X-RAY ABSORPTION FINE STRUCTURE SPECTROSCOPY OF THIN FILM SiGe ALLOYS

X-RAY ABSORPTION FINE STRUCTURE SPECTROSCOPY OF THIN FILM SiGe ALLOYS

By

JEFF AUBRY, B.Eng.

A Thesis
Submitted to the School of Graduate Studies
in Partial Fulfillment of the Requirements
for the Degree
Master of Engineering

McMaster University

MASTER OF ENGINEERING (1996)
(Materials Engineering)

McMaster University
Hamilton, Ontario

TITLE:	X-Ray Absorption Fine Structure Spectroscopy of Thin Film SiGe Alloys
AUTHOR:	Jeff Aubry, B.Eng. (Queen's University)
SUPERVISORS:	Professor A.P. Hitchcock Professor T.E. Jackman
NUMBER OF PAGES:	***xi, 150***

ABSTRACT

SiGe thin film alloys are the subject of intense interest in semiconductor research. The extent of bond length dependence upon alloy composition in these materials is a subject of some debate in the literature. This work details our Si and Ge K-edge extended x-ray absorption fine structure (EXAFS) measurements on a selection of strained and relaxed single crystal SiGe alloys. Constrained, simultaneous fits to the EXAFS of multiple spectra from both Si and Ge K-edges were performed in order to extract quantitative data for bond lengths and co-ordination numbers.

The first analysis was performed solely using EXAFS spectra from relaxed alloys grown on Si. The results indicate that first shell bonding in relaxed SiGe alloys adheres to a weakly mixed Pauling-Vegard regime, showing detectable composition dependence (bond length change of 0.03 Å over the full composition range). In the notation of the CT theory of Thorpe and co-workers (*Phys. Rev. B* **46**, 15872 (1992)), the topological rigidity parameter, **a****, is found to be $0.70^{+0.09}_{-0.03}$. The results are compared to other theoretical and experimental results, and alternate models to the CT theory are explored. Ordering effects in the co-ordination numbers are also evaluated.

The second analysis was performed on a small range of complimentary strained and relaxed samples, to investigate the hypothesis that strained SiGe alloys on Si(100) have shorter bond lengths than relaxed samples. The results of the analysis suggest that strain accommodation is at least partly accomplished by bond length contraction.

Finally, the Appendix details a complimentary project in near-edge x-ray absorption fine structure measurements of SiGe alloys. Specifically, a strain-induced polarisation dependence in the Si K-edge spectra of SiGe films is explored with measurements of a large range of samples. The results indicate that the source of the polarisation is not yet fully understood.

ACKNOWLEDGEMENTS

The author would like to express his gratitude to a number of individuals: Dr. A.P. Hitchcock, my supervisor at McMaster University who made this work possible; Dr. T.E. Jackman, my supervisor at the National Research Council (NRC), who gave me ample opportunity to make use of the IMS facilities at the NRC; Dr. T. Tyliszczak, the expert who made things happen; and Dr. J-.M. Baribeau, who produced my samples and provided invaluable assistance throughout the course of the work. Finally, the author would like to acknowledge the support from the staff at the CSRF-DCM beamline at SRC and the C2 station at CHESS.

TABLE OF CONTENTS

1.0 INTRODUCTION TO SiGe ALLOYS AND HETEROSTRUCTURES

2.0 THEORY OF EXAFS

3.0 LITERATURE REVIEW AND GOAL OF MY WORK

4.0 EXPERIMENTAL DETAILS

5.0 DATA ANALYSIS

6.0 RESULTS AND DISCUSSION

7.0 CONCLUSION

APPENDIX

LIST OF FIGURES

1.0 INTRODUCTION

2.0 EXAFS THEORY

3.0 LITERATURE REVIEW

4.0 EXPERIMENTAL

5.0 DATA ANALYSIS

6.0 RESULTS AND DISCUSSION

APPENDIX A - POLARISATION DEPENDENCE

LIST OF TABLES

LIST OF SYMBOLS

α, α_{AB}	linear elastic force constant
β	angular force constant
$\chi(k)$	EXAFS data
$\tilde{\chi}_i^F$	experimental Fourier filtered data points
$\tilde{\chi}_i$	calculated EXAFS data points
$\tilde{\chi}(q)$	Fourier filtered EXAFS data
$\delta_j(k)$	phase shift
Φ	ionization potential
λ	electron mean free path
$\mu(E)$	characteristic absorption coefficient, in energy space
$\mu(k)$	absorption coefficient, in k-space
$\mu_0(k)$	non-oscillatory signal from isolated atom
σ^2_j	Debye-Waller factor
a^{**}	topological rigidity parameter
$A_j(k)$	amplitude function for atom j
E	energy
E_K	kinetic energy
E_o	energy scale correction term
f	number of files
$f(\pi,k)$	element-specific backscattering factor
$F_n(r)$	magnitude of the Fourier transform
F_{radial}	radial force
$h\nu$	photon energy
I	transmitted photon flux
I_0	incident photon flux
k	de Broglie wave vector
k^n	k-weighting
L	path length
m_e	electron mass
n	number of data points
M	number of parameters
N_j	co-ordination number for atom j
r_j	distance from central atom to atom j
r_e	virtual crystal bond length
r^o_{xx}	natural elemental bond length
S	sums of squares of residuals
S_o^2	passive electron reduction term
u_{AB}	displacement of the nearest neighbor atom
$W(k)$	window function
x	composition
y	fraction of one type of atom around the central atom
Z	atomic number
$Z_{A,B}$	number of co-ordinated atoms around A or B

LIST OF ACRONYMS AND ABBREVIATIONS

APD	Avalanche PhotoDiode
CVD	Chemical Vapor Deposition
DAC	Digital to Analog Converter
EXAFS	Extended X-ray Absorption Fine Structure
FT	Fourier Transform
FY	Fluorescence Yield
HBT	Heterojunction Bipolar Transistor
HMT	High Mobility Transistor
IC	Integrated Circuit
MBE	Molecular Beam Epitaxy
MODFET	MOdulation-Doped Field Effect Transistor
MOS	Metal-Oxide-Semiconductor
MOSFET	Metal-Oxide-Semiconductor Field Effect Transistor
NEXAFS	Near Edge X-ray Absorption Fine Structure
RTA	Rapid Thermal Annealing
TEY	Total Electron Yield
VCA	Virtual Crystal Approximation
XAFS	X-ray Absorption Fine Structure

1.0 INTRODUCTION TO SiGe ALLOYS AND HETEROSTRUCTURES

In this chapter, the motivations for studying SiGe materials will be outlined. A general description of how SiGe materials fit into modern Si technology will be given, followed by a brief outline of device applications. The chapter ends with a discussion concerning questions regarding the local structure of these materials.

1.1 Motivations For Development

Silicon integrated circuitry (IC) technology, the basis upon which most of the electronics industry is built, has overcome many hurdles during its rapid growth; nonetheless, Si technology still has many significant challenges which need to be overcome. Probably the most looming problem is the approaching limitation of finite atomic dimensions. Most of the gains in device speed achieved over the past years in Si-based technology have been achieved by advances in lithography techniques (miniaturization of components), device integration (forcing more devices onto a single chip), and discrete device design (more efficient devices), rather than "faster electrons". It is widely believed that in the future, continuation in size reduction of component gates/devices will not entail a corresponding increase in device speed, but rather a decrease, as the devices will become too small to properly confine carriers [HH96, C95, GOE95, M94, B92, K92]. Furthermore, the capital investments required for further reductions in device size are becoming prohibitively expensive [HH96]. Such a trade-off between device size and speed significantly impedes the possibilities of evolution of the electronics industry, and as such, ways around this restriction are constantly being sought.

Another problem has been the lack of progress in integrating optoelectronics into conventional Si processes. The field of optoelectronics is gaining more and more prominence, and thus it has become imperative to find a way to successfully bring about it's marriage with standard Si IC technology [C95, GOE95, K95]. The discovery of a direct gap Si-based material would do much to advance the integration of optoelectronics and traditional Si technology. To date, this goal has proven to be very elusive, and optoelectronics remains somewhat isolated from Si IC technology. At one time, it was thought that III-V materials represented solutions to these problems. These materials have proven to be quite interesting due to their excellent carrier mobilities and optoelectronic activity, as well as their flexibility in band gap engineering and carrier confinement through alloy and heterostructure growth. Unfortunately, III-V materials have several faults associated with them, including poor thermal conductivity (which limits device operating power and packing density), very high raw material costs, the lack of a high-quality oxide (and thus, complex processing requirements i.e. implantation, annealing for semi-insulation, etc.), and high numbers of intrinsic defects (which dramatically reduces chip yields) [C95]. Of most importance, however, is the fact that III-V materials and Si tend to cross-dope each other quite effectively; consequently, these materials are poorly suited to integration into existing Si technology [B92]. It is unrealistic and certainly not economical to abandon the multi-billion dollar Si industry for III-V's in the foreseeable future; to date, this has precluded monolithic III-V integration into standard Si processes. Despite the enormous potential benefits, as of 1993, III-V's had yet to capture more than 2% of the IC industry, seeing use in only specialty applications [KD95].

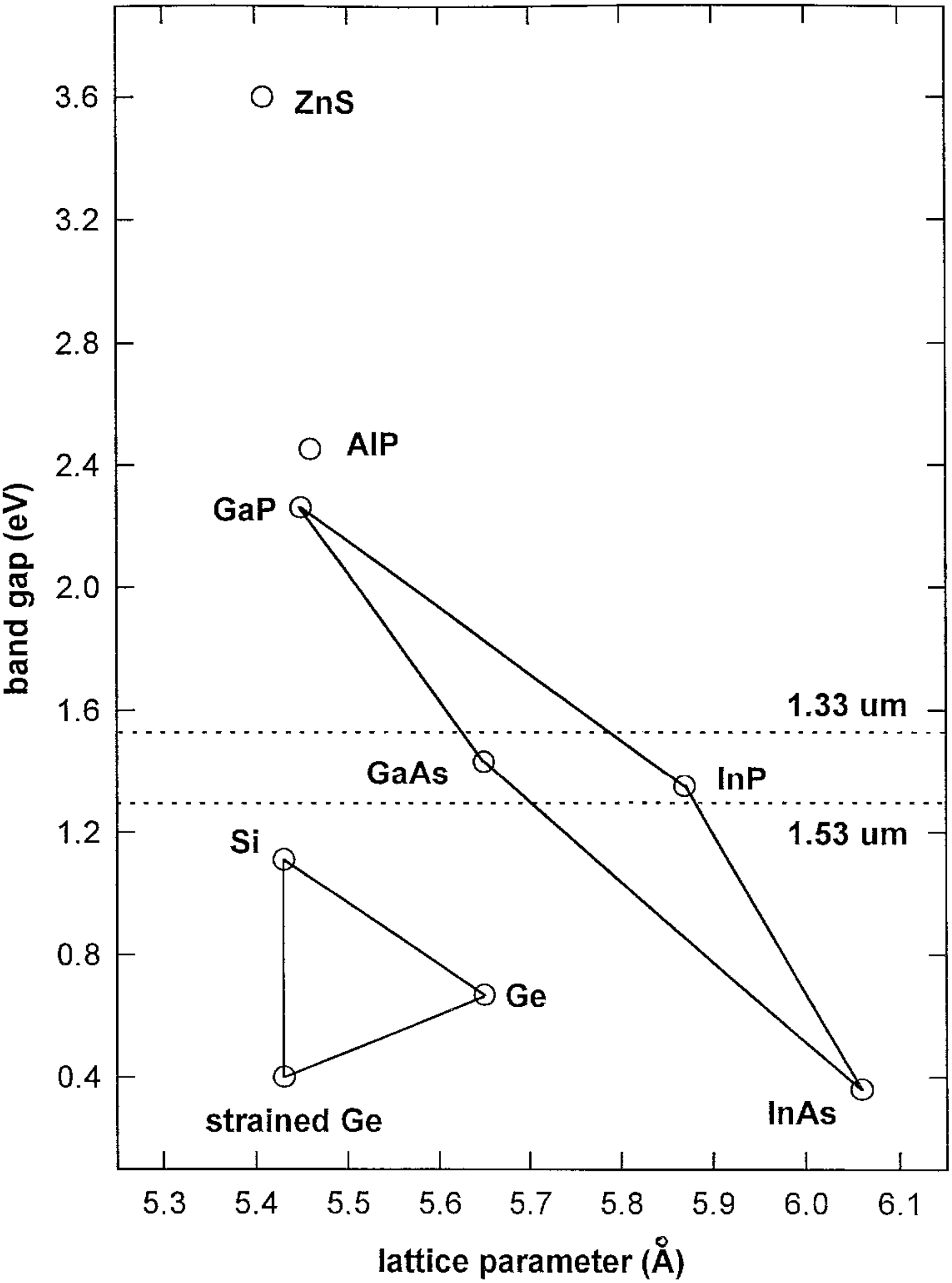

Figure 1.1 - Band gaps and lattice parameters for various materials. The solid lines depict approximate limits for band gap engineering for the materials systems shown. The dotted lines show the band gap range useful for optoelectronic applicatications.

Heterostructures have proven to be of enormous technological importance [C95, CE92, E86]. III-V materials form wide ranges of alloys among themselves (see Figure 1.1) [B92] which provides the opportunity to produce highly engineered, lattice matched, tailored heterostructures to suit a wide array of device needs. Unfortunately, among available semiconductor materials, only some III-Vs, AlP and GaP, and ZnS, a II-VI material with the same cross-doping problems of III-Vs, have lattice constants near enough to that of Si to create heterostructures with few enough defects to be of device quality. These materials cannot be used effectively in Si processes, and so up until the late 1980's this precluded the use of Si-based heterostructures. Without band gap engineering, Si can play only a marginal role in optoelectronics, due to a band gap that is indirect and too wide for fibre optic applications (1.0 μm, requires 1.3-1.5 μm) and too narrow (IR range) for visual display technology [C95, B92, P91].

Within the last ten years, interest has developed in IV-IV materials, with particular emphasis on crystalline Si-Ge alloys and heterostructures. Possessing exciting new intrinsic electronic properties, SiGe materials will provide the opportunity for continued Si IC evolution with simple incorporation into existing standard Si technology. In addition, SiGe materials may even bridge the separation between Si IC and optoelectronics technology, showing several promising optoelectronic properties [C95, GOE95, KD95, M94, B92, P91].

Silicon and germanium, which share the diamond cubic structure, are fully miscible, forming random substitutional alloys of any composition [OA84, SK39]. The lattice constant of Ge is larger than that of Si by approximately 4.17% at room temperature [I69]. This difference produces significant strain during epitaxial growth of SiGe alloys, distorting the Brillioun zones of the epitaxial alloys away from BCC symmetry (in fact, the number of point-symmetry operations is reduced from 48 for the unstrained diamond lattice to 16 for strained (001) growth, 12 for (111) growth, and 8 for (110) growth). This can be expected to produce significant changes in the band structure relative to that of Si and Ge, and hence, changes in the electronic properties [MWS93].

Epitaxial strain cannot be maintained for any desired film thickness. Once the SiGe film growth increases beyond a critical thickness limit (which is itself dependent upon film composition and substrate, see Figure 1.2 for on-Si alloys) [PB85], the epitaxial strain becomes energetically unfavorable compared to the energy requirements for the creation of misfit dislocations. Provided that the kinetics are favorable, an alloy whose thickness is beyond the critical limit undergoes spontaneous relaxation, decoupling its lattice from that of the substrate and producing a high density of misfit defects. Such materials are not useful to device designers, who require nearly defect-free materials. When kinetics are unfavorable, the film may not relax (or relax only incompletely), existing in a metastable strained region as shown in Figure 1.2. Such films may be useful to device designers; however, the thermal budget becomes a critical limitation.

In addition to alloys, strained Si/SiGe/Ge heterostructure combinations can be grown. Alternating layers of substrate materials and Si-Ge combinations extend the favorable energetics of the elastic strain field, permitting growth of films much thicker than the critical limit for a similar alloy composition [A+89]. These heterostructures have exhibited interesting electronic properties that are superior to those of Si, and have also demonstrated important optoelectronic properties [GOE95, P91, A+89, B86].

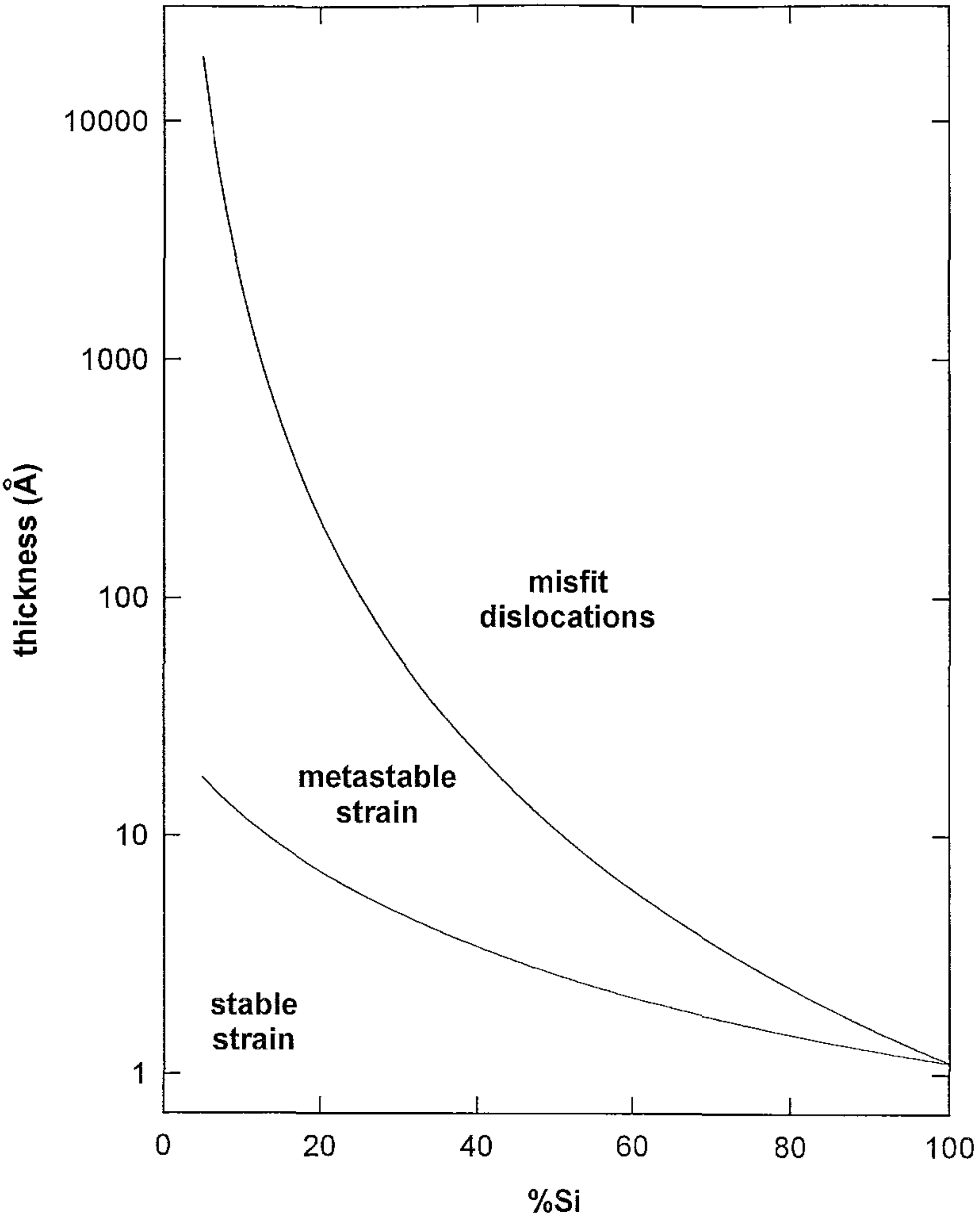

Figure 1.2 - Approximate critical thickness limitations in SiGe expitaxial growth on Si(100), according to [PB85].

1.2 SiGe Electronic Properties And Device Applications

The electronic properties of SiGe alloys and heterostructures are highly dependent upon the amount of alloying element, the substrate orientation, and the resulting strain field within the material [MSW93]. The bandgap of Si (1.12 eV), is larger than that of Ge (0.66 eV). Consequently, SiGe alloys have bandgaps interpolated (non-linearly [MSW93]) between these two values, depending upon the alloy composition (see Figure 1.3). Epitaxial strain affects the band structure of the alloys by distorting the BCC symmetry of the Brillioun zones, and hence, the resulting band structures, while substrate orientation ((100) vs. (111) vs. (110)) determines the nature of the strain in the unit cell, which again affects the Brillioun zone symmetry. The manipulation of the 3 variables, composition, strain, and substrate orientation, creates the potential for band gap engineering in SiGe device technology.

The first commercial SiGe devices, produced by IBM in conjunction with Analog Devices Inc. (ADI), have been heterojunction bipolar transistors (HBTs) (Figure 1.4) [M94, K+89]. The use of epitaxially strained SiGe alloy layers in the base region of the device provides three separate benefits. First of all, a reduction in the base bandgap (from the full Si bandgap) at the emitter-base junction of the device (created by a compositionally-graded SiGe base layer) exponentially increases minority carrier injection into the region for a given emitter-base bias. This results in an approximately 600-fold increase in collector current, as well as increases in overall current gain and emitter power, as compared to Si-based devices [C95, GOE95]. These properties make SiGe HBTs very useful for power amplifiers [KD95]. Secondly, the graded SiGe base produces an internal electric field, thereby accelerating minority carriers through the region, greatly increasing base and emitter transit times [C95, A+91]. Finally, SiGe reduces the overall output resistance of the device, which is of paramount importance

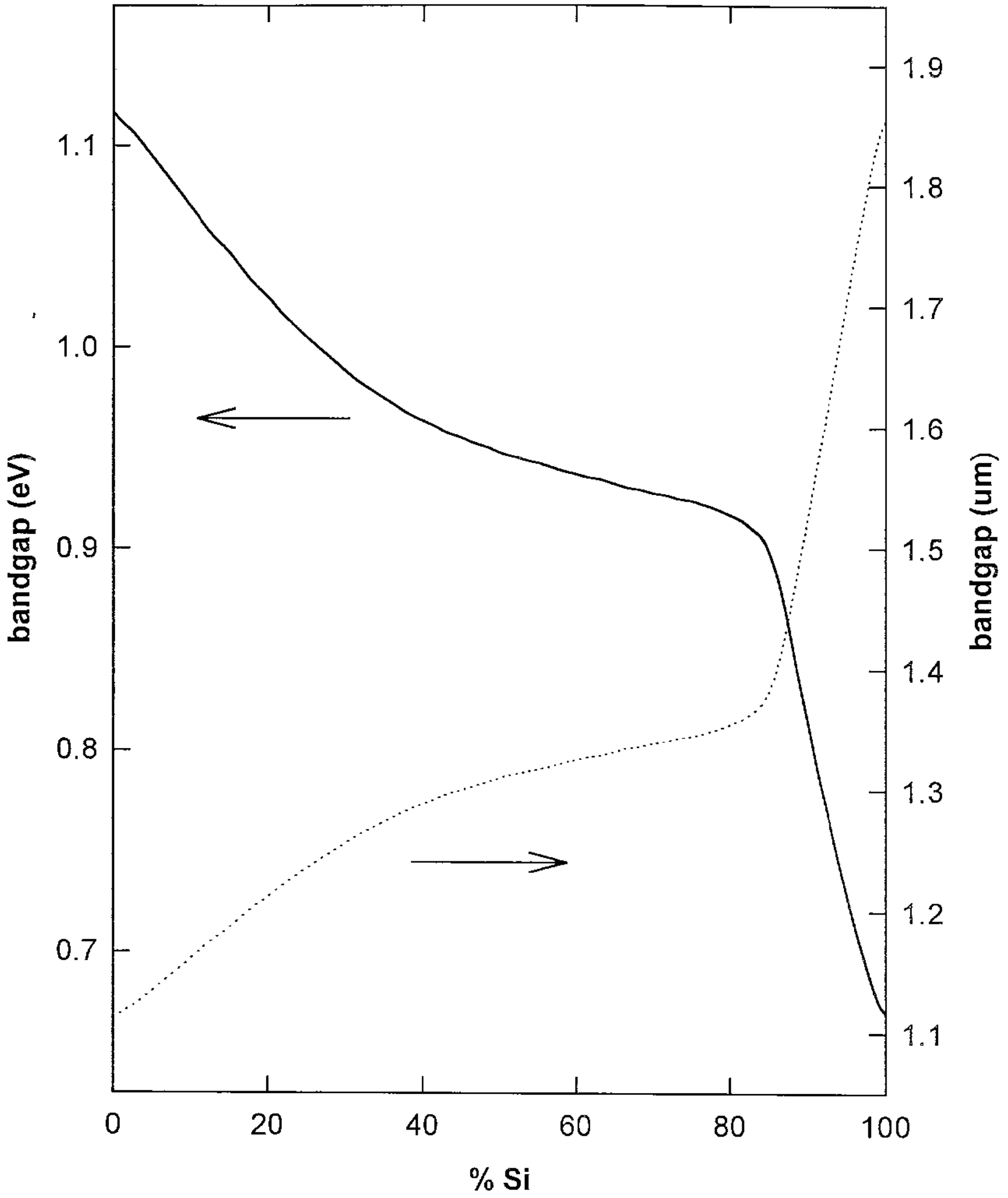

Figure 1.3 - Bandgap of bulk SiGe alloys as a function of composition, according to the calculations of Ma et al. [MSW93].

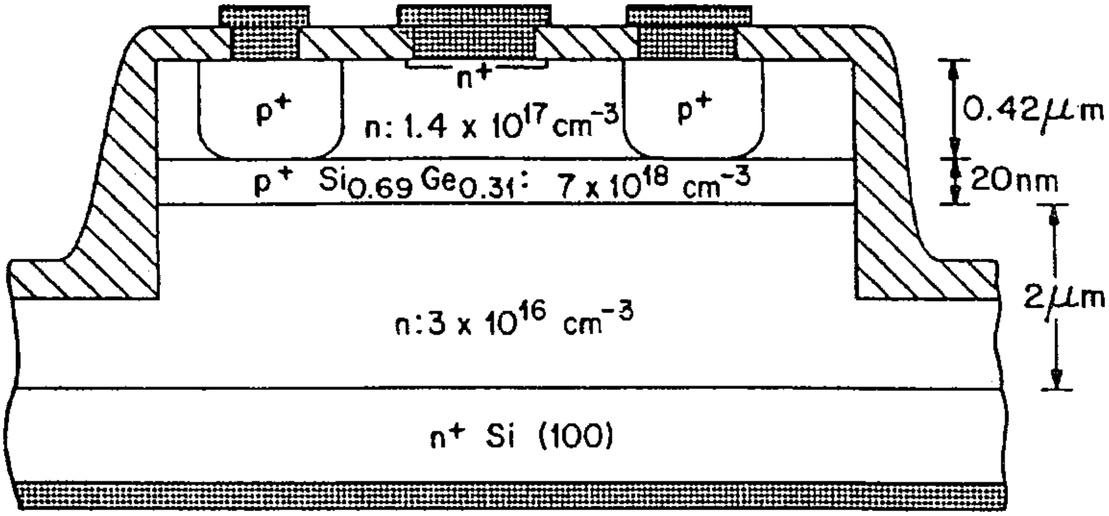

Figure 1.4 - Schematic diagram of a SiGe heterojunction bipolar transistor (HBT), modeled on Figure 3 in [K+89].

in any analog circuit. The final result is a record setting device - IBM SiGe HBT discrete device switching frequencies have been clocked at 120 GHz, about twice that of any pure Si-based device, and competitive with III-V based devices [KD95]. Using this SiGe HBT technology, IBM and ADI have released a 1 GHz 12 bit digital to analog converter (DAC) - again, a speed record breaker - which consumes a low 1 W at a bias of 5V - a perfect fit for mobile telecommunications [KD95, M94]. Additionally, SiGe HBTs are receiving attention for use in microwave power applications, where their high voltage properties (high gain, low base resistance) are well suited [H+95, SD95].

There exists a large offset between the valence bands and a smaller offset between the conduction bands of Ge and Si (Figure 1.5), and as such, SiGe alloys form tunable type-II heterostructures with these materials [K95, M92, P91]. This provides an enormous amount of flexibility for application of SiGe materials to modulation-doped field effect transistors (MODFETs), as depicted in Figure 1.6. Additionally, strain forces a split in the degeneracy of the SiGe valence band, often (depending upon substrate orientation) forcing the uppermost valence band (the light-hole band) to be topmost. This has the desirable effect of vastly increasing the hole mobility in SiGe p-MODFETS, since the effective mass of the light hole band is always much lower than that of the heavy hole band. This then permits much faster devices [A+96, K95, GOE95, M94]. Devices created to date have demonstrated better switching speeds [C95] than those of Si-based MODFETs, in addition to superior transconductances.

SiGe heterostructures have particular potential for use in a variation of the MODFET, the high mobility transistor (HMT). This device (Figure 1.7) is characterized by high carrier mobilities achieved by two dimensional confinement of carriers in a strained, defect-free layer of conventional Si or Ge, epitaxially grown upon a graded SiGe buffer layer [KD95, M+94, M92]. The buffer acts as a sort of "defect sponge",

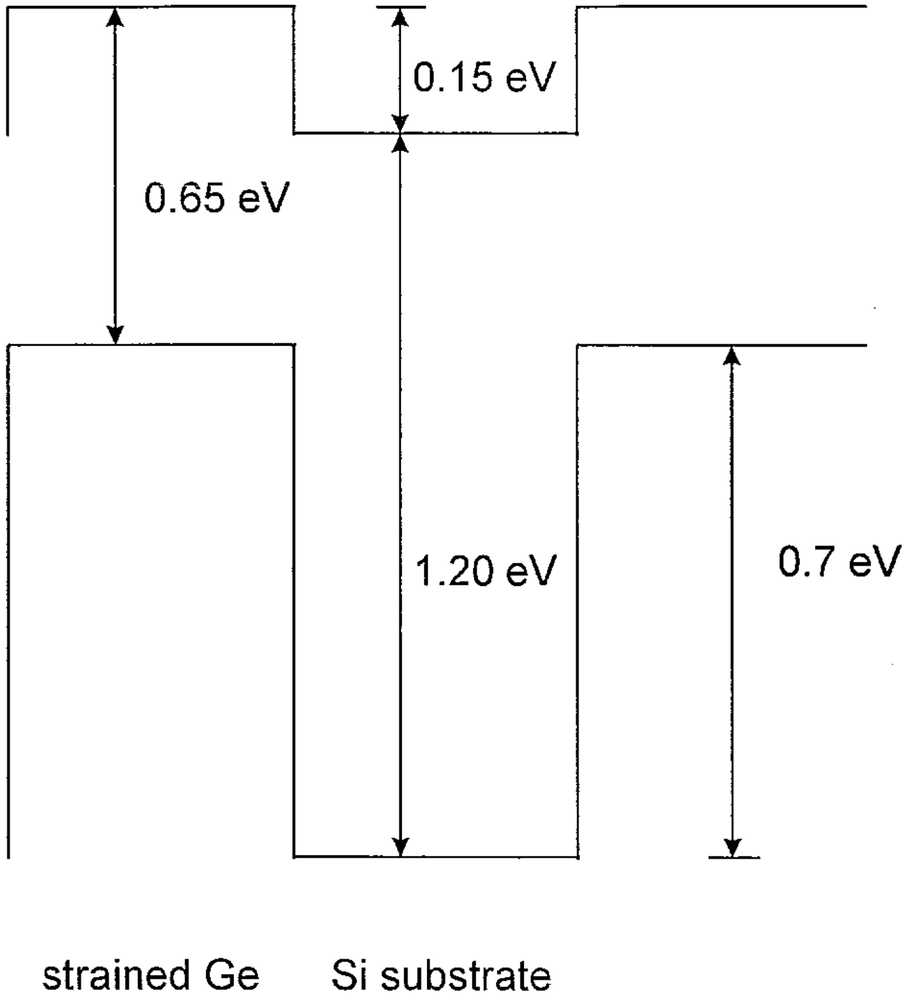

Figure 1.5 - Maximum band offsets in SiGe alloys on Si substrates.

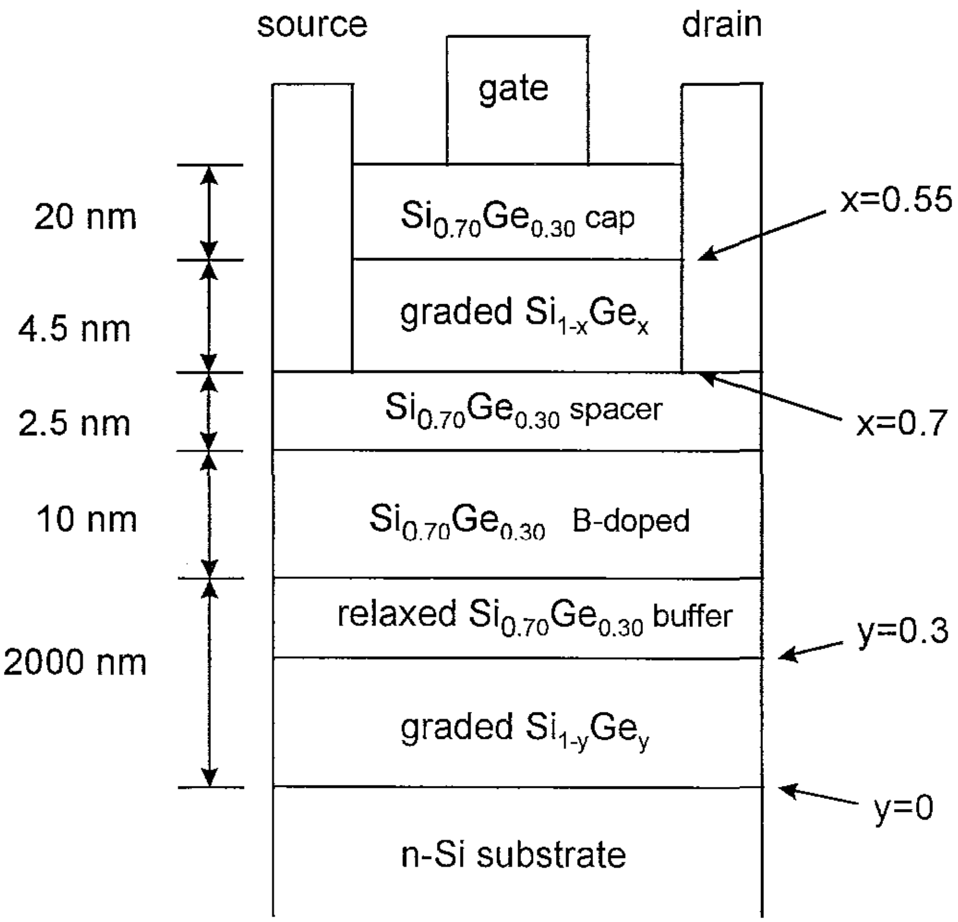

Figure 1.6 - SiGe p-type modulation-doped field effect transistor (pMODFET), as shown as Figure 1 in [A+96].

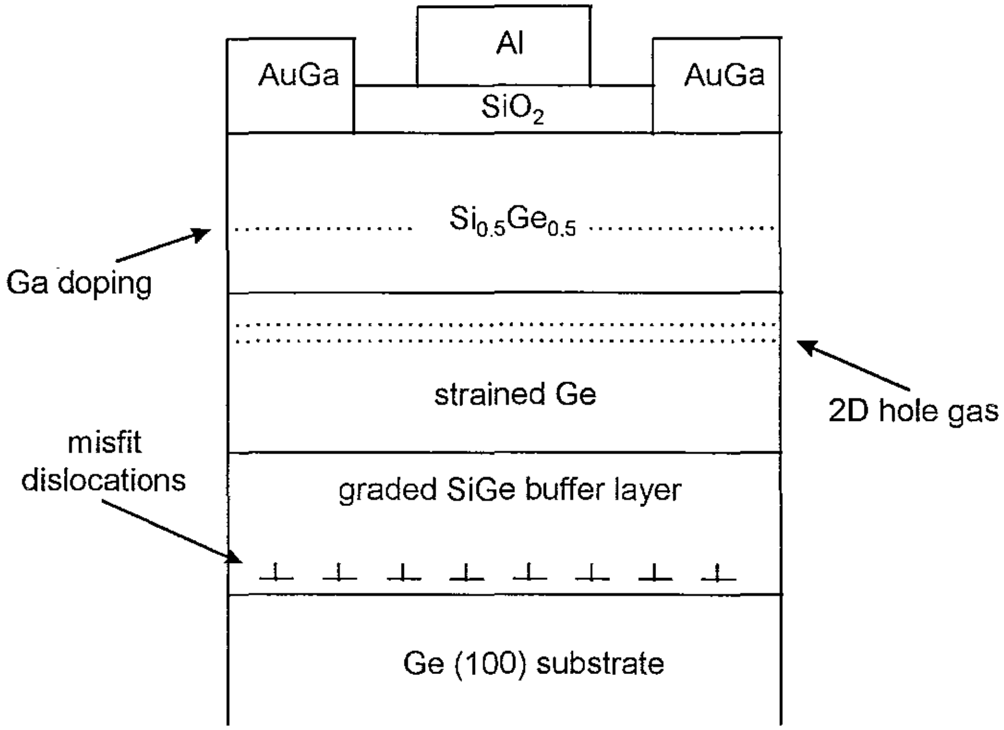

Figure 1.7 - Schematic representation of a SiGe high hole mobility transistor (HMT), as depicted in Figure 1 in [M+94].

permitting the formation of a near perfect interface with the strained channel layer, which is forced to adopt the lattice parameter of the SiGe buffer. Again, the strain in the channel acts to vastly improve carrier mobility, elevating SiGe HMTs into competition with the best III-V devices [KD95, M94]. Other devices being considered for SiGe inclusion include resonant tunneling diodes and bipolar inversion channel FETs [M92, A+91].

The greatest advantage of SiGe alloys and heterostructures in microelectronics is the ease with which these materials can be integrated into existing Si IC technology. For virtually any SiGe device, the inclusion of a simple Si cap on the SiGe alloy or heterostructure permits construction of MOS (Metal Oxide Semiconductor) integrated circuits on the very same wafer. SiGe MODFETs in particular show great promise for use in complementary-MOS (CMOS) application, where the vastly improved p-type carrier mobility would have its greatest benefit, since it would be similar to the otherwise much higher n-type mobility. SiGe CMOS devices should deliver significant improvements in power consumption and noise levels over standard Si-CMOS, not to mention an expected speed improvement by a factor of 3-5 [KD95].

SiGe materials also have significant optoelectronic potential. Si and Ge possess indirect gaps, though Ge is very nearly a direct gap material, and the addition of strain (i.e. epitaxially strained SiGe alloys or heterostructures) may produce a direct gap [MSW93, P91]. Unfortunately, the most recent calculations predict that a direct band gap is not created in strained SiGe alloys, and to date, experimenters have not provided solid evidence to indicate otherwise [MSW93]. As for SiGe heterostructures, there has been no progress in producing a direct gap, and for the most part, researchers now discount the possibility of quasi-direct gaps forming in SiGe superlattices. Nonetheless, SiGe materials continue to hold considerable potential for future optoelectronic applications. The SiGe band gap is a function of composition, and therefore, tunable (see Figure 1.3). The technologically important optical wavelengths of approximately 1.3 and 1.5 μm (where IR absorption losses and Rayleigh scattering in SiO_2 fibres are minimized), unreachable with conventional Si technology, are covered by the SiGe band gap range, giving these materials the potential to be useful in fibre optic applications. In fact, SiGe/Si strained alloy heterostructures are currently being used in avalanche photodiodes (APDs) (Figure 1.8). Si-APDs (one of the few optoelectronic applications of conventional Si) have proven to be the standard to which other semiconductor photodetectors are compared. Si-APDs are sensitive in the visible and near IR regions (0.5 - 1.0 μm); however, the use of SiGe/Si heterostructures permits the optical absorption region to be extended to the 1.0 - 1.5 μm region, which was at one time accessible only with the use of exotic III-V combinations. Performances of SiGe-APDs are comparable to those of Si-APDs, the industry benchmark [K95, A+91, P91]. Additionally, SiGe heterostructures have shown electroluminescent activity, and are the subject of interest in the thin film display field [GOE95, K95].

1.3 Local Structure of SiGe Alloys

SiGe devices have shown the potential to deliver exciting gains in Si-based IC performance; moreover, SiGe device technology is still in its infancy [K95, M94]. The dramatic gains described above are only a sample of what is possible, and many more are expected as SiGe technology matures. Only when the fundamental questions of strain accommodation, lattice relaxation modes, atomic ordering, phonon modes, etc. are answered will researchers dealing with more applied problems be able to fully exploit the potential of SiGe materials [K95, M94, MSW93, CT92, MT92].

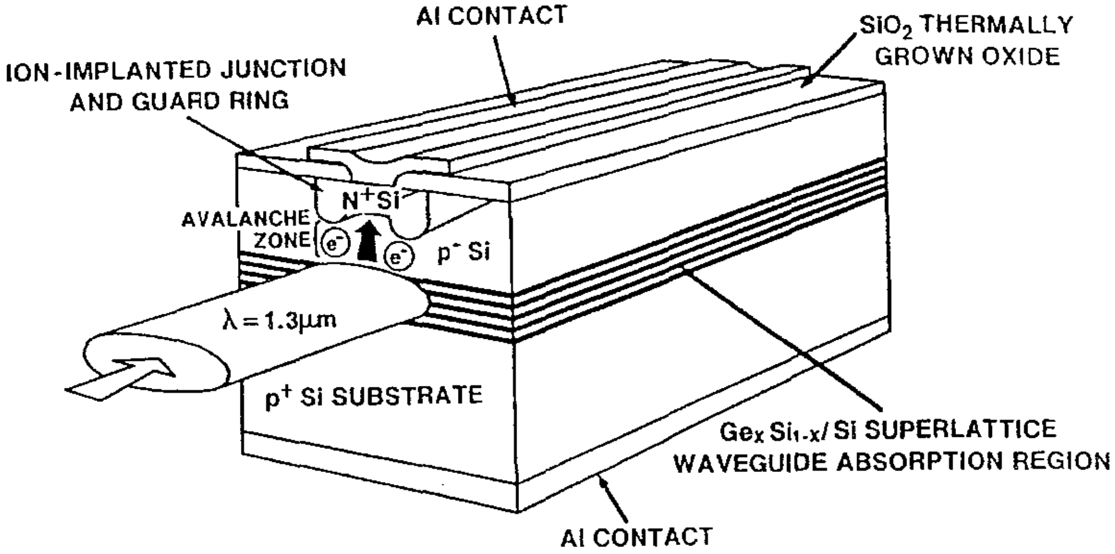

Figure 1.8 - Schematic of a SiGe avalanche photodiode (APD) for operation in the 1.3-1.5 μm region, modeled on Figure 5 in [P91].

The need for fundamental research into SiGe structural properties is particularly evident in the on-going work in calculated band structures. The results of the calculations of Ma et al. [MSW93] (the most recent) for SiGe alloys are not entirely satisfactory, showing several discrepancies with previous calculations as well as with rare experimental results. In their calculations, Ma et al. used a virtual crystal approximation (VCA) to depict the SiGe unit cell. The VCA treats the entire solid as an infinite replica of a single cell, each containing the same atomic potentials and the same bond lengths and angles, with no local disorder. This is in effect a special case of Vegard's law, which states that the lattice parameter of an alloy is equal to the compositionally weighted interpolated value between the two pure constituents [MZ84, V27]. Vegard's law implies that bond lengths are soft, and accommodating (i.e. compositionally dependent), while bond angles are fixed at the regular angles. Vegard's law tends to well describe situations where metallic bonding is predominant; however, it is never strictly obeyed and it seems implausible that it would be obeyed in semiconductors. Recent x-ray diffraction studies indicate that SiGe alloys have a slight negative bowing deviation away from Vegard's law [K95]. Conversely, Pauling's rules (which actually are a more generalized form of Bragg's results [B20] for ionic materials) state that the bond length between a given atom pair is fixed (i.e. independent of composition), and in alloys, steric strain is accommodated by bond angle changes [P67]. Pauling's rules are better suited for situations of directed chemical bonds [ANS94, MT93, CT92, MT92], and thus are probably a better description of bonding in semiconductors, which is known to be highly covalent [P73]. Figure 1.9 depicts the two models in a bond length vs. composition plot.

The VCA approximation used by Ma et al. is certainly a limitation in their results, since it is merely a simple method to model a random, complex structure, such as the

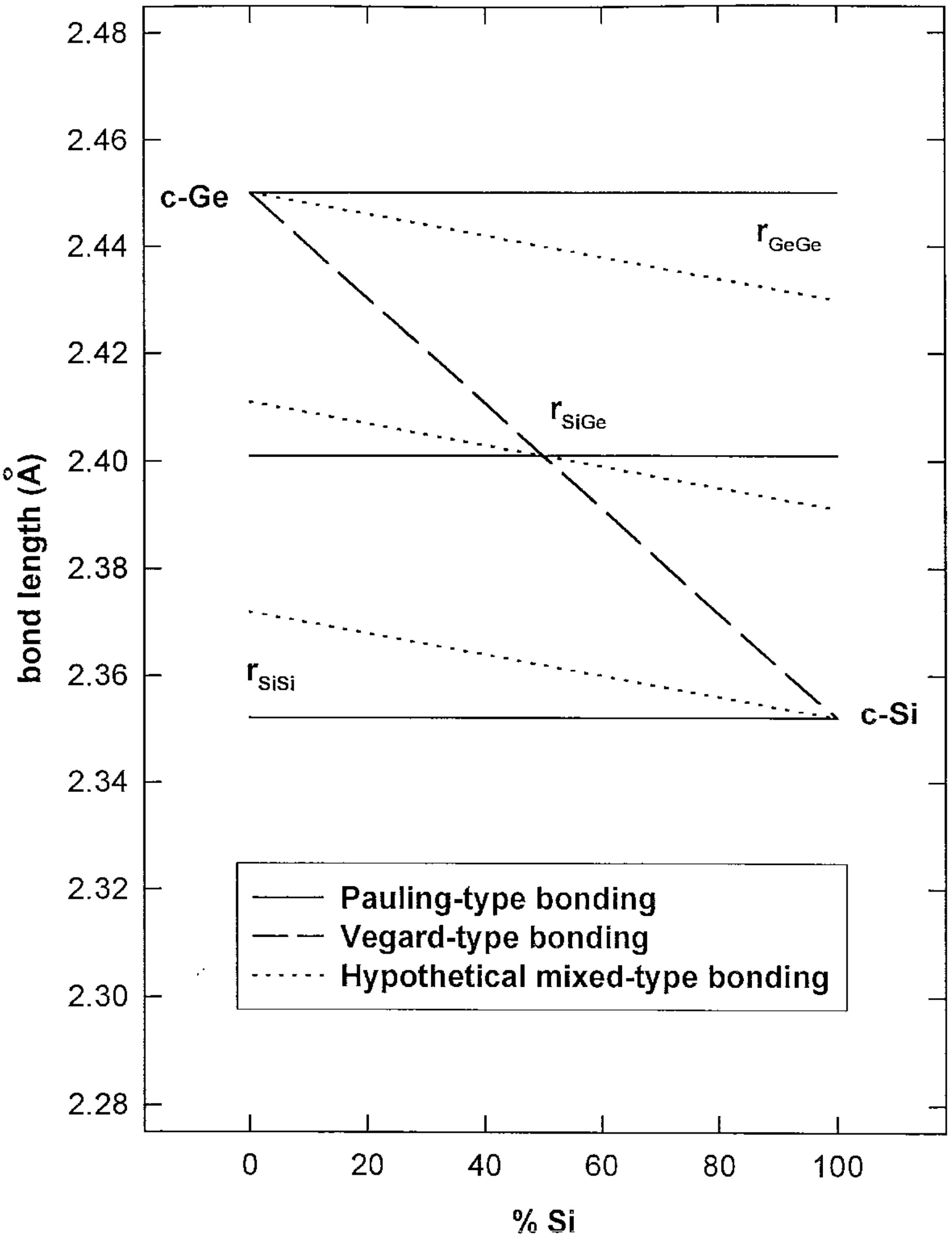

Figure 1.9 - Pauling-, Vegard-, and hypothetical mixed-type bonding depicted on a bond length vs. composition plot. Pauling- and mixed-type bonding produces 3 distinct bond lengths, whereas Vegard-type bonding requires only a single length.

SiGe unit cell. Unfortunately, there is very little knowledge of the true *local* structure in SiGe, and as such, at the time of their publication, Ma et al. had no clear alternative to the VCA. Thus, there is considerable research devoted to characterizing the local structure of SiGe materials [ANS94, MT93, A+92, CT92, K+92, MT92, MTC91, W+91, N+88, I+85]. The aim is to determine what mixture of the two models best describes bonding in SiGe (i.e. Figure 1.9). To answer this, one must obtain quantitative data on the local structure.

EXAFS (Extended X-ray Fine Structure) spectroscopy [ANS94, MT93, A+92, CT92, K+92, MT92, MTC91, W+91, N+88, I+85] is an especially useful technique for quantitatively studying local structure in materials, especially in the SiGe system. Analysis of EXAFS data permits the extraction of quantitative data for interatomic distances as well as coordination shells about the central absorbing atom, thereby permitting researchers to delve into the local structure of their material. The standard techniques, such as diffraction and microscopy, do not easily yield quantitative information about local structure; hence, EXAFS represents a convenient complement.

This work is an investigation of the local (i.e. first shell) structure in SiGe alloys, using EXAFS spectroscopy. Chapter 2 details the physics of the EXAFS technique, in addition to some discussion of data processing and extraction of quantitative results. This prepares the reader for Chapter 3, which is an extensive literature review, followed by a detail statement of the goals of this work. Chapter 4 details the experimental procedures in sample growth and EXAFS measurements. Chapter 5 is a thorough review of data processing and fitting procedures. Chapter 6 is a presentation and discussion of the fitting results, along with the respective error analyses. Finally, Chapter 8 concludes the EXAFS discussion, and includes a description of possible future work.

In addition, Appendix A details a project in SiGe NEXAFS, which was also completed as part of this author's Masters of Engineering research. Using plane-polarized synchrotron radiation, Hitchcock and co-workers [H+94, T+94, H+93, A+92] discovered a polarization-dependent signal in the very near edge portions of the Si K-edge x-ray absorption spectra of strained SiGe alloys. They attributed this to the presence of strain-induced conduction band states in the material. Using the same methodology, this author has further explored the relationship between the alloy strain and the resulting polarization signal, and the results of this exploration are detailed in the Appendix.

2.0 THEORY OF EXAFS

This chapter begins with a brief description of x-ray absorption fine structure spectroscopy. The chapter concludes with a discussion of the general methodology of data analysis.

2.1 Introduction To X-ray Absorption Fine Structure Spectroscopy

X-ray absorption fine structure spectroscopy (XAFS) are oscillations in the x-ray absorption coefficient extending for a range of up to 1000 eV beyond the absorption edge of the absorbing atoms (see Figure 2.1, absorption edge). The oscillations principally arise from constructive and destructive interference between the outgoing photoelectron wave and that portion of itself backscattered by the surrounding shells of atoms [SSL71]. Thus, isolated atoms, such as noble gases, do not show regular XAFS features. The spectroscopic technique is somewhat similar to electron diffraction, except the electron source is the central x-ray absorbing atom. The scattering is generally over short range (1 to 5 identifiable co-ordination shells for most materials), and multiple scattering effects (involving more than one scattering paths) are somewhat separable. While the eventual aim of XAFS theorists is to utilize single and multiple scattering signals together in a unified approach, separation of the two phenomena is still common, especially when studying complex material problems, such as with SiGe alloys. Separation (see Figure 2.1 inset) leads to a division of the overall XAFS signal into two portions, the NEXAFS (Near Edge X-ray Absorption Fine Structure) signal,

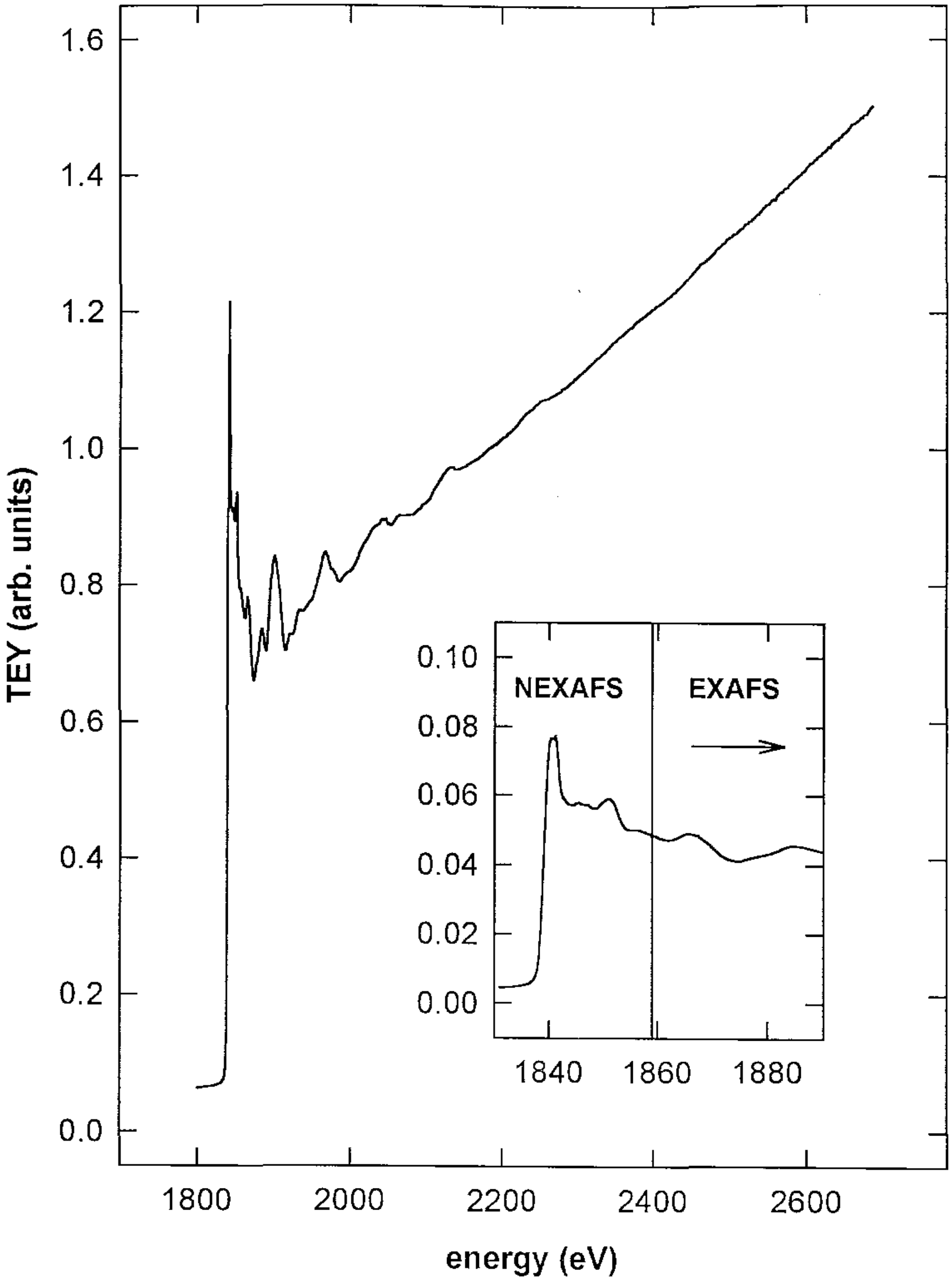

Figure 2.1 - Si K-edge TEY spectrum of crystalline Si. The inset depicts the separation between the NEXAFS and the EXAFS portions of the spectrum.

which is dominated by the multiple scattering signal, and the EXAFS (Extended X-ray Absorption Fine Structure) signal, which is dominated by single scattering events.

The EXAFS spectroscopy technique has several beneficial characteristics. It is element specific, highly sensitive to short range order (structure and bonding), and applicable to a wide variety of systems. This technique provides a simple method to quantitatively study the local chemical environment of virtually any element in a multitude of materials environments. Analysis of the EXAFS data permits the extraction of quantitative data for interatomic distances as well as coordination shells about the central absorbing atom. Thus, EXAFS is an especially useful technique, either as a compliment to the standard materials analysis techniques, or as a substitute when other structural techniques are not useable, ie. when there is only short range order about the element of interest. Additionally, one can apply many variations to the EXAFS technique to tailor it to a wide variety of materials problems. Examples include polarization EXAFS using plane-polarized synchrotron radiation for studies of anisotropic materials (such as planar interfaces in quantum wells), low temperature EXAFS for higher coordination shell analysis, glancing angle and/or total external reflection mode EXAFS for surface layer studies, etc. Examples of material problems where XAFS is especially useful include disordered and amorphous systems, alloys, buried interfaces, surface coverages, impurities/dopants, and catalysis [W86].

XAFS techniques are limited by the fact that the signals are averages of all absorbing atoms, and hence, the results are averaged for all the atomic environments within the illuminated area. Thus, in the case of multiple layered heterostructures, for example, one cannot immediately differentiate the signal from an interfacial atom from that of a bulk atom. Despite this perceived limitation, XAFS techniques have proven to be extremely useful, and are gaining prominence throughout the literature [O94, W86].

2.2 EXAFS Theory

X-ray attenuation is described by the classical Beer-Lambert equation:

$$\boxed{I = I_0 \exp(-\mu L)} \tag{2.1}$$

where **I** is the transmitted photon flux, I_0 is the incident photon flux, **L** is the path length, and μ is the characteristic absorption coefficient, a function of the element **Z** and the photon energy **hν**. Upon absorption, the ejected photoelectron escapes from the bound energy level to the vacuum level with kinetic energy E_K:

$$\boxed{E_K = h\nu - \Phi} \tag{2.2}$$

where Φ is the ionization potential of the atom (see Figure 2.2). The photoelectron, being a small particle, exhibits appreciable wave-particle duality, and consequently can also be described as a photoelectron wave, with a de Broglie wave vector **k**:

$$\boxed{k = \sqrt{\frac{2m_e(E_K - E_o)}{h^2}}} \tag{2.3}$$

where m_e is the electron mass, and E_o, as depicted in Figure 2.2, is the energy gap between the vacuum level and the maxima of the localized muffin tin potential. E_o is

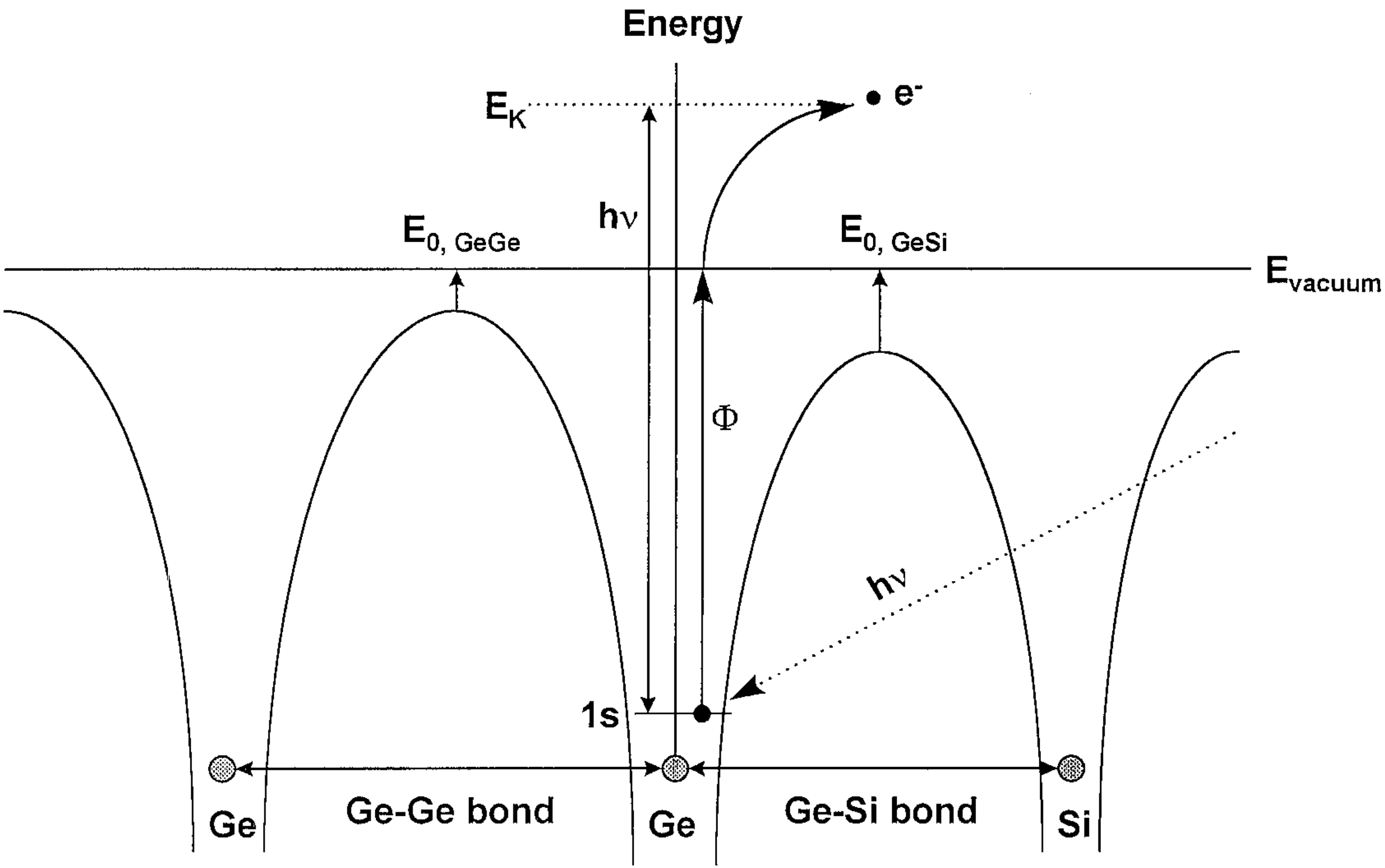

Figure 2.2 - Muffin tin potential diagram and the photon absorption process.

often used as a corrective term that accounts for shifts in the k-scale origin between two systems (i.e. unknown and model) which may be a result of chemical bonding effects, core hole relaxation, inaccuracies in choosing the k-scale origin in data analysis, etc.

As the photoelectron wave exits the potential well of the absorbing atom, it encounters the surrounding co-ordination shells, and a fraction of it is backscattered towards the central atom. Constructive and destructive interference occurs between the outgoing and backscattered photoelectron waves (Figure 2.3a), resulting in a final state quantum mechanical effect which produces the observed oscillations in the absorption coefficient. The backscattering can occur as single scattering events, which accounts for the majority of the EXAFS signal (Figure 2.3b), or as multiple scattering events, which accounts for much of the NEXAFS signal (Figure 2.3c). Figure 2.1 presents the Si K-edge spectrum of c-Si as a typical XAFS spectrum, showing both the NEXAFS (magnified in inset) and the EXAFS portions of the XAFS spectrum. EXAFS analysis is greatly simplified by assuming that all photoelectron scattering events are single scattering elastic events (basically an assumption that the EXAFS signals is simply the sum of all individual single scattering path signals). Thus, it is important that multiple scattering effects do not contaminate EXAFS data, i.e. that NEXAFS data and EXAFS data are cleanly separated. At low photoelectron energies (i.e. just above the edge jump, 0-20 eV), multiple scattering is greatly enhanced, producing the prominent near edge features that make up the NEXAFS; however, at higher photoelectron energies, multiple scattering is greatly reduced, as the rapidly varying multiple scattering oscillations tend to cancel out. This permits the "separation" of the two phenomena, and thus, much of the multiple scattering contributions can be removed by data truncation, leaving the single scattering effects which dominate the EXAFS [S88].

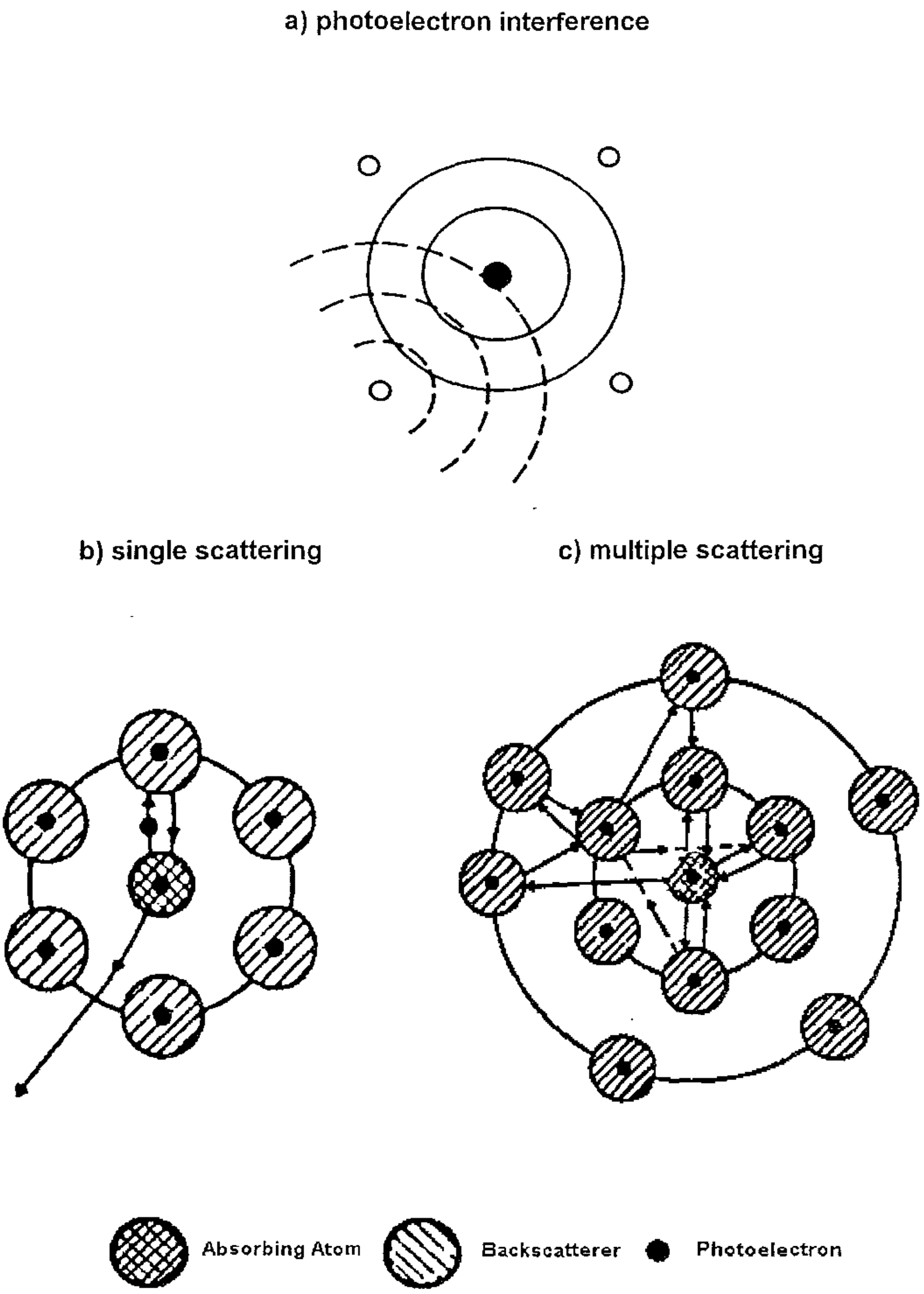

a) photoelectron interference

b) single scattering

c) multiple scattering

Figure 2.3 - Schematic of photoelectron backscattering.

Figure 2.4 depicts the Ge K-edge energy space data for crystalline germanium, along with the truncated portion that represents the EXAFS. Within the EXAFS data, the signal is dominated by the backscattering of the first co-ordination shell. Higher shell signals are present, but are weaker in intensity, due to a) their relatively complex and/or obstructed paths, b) increased damping from inelastic scattering, and c) increased damping from structural and dynamic disorder inherent to the material.

The periodicity of EXAFS becomes evident in k-space, where the data is not measured in terms of photoelectron energy, but wave vector, **k**. The EXAFS signal in k-space is labeled χ**(k)**. It is derived from the experimental μ**(k)** according to:

$$\boxed{\chi(k) = \frac{\mu(k) - \mu_o(k)}{\mu_o(k)}} \qquad \textbf{(2.4)}$$

where χ**(k)** is the background-subtracted and normalized wave-vector dependent interference function (the EXAFS), μ**(k)** is the measured absorption coefficient, converted to k-space from μ**(E)** using equation 2.3, and μ_0**(k)** is the non-oscillatory absorption coefficient (the "background" signal). Figure 2.5 depicts the k-space data, (a) before and (b) after background subtraction (procedure detailed below). In general, EXAFS spectra have ranges of 2 to 10-16 Å^{-1} (approximately 400 data points). Additionally, a term not included in equation 2.4, but is often used is a **k**$^{\mathbf{n}}$ weighting term (on the left side of the equation), which represents the k-weighting of the data. This term allows the experimenter to change which portion of the χ**(k)** spectrum is emphasized: low k-weights (0,1) favor low-k information, while high k-weights (k = 2, 3) favor higher-k information.

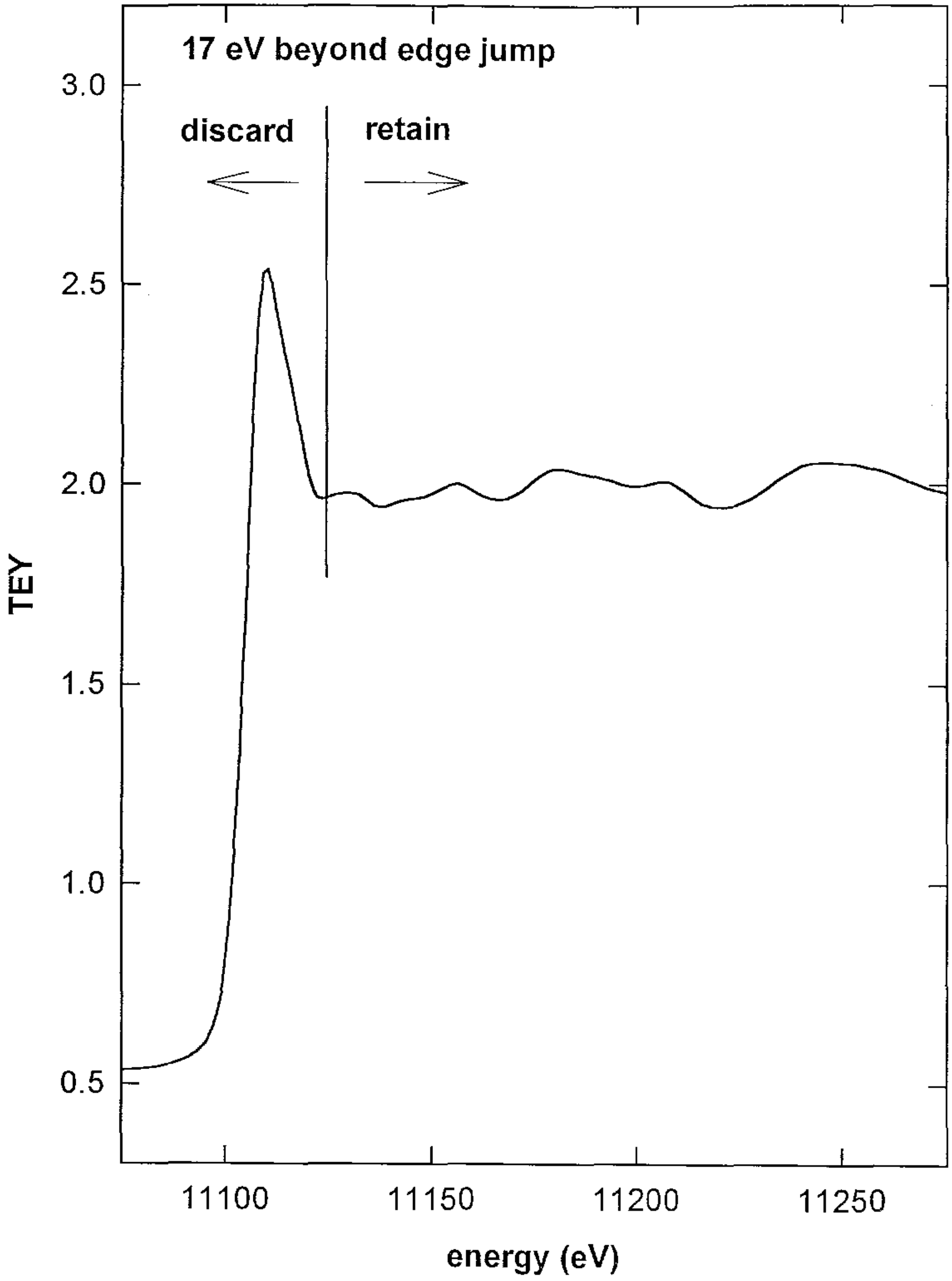

Figure 2.4 - Simple low energy truncation for Ge K-edge absorption spectrum for crystalline Ge.

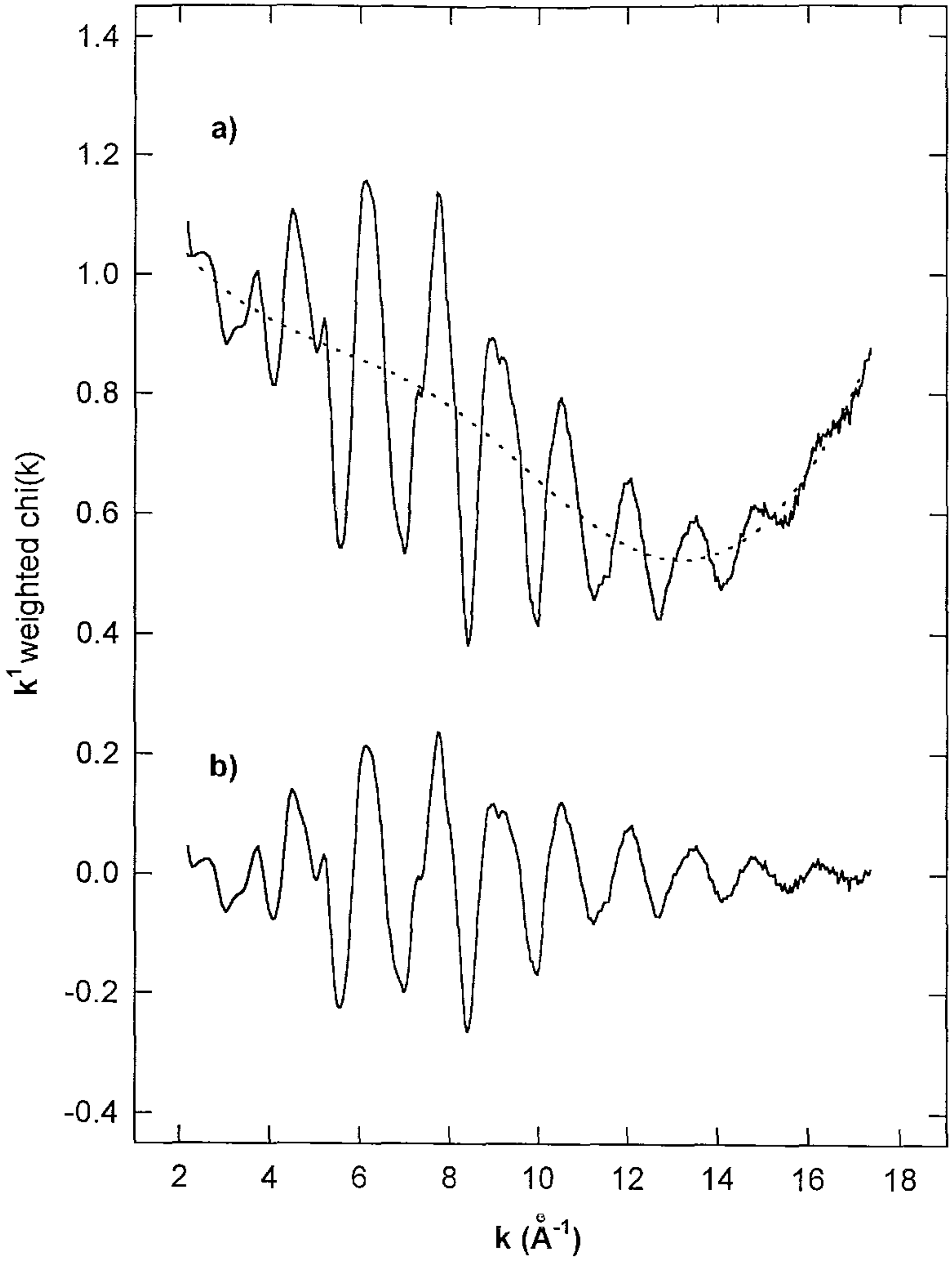

Figure 2.5 - Background removal for EXAFS data of c-Ge: a) isolated EXAFS with appropriate background, and b) after background subtraction and subsequent normalisation. Spectrum a) has already been k^1 weighted, and had a linear background subtracted.

Assuming that any disorder in the material is small and has a Gaussian distribution, and that the single scattering approximation holds well, EXAFS can be modeled by the EXAFS equation [S88, L+81]:

$$\boxed{\chi(k)=\frac{-1}{k}\sum_j \frac{S_o^2 N_i}{r_j^2}\exp\left(\frac{-2r_j}{\lambda}\right)\exp\left(-2k^2\sigma_j^2\right)f_j(k)\sin\left(2kr_j+\delta_j(k)\right)} \qquad \textbf{(2.5)}$$

Equation 2.5 is a collection of several phenomena which have well-defined physical interpretations. The EXAFS signal, $\chi(\mathbf{k})$, is a summation of the individual contributions of **j** types of co-ordinated atoms, each at a distance of $\mathbf{r}_j$ from the central atom. In the case of regular crystals, such as Ge, it is convenient to organize the EXAFS contributors into shells of atoms, such that the nearest neighbors represent the first shell, the next nearest neighbors represent the second shell, etc. In this manner, one can simply define **j** shells as contributors to the EXAFS, each with a co-ordination number $\mathbf{N}_j$ and bond length $\mathbf{r}_j$, specific to the co-ordination shell. In the case of a zinc blende structure, such as GaAs, the first shell and second shells are of different composition (one is always a group III element, the other is a group V); however, this presents no problem since the shells are separate. In the case of a random alloy such as SiGe, because there is only a small difference between homo- and heteroatomic bond lengths, Si and Ge backscatterers are both considered to be part of a mixed first shell.

The next term, S_o^2, is referred to as the passive electron reduction term, which accounts for EXAFS damping due to shielding effects of non-participant electrons in both the central and backscattering atoms, as well as many-body relaxation effects [SBH80]. The subsequent two terms represent damping effects as functions of wave vector **k**. The first exponential term, containing λ, the electron mean free path of the material represents the damping effects due to inelastic scattering of the photoelectron. Inelastic scattering causes a change in kinetic energy, and hence, wave vector **k** of the photoelectron, thereby bringing its contribution to the EXAFS out of phase with those photoelectrons that have undergone purely elastic scattering. The result is an exponential decay in EXAFS intensity with increasing energy. The next term is a Debye-Waller-type term, representing the effects of dynamical and structural disorder. The term contains σ^2_j, which is defined as the mean square fluctuation in relative position of the central and backscattering atom j. Note that in diffraction, the Debye-Waller (DW) term is a one body average, while in EXAFS it is a two body term. The version of the EXAFS equation presented here requires that bond length disorder has a Gaussian distribution. Other versions of the equation can account for non-Gaussian disorder distributions by inclusion of higher order terms in the description of the pair correlation of the jth shell. This approach is called a cumulant analysis. It involves the inclusion of power series terms into the amplitude functions and phase shifts for the absorber-backscatterer pair, which account for the non-Gaussian disorder distribution. In general, this is used only for highly detailed analysis of at most moderately disordered structures [CRI88].

The final terms are element-specific. The wave vector dependent amplitude of 180° backscattering, **f(π,k)**, is characteristic to a given element, and is used to readily identify the major backscatterers. The last term, a sine wave, describes the oscillation in **μ(k)** that is a result of the interference between the forward and backscattering photoelectron waves. Within the sine term, there are two different terms that determine the period of the oscillation. The **2kr** term represents the distance traveled by the photoelectron wave in leaving and returning to the absorbing atom. The second term,

$\delta_j(k)$, is often decomposed into two terms: $2\delta_{central}(k)+\delta_{backscatterer}(k)$, both of which are elementally specific phase shifts (which provides another means by which to chemically identify the surrounding atoms). These shifts are due to the interaction of the outgoing and backscattered photoelectron with the central and backscattering atoms' passive electrons. Note that phase shifts for L-edge spectra differ slightly from K-edge spectra, owing to the different symmetries, and hence, allowable transitions.

Upon first exposure, the EXAFS equation appears extremely complex; however, it is merely the products of amplitude functions and sine waves summed over successive shells of atoms. The various terms within this model can be grouped to provide a more simple picture. An amplitude function, $A_j(k)$, can be defined as the "strength" of the backscattering. Within this term one can include the geometric and inelastic scattering corrections, such as the co-ordination number N_j, the exponential terms, containing the DW term and electronic mean free path, and the atom-specific backscattering function $f(\pi,k)$. The sine term contains phase shifts experienced by the photoelectron. Together with the newly defined $A_j(k)$ term, the EXAFS equation in equation 2.5 is simplified to:

$$\boxed{\chi(k)=\frac{-1}{k}\sum_j A_j(k)\sin\left(2kr_j+\delta_j(k)\right)} \qquad \textbf{(2.6)}$$

2.3 Extracting Quantitative Data

To even a well trained eye, k-space data alone does not provide easily interpretable results. It is often difficult to discern any quantitative physical information in this format, due to such things as overlapping signals from multiple shells, complex backscattering amplitudes (such as those for heavy elements), residual background effects, etc. Fourier transformation of the data, however, provides a very quick and easy way to alleviate this problem. A discrete series of sine waves is an ideal data set for discrete Fourier transformation. Using the Fast Fourier Transform algorithm [CT65], one can Fourier transform the k-space data into r-space, producing radial structure data. In EXAFS analysis, the Fourier transform data, $F_n(r)$, is obtained by use of the following Fourier transform [L+81]:

$$\boxed{F_n(r) = \frac{1}{\sqrt{(2\pi)}} \int_{k_{\min}}^{k_{\max}} W(k) k^n \chi(k) \exp(2ikr) dk} \qquad (2.7)$$

where k_{max} and k_{min} are the limits of the experimental data, and $W(k)$ is a window function used to isolate the $\chi(k)$ spectrum, an example of which is the Hanning function:

$$\boxed{W(k) = \frac{1}{2}\left\{1 - \cos 2\pi\left(\frac{k - k_{\min}}{k_{\max} - k_{\min}}\right)\right\}} \qquad (2.8)$$

In equation 2.8, $W(k)$ has a value of zero outside the chosen window range and 1 inside the range, with steep slopes at the boundary representing the increment. This produces the correct number of data points required for Fast Fourier Transform algorithm, originating from zero in k-scale (even though the data may not begin until approximately 2 $Å^{-1}$) and extending until a code-defined number of points is reached (2^n - typically, n = 9 or 10, corresponding to 512 or 1024 data points). The steepness of the window "sills" is variable according to preference. Windows with infinitely steep sills are termed zero-filling windows, since every point outside the data is forced to zero, while the data itself is unchanged. Windows with less steep sills, termed apodizing windows (the Hanning window is an example of this), slowly reduce the amplitude of the edge data to match the (essentially) zero signal outside the data range. In general, any windowing will add some distortion to $\mathbf{F_n(r)}$, and this is something that must always be considered when choosing windows.

Fourier transforms produce complex results - an imaginary signal, as well as a real signal; however, the magnitude of $\mathbf{F_n(r)}$ is the most useful portion for visualizing the structural content of an EXAFS signal, since it depicts an easily interpreted intensity vs. **r** plot (see Figure 2.6)). Unfortunately, one still cannot directly derive quantitative data, such as bond lengths or co-ordination numbers, from the magnitude of $\mathbf{F_n(r)}$. Even peak positions, which seem relatively clear, cannot be used, since peaks in the $\mathbf{F_n(r)}$ plot are displaced from the physical $\mathbf{r_j}$ values, on account of the scattering phase shifts, $\delta_j(\mathbf{k})$. In order to obtain quantitative results, one must continue with the analysis.

Back Fourier transformation (Fourier filtering) provides a convenient way to separate signals from different shells. Using a window function, one can isolate the signal from a single or a reduced number of coordination shells, and Fourier transform the filtered data back into k-space again (Fourier filtered k-space is referred to as q-space in this work):

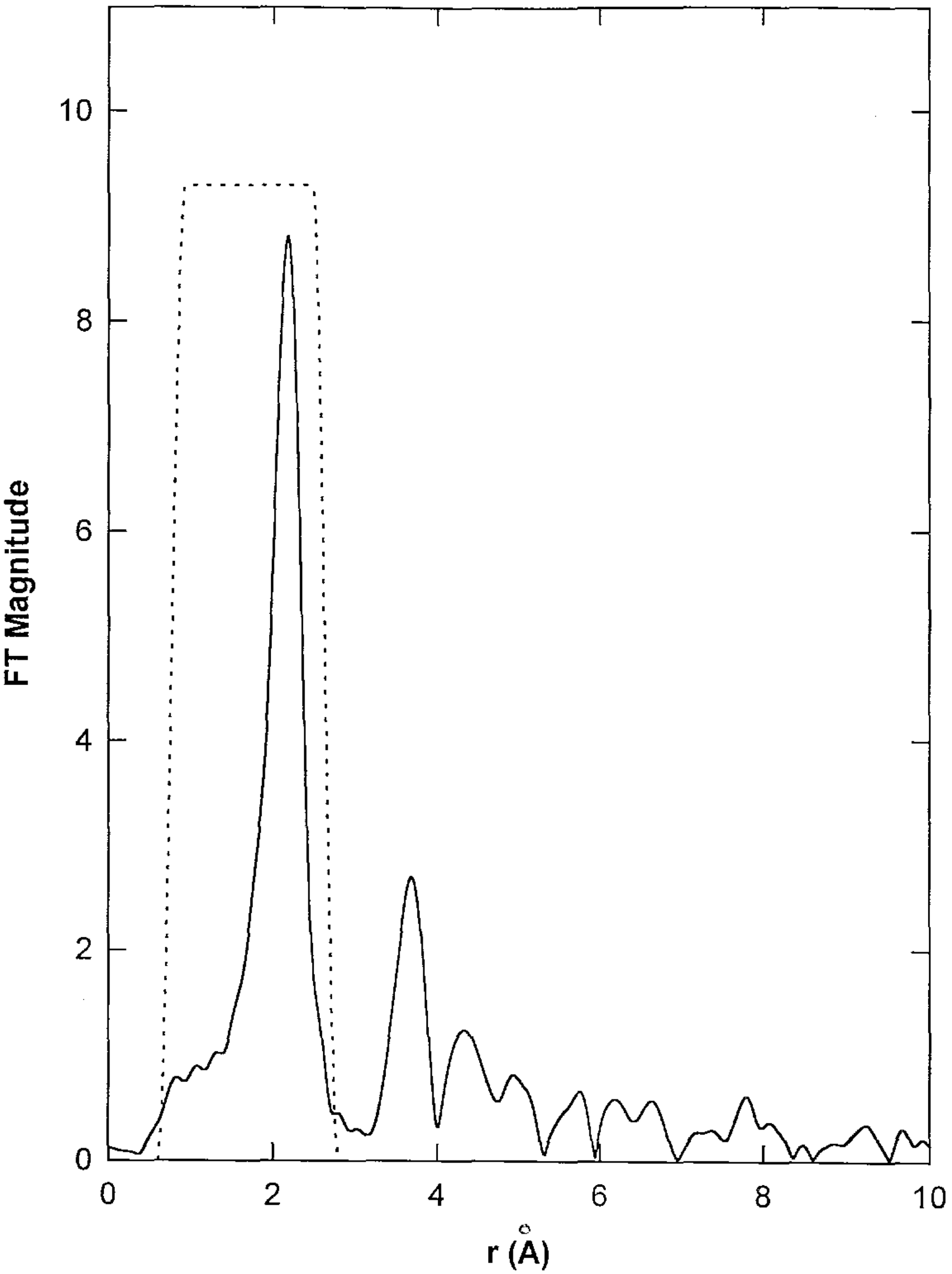

Figure 2.6 - Fourier transform of Ge K-edge EXAFS of crystalline Ge, along with a Fourier filter for first shell isolation.

$$\boxed{\tilde{\chi}(q) = \frac{-1}{\sqrt{2\pi}} \int_0^\infty W(r) \frac{F_n(r)}{kr^2} \sin[2kr + \delta(r)]dr} \qquad \textbf{(2.9)}$$

where $\tilde{\chi}$ **(q)** is the Fourier filtered EXAFS. Figure 2.6 depicts **F$_n$(r)** data with an appropriate filtering window over the first shell signal. The result of the back transform, Figure 2.7, is an EXAFS spectrum depicting $\tilde{\chi}$**(q)** data for the isolated first shell, overplotted with the original **χ(k)** data. In this figure, the higher shell effects in the **χ(k)** (the higher frequency oscillations) become significantly more noticeable.

Quantitative results are obtained by non-linear curve fitting to the EXAFS data. The fit is usually performed with $\tilde{\chi}$**(q)** data, though at least one fitting software package fits to a prescribed region of **F$_n$(r)** as well as $\tilde{\chi}$**(q)** [N95]. The fit itself is usually optimized by a least squares minimization, of the form:

$$\boxed{S = \sum_i^n (\tilde{\chi}_i^F - \tilde{\chi}_i)^2} \qquad \textbf{(2.10)}$$

where **S** is the sums of squares measurement of the difference between the “guessed” EXAFS and the Fourier filtered EXAFS. In the fitting, **S** is minimized in order to obtain the best fit. Also in equation 2.10 are the terms **n**, the number of data points, $\tilde{\chi}_i^F$, the experimental Fourier filtered data points, and $\tilde{\chi}_i$, the EXAFS spectra calculated from specific values for the fitting parameters, i.e. r_j, N_j, σ_j, and $E_{0,j}$. Other approaches to least squares EXAFS analysis have higher DW cumulants and/or the **S$_0$^{2}** term included as fitting parameters as well the main four described above [N95].

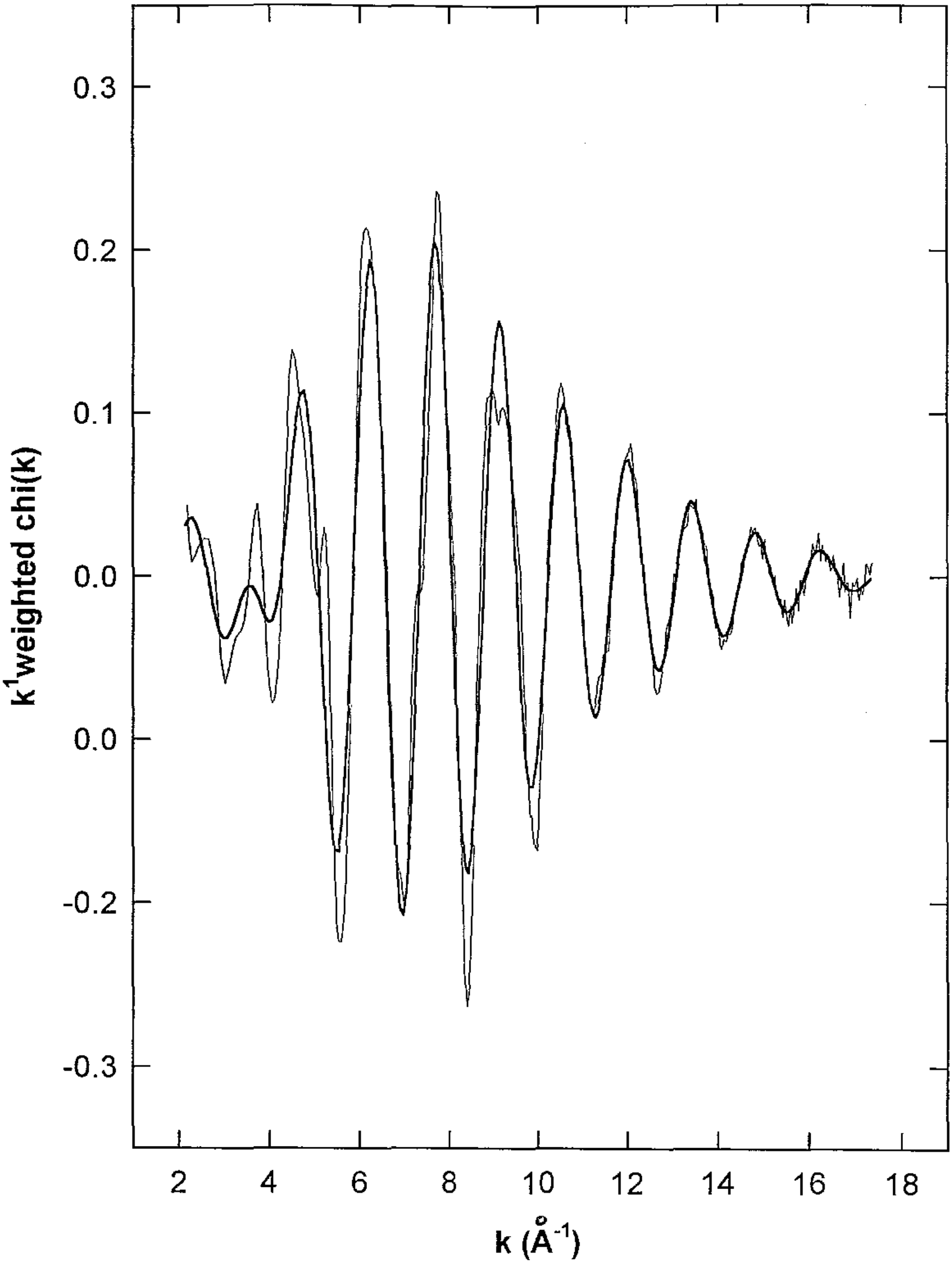

Figure 2.7 - Ge K-edge EXAFS (thick) and Fourier filtered first shell spectra (thin).

Fitting requires the use of model phase shifts, $\delta_j(\mathbf{k})$, and atom-specific amplitude functions, $\mathbf{f_j(\pi,k)}$, for each type of co-ordination being fitted. For example, in the case of SiGe, four models are needed for the Si and Ge edge data: Si-Si bonding, Ge-Ge bonding, Si-Ge bonding, and Ge-Si bonding (note that Si-Ge bonding and Ge-Si bonding are very different - the first atom, the central absorbing atom by convention, is co-ordinated to a dramatically different backscatterer in each case). One has several choices of model amplitude and phase functions. The best option for SiGe would be to use dilute alloys, i.e. a $Si_{0.05}Ge_{0.95}$ alloy for Si-Ge bonding, and a $Si_{0.95}Ge_{0.05}$ alloy for Ge-Si bonding. This would, of course, require the pre-knowledge for the heteroatomic bond length, though one could use calculated values. Unfortunately, as will be described in detail in Chapter 4, low %Si samples are beyond the capabilities of our experiment; thus, this option is not available to us.

A historically popular option was to use model compounds of well known structure that are similar to the experimental system of interest, and extract phase shifts and amplitude functions from their EXAFS [L+81]. It is not even necessary that the same elements are present in the models and the fitted sample; in reality, amplitude functions and phase shifts are very similar from one element to the next in the periodic table (but differences become readily apparent for larger steps - i.e. the amplitude functions of Si and Ge are vastly different, since they are separated by a row in the periodic table) [LLB95]. For the case of SiGe alloys, options include using experimental data for crystalline Si and Ge, as well as GaP for mixed cases, i.e. for Ge backscattering around Si and vice versa (Ga is very close to Ge, while P is very close to Si in the periodic table; additionally, crystallographic data for GaP is readily obtainable). Alternatively, one can use molecules for models. Again, in the case of Si-Ge interactions, one could use $Ge(SiH_3)_4$, or $Si(GeH_3)_4$ (note that H, having a very small electron density, has negligible contribution to XAFS, and as such, will not contaminate the spectrum by forming a second shell or multiple scattering paths).

A newer alternative involves using a software package entitled FEFF6 [R+91]. This package calculates theoretical *ab initio* XAFS for user-defined structures, and permits considerable tailoring for individual requirements. In the case of SiGe, one can substitute calculated XAFS for a Ge substitutional impurity in Si and vice versa as a replacement for GaP. A variation of this [LLB95] is to use FEFF to *correct* experimental models such as GaP, in an attempt to combine the best aspects of each. Today, the EXAFS community seems to prefer the use of FEFF6.01 calculated results over any other models; however, in some cases (notably covalent solids), FEFF does not perform well, and one is obliged to pursue other avenues [N95]. In general, each of these models has various benefits and drawbacks. Their specific attributes as applied to the SiGe system will be discussed in detail below.

Unfortunately, non-linear curve fitting is a difficult task. Within the EXAFS parameter space, there exist a number of secondary minima which often impedes the progress in finding the true, global minimum (i.e. the best result). The existence of these local minima can be attributed to the significant correlation that exists between EXAFS parameters. Within equation 2.5, one notices that pairs of EXAFS parameters tend to have similar effects in producing the EXAFS signal. Both co-ordination numbers and DW factors determine EXAFS amplitudes. Similarly, the interatomic bond distance and E_o terms are highly correlated, since both play important roles in phasing of the sine wave. When dealing with correlated parameters in curve fitting, it is often very difficult to separate their respective roles, and this can result in highly unexpected (and often non-physical) results.

Despite all this, EXAFS analysis is workable. Depending upon the complexity of the system of interest, fitting can be relatively straight-forward, or extremely complex. Regardless, the end result (i.e. quantitative information regarding the local structure of the material of interest) is well worth the difficulty experienced in the analysis.

3.0 LITERATURE REVIEW AND GOAL OF MY WORK

This chapter describes the results of previous theoretical and EXAFS studies of SiGe materials. In addition, a model for use in characterizing local structure, developed by Thorpe and co-workers, will be presented. The chapter concludes with a statement of the goals of this work.

3.1 Theoretical Studies Of Local Structure In SiGe Materials

The local structure of SiGe alloys is a complex problem that is proving difficult to unravel. X-ray diffraction studies have shown that SiGe alloys have average lattice parameters that mostly follow Vegard's law, but with a slight negative deviation [K+95, K+92, DEP64]. The slight bowing, a phenomenon which is not fully understood, has been attributed to a free energy reduction in forming heteroatomic bonds, rather than homoatomic [K+95]. These diffraction results, while useful, do not provide much information regarding the local structure of SiGe alloys. Theoretical studies are useful methods for modeling materials, especially local structure where experimental results are difficult to obtain.

An important theoretical paper on alloy structure was produced by Martins and Zunger [MZ84]. In this work, the authors studied heteroatomic bond lengths at the impurity limits. For SiGe, they calculated that at dilute levels, $\mathbf{r}_{\mathbf{SiGe}}$ and $\mathbf{r}_{\mathbf{GeSi}}$ for Si in c-Ge and Ge in c-Si were 2.419 Å and 2.380 Å, respectively. Figure 3.1 depicts their results. The next important paper dealt exclusively with SiGe alloys. This work, by

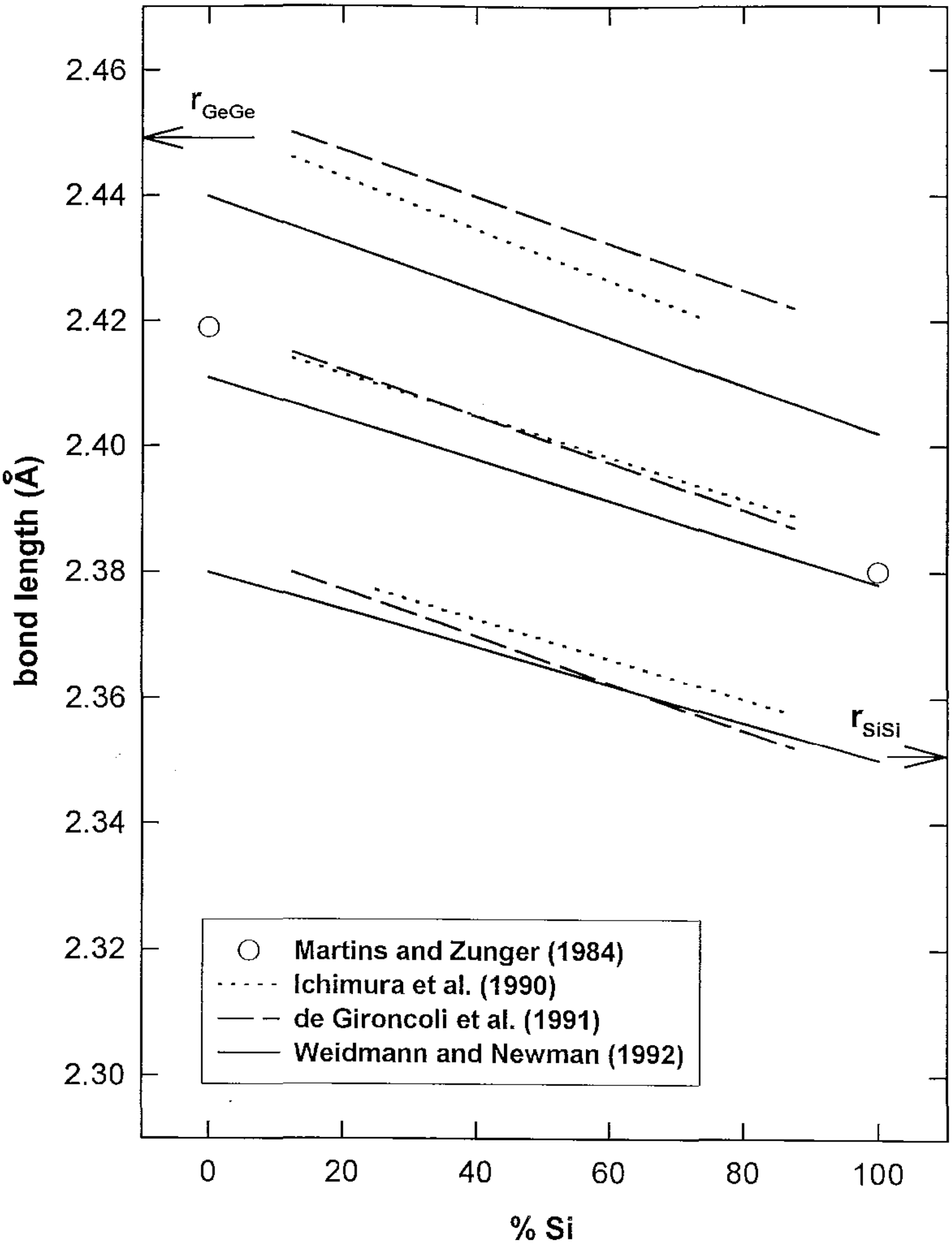

Figure 3.1 - Calculated results for bond lengths in SiGe alloys. The arrows correspond to the crystallographic bond lengths in c-Ge (upper) and c-Si (lower).

Ichimura et al. [I+90] detailed how the authors used a zinc blende structure of SiGe as a model of random SiGe alloys in order to calculate the three nearest-neighbor bond lengths. Their results were in excellent agreement with Martins and Zunger [MZ84] (see Figure 3.1), showing a distinctive linear trend with significant Vegard-like behavior.

These works were followed by papers from de Gironcoli et al. [GGB91] and Weidmann and Newman [WN92]. de Gironcoli et al. performed *ab initio* Monte Carlo simulations of random SiGe alloys, in another attempt to study the bond length dependence upon composition. Their bond length results were in very good agreement with that of Ichimura et al. [I+90] and Martins and Zunger [MA84] (see Figure 3.1). Of interest though, was the prediction in their results that the lattice parameter of SiGe alloys shows upward (positive) bowing, rather than downward (negative), as experimentally determined previously [K95, DEP64]. Weidmann and Newman [WN92] published a thorough study of the problem of elastic network relaxation, using SiGe alloys as their main example. Among their significant findings was a general agreement with others [GGB91, I+90, MZ84], in that the three bond lengths in SiGe alloys were distinct, and slightly dependent upon composition (see Figure 3.1).

A relatively new theoretical method of describing lattice accommodation has been proposed, entitled the CT theory, for the authors Cai and Thorpe [CT92, MT92]. Using the Kirkwood model harmonic interatomic potential [K39], they have defined a *topological rigidity parameter,* a**, that describes the resistance of a given lattice to a radial expansion from a central atom:

$$\boxed{a^{**} = \frac{u_{AB}}{F_{radial} / \alpha_{AB}}} \qquad \textbf{(3.1)}$$

where F_{radial} is the radial force from the central atom pushing away a nearest neighbor atom, α_{AB} is the radial force constant for the AB bond, and u_{AB} is the displacement of the nearest neighbor atom relative to its natural bond length. For **a**** = 1, the lattice is considered "floppy", and every bond adopts its natural length, which is Pauling's limit. For **a**** approaching 0.0, the lattice is considered perfectly rigid, and every bond extends or contracts to fit within the rigid unit cell, defined by the lattice parameter, which is Vegard's limit. Within these bounds, 0<**a****<1 describes a mixed behavior. For SiGe alloys, chemically specific bond lengths can be related to **a**** by the following:

$$\boxed{\begin{array}{ll} a) & r_{SiSi} = r_e - (1-x)a^{**}(r^o_{GeGe} - r^o_{SiSi}) \\ b) & r_{GeGe} = r_{SiSi} + a^{**}(r^o_{GeGe} - r^o_{SiSi}) \\ c) & r_{GeSi} = \tfrac{1}{2}(r_{GeGe} + r_{SiSi}) \\ d) & r_e = x r^0_{SiSi} + (1-x) r^0_{GeGe} \end{array}} \qquad \textbf{(3.2a-d)}$$

where r_e is the virtual crystal bond length, x is the Si fraction, r^o_{xx} is the natural bond length, and r_{xx} is the chemically specific bond length in the bulk alloy of composition x. Using bond length results from EXAFS measurements, one can obtain a value for **a****, for example:

$$\boxed{a^{**} = \frac{r_{GeGe} - r_{SiSi}}{r^0_{GeGe} - r^0_{SiSi}}} \qquad (3.3)$$

Thus, using this methodology, one has a way in which to use EXAFS results to characterize the lattice rigidity in terms of a single parameter, **a****. The major result of the CT theory is a prediction that a plot of the SiSi, SiGe, and GeGe bond lengths vs. composition should have three equally spaced parallel lines having a slope which is closely related to the value of **a****. This is in very good agreement with the published theoretical results presented above [WN92, GGB91, I+90]. Note that the results of the CT theory are based upon the assumption that $\mathbf{r^0_{SiGe} = \frac{1}{2}(r^0_{SiSi} + r^0_{GeGe})}$ (Equation 3.2c). They defend this assumption, by making the point that one would not expect a significant bond length change, since there will not be significant charge transfer effects, etc. [CT92, MT92, GGB91]. Effectively, this is a prediction that the heteroatomic bond length in a 50% Si alloy should be exactly 2.401, regardless of the value of **a****. Some experimental results are in reasonable agreement with this prediction [ANS94, A+92, N+88], while others have produced results for $\mathbf{r_{SiGe}}$ being slightly lower than the CT assumption [W+91, I+85].

The parameter **a**** was first defined as a complex function of the ratios of the elastic linear and elastic shear force constants. Formally, the **a**** parameter is defined by a series of Green's functions, the derivation of which is too long and complex for inclusion in this work (see [CT92] for a complete description); however, **a**** can be approximately described by:

$$\boxed{a^{**} = \frac{1 + 1.249(\beta/\alpha)}{1 + 3.600(\beta/\alpha) + 1.171(\beta/\alpha)^2}} \qquad (3.4)$$

where β is the angular elastic force constant, α is the linear elastic force constant, and the numerical factors are constants used to fit the interpolation curve to the **a**** curve defined by the series of Green's functions.

From bulk elastic and shear modulii, Thorpe et al. determined that for most semiconductors, the ratio of the angular and linear force constants, (β/α), tends to be between 0.10 and 0.20, with SiGe probably fitting into the high end of this range [CT92, MT92]. Qualitatively, this agreed with the results of Martins and Zunger [MZ84]. Assuming that (β/α) = 0.20, the authors used calculated bond lengths from de Gironcoli et al. [GGB91] to estimate that **a**** in SiGe alloys was 0.707 [MT92]. The lines for the data of de Gironcoli et al. in Figure 3.1 represent **a**** for this value.

3.2 EXAFS Studies Of SiGe Materials

The experimental results in the literature have not been so harmonious as the theoretical results presented above. In contrast to the approximately 30% Vegard character to the bonding in SiGe materials, several groups have presented EXAFS results that provide evidence supporting the Pauling limit [K+92, MTC91, W+91, N+88, F+86, I+85]. Figure 3.2 depicts their results.

The first study, by Incoccia et al. [I+85], was a Ge K-edge EXAFS study of hydrogenated amorphous SiGe alloys (a-SiGe:H). Making the assumption that the r_{GeGe} values were equal to that of crystalline Ge for all compositions, the authors performed single shell fits for their range of samples, using theoretically corrected experimental dilute SiGe alloy models. From their results, they concluded that r_{SiGe} = 2.38 Å (errors not given) for their amorphous alloys, independent of composition.

Following this, Filliponi et al. [F+86] made Si K-edge EXAFS measurements of a similar series of a-SiGe:H alloys. Using the most dilute alloy as a model, Filliponi et al.

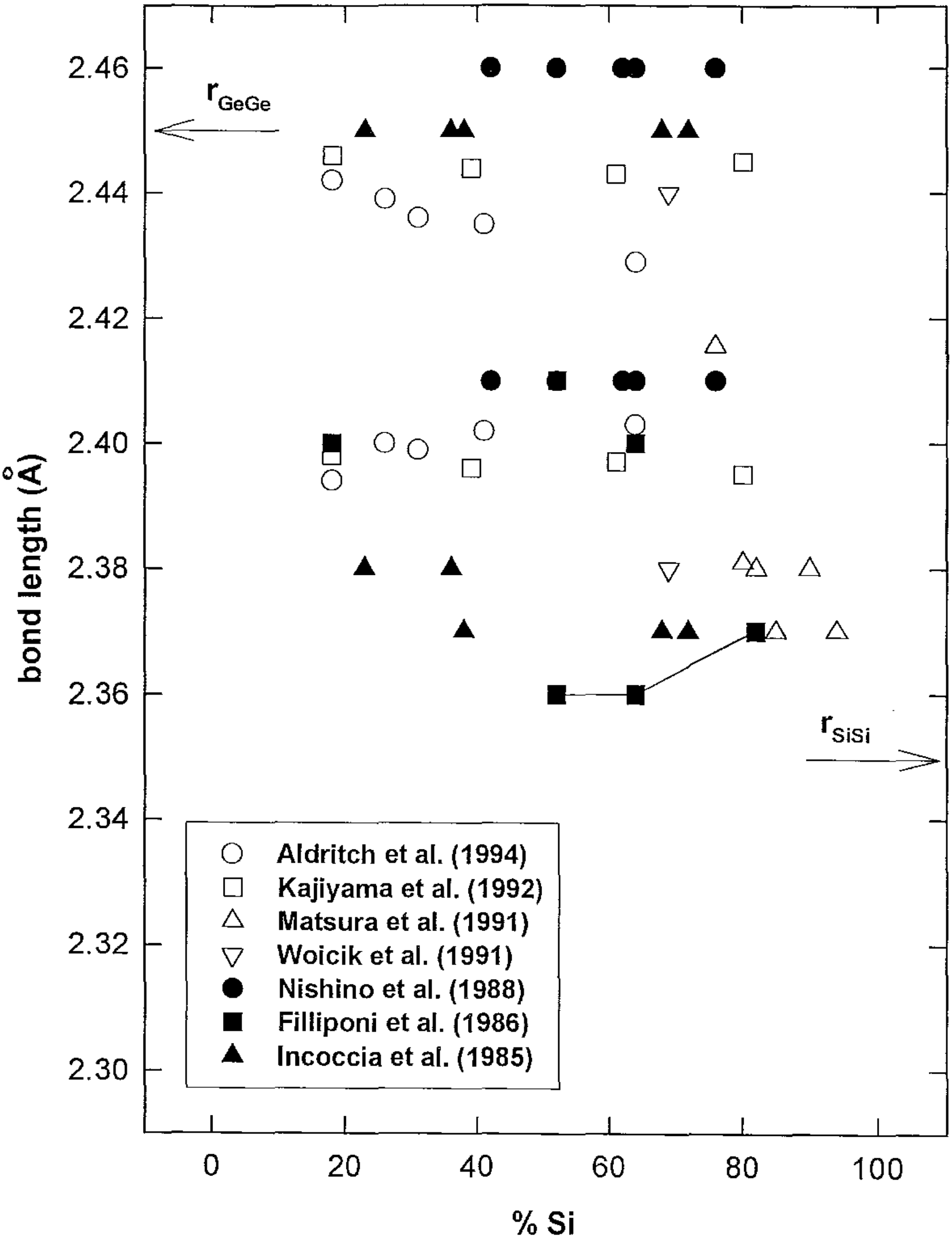

Figure 3.2 - The experimental r_{GeGe} and r_{GeSi} results from the literature. The only three points for r_{SiSi} are connected by al line, for ease in viewing. The solid symbols are for amorphous samples, while the open symbols are for crystalline samples. Again, the arrows correspond to the crystallographic bond lengths in c-Ge (upper) and c-si (lower).

determined from fitting results that r_{GeSi} = 2.40 Å (±0.02) and r_{SiSi} = 2.36 Å (±0.02), in apparent agreement with the results of Incoccia et al. [I+85], i.e. Pauling-type bonding was dominant. We note that the quoted error bars in their work are probably too large to make this conclusion. Furthermore, Filliponi et al. failed to mention what bond length they chose for their model, and subsequent inclusion in the fitting.

Another study, by Nishino et al. [N+88], also presented Ge K-edge EXAFS results for a-SiGe:H alloys. Using in-house calculated models, Nishino et al. also found that these materials adhered to Pauling type bonding, having r_{GeGe} lengths of 2.460 Å (±0.005) and r_{SiGe} of 2.410 Å (±0.005). The bond lengths differed slightly from the results of Incoccia et al.; however, the overall result of compositional independence was in complete agreement (see Figure 3.2).

The applicability of the experimental results for amorphous alloys to crystalline materials is questionable. It is well known that bonding differs significantly between amorphous and crystalline materials [CT92. MT92]. Specifically, in an amorphous material, one expects the disorder to permit significant bond extension, such that there is virtually no matrix rigidity, i.e. Pauling-type behavior. Crystalline materials, having much less disorder, should have more rigid lattices. Thus, the conclusions drawn above by Incoccia et al., Filliponi et al., and Nishino et al. are probably not valid for the case of crystalline SiGe alloys [MT93].

Matsuura et al. [MTC91] performed Ge K-edge studies for a series of strained, Si rich (82%-94% Si) MBE- and CVD-grown SiGe single crystal epitaxial films. Using c-Ge and GaP for models, they performed single shell fits for their range of samples. From their fitting results, they determined that the values of r_{SiGe} were equal to 2.375 ± 0.02 Å, independent of composition (see Figure 3.2). While this may provide evidence for Pauling type bonding, the magnitude of their error bars is greater than any expected compositional variation over such a small composition range [MT92].

Woicik et al. [W+91] performed Ge K-edge measurements of a strained crystalline $Si_{.70}Ge_{.30}$ epitaxial base layer in SiGe HBTs grown by chemical vapor deposition (CVD) on Si(001). Fitting of single shell data was performed using c-Ge and GaP models. In their study, the authors determined that r_{Ge-Ge} was 2.44 ± 0.02 Å, while r_{GeSi} was 2.38 ± 0.02 Å, effectively equal to the values in crystalline Ge (2.4498 Å) [I69] and amorphous SiGe (2.38 Å) as quoted by Incoccia et al. [I+85], respectively. From this result (shown in Figure 3.2), the author suggested that a Pauling type description was best for bonding in SiGe alloys.

A subsequent EXAFS study of SiGe alloys, by Kajiyama et al. [K+92], was much more extensive. For this study, amorphous SiGe alloys spanning a range of compositions from 20-100% Ge were grown by CVD on polycrystalline graphite substrates using Si_2H_6 and GeH_4 feed gases. The samples were then annealed for 5h at 700°C, forming polycrystalline layers (crystallinity was confirmed by x-ray diffraction). Ge K-edge EXAFS of these samples were obtained, with subsequent fitting using calculated models. They obtained results of r_{Ge-Ge} = 2.44 Å and r_{GeSi} = 2.40 Å (errors not given) for the entire range, essentially independent of alloy composition (shown in Figure 3.2). This was supposedly clear evidence for Pauling type bonding in SiGe alloys.

Contradicting these results were more recent work from others, producing evidence that supports a mixed regime (mostly Pauling with some Vegard-like character) for SiGe. The work of Mousseau et al. [MT93] was concerned with interpreting the results of Kajiyama et al. [K+92]. In their paper, Mousseau et al. considered the plausibility of strictly Pauling type behavior, and determined by calculations that this would require clearly unphysical elastic constants in the SiGe bonding. For the results of Kajiyama et al., Mousseau et al. calculated that their Pauling type results suggested $a^{**} = 0.98$, which would correspond to a (β/α) ratio of less than 0.01 [MT93]. They argued that this was far too low to be physically plausible, especially in light of bulk elastic and shear modulii data for SiGe alloys that indicate that the (β/α) ratio should be close to 0.20. Additionally, Mousseau et al. calculated that the conclusions of Kajiyama et al. would result in r_{SiSi} values (2.16 - 2.34 Å) below that found in c-Si (2.352 Å). To account for this disagreement, Mousseau et al. explored possible error sources in the work of Kajiyama et al., and suggested that their CVD samples were highly contaminated with hydrogen, in the form of large, planar hydride cracks within the polycrystalline films. Hydrogen does not backscatter, and is virtually invisible to EXAFS measurements. Mousseau et al. reasoned that such cracks would significantly degrade the rigidity of the crystal lattices. This would permit the bonds in SiGe to extend out to the Pauling limit, and perhaps approach the results of the EXAFS studies of a-SiGe:H alloys cited above [I+85, N+88]. Mousseau et al. admitted that the amount of hydrogen required to have this effect was quite high (45-65% hydrogen in the alloy).

The most recent EXAFS results by Aldritch et al. [ANS94], are considered the best to date. For a range of relaxed, MBE-grown epitaxial SiGe alloys (relaxation confirmed by x-ray diffraction), the authors obtained Ge K-edge EXAFS measurements. Using FEFF3.11 calculations for models, Aldritch et al. produced bond length results which indicated that SiGe alloys obey mixed-type (Figure 3.2, 3.3), showing detectable compositionally-dependent first shell bond lengths, and thus, a partial Vegard-like character in reasonable agreement with the theoretical predictions [MT93, WN92, GGB91, I+90, MZ84]. In this paper, the authors were able to show that the previous Ge K-edge results of Kajiyama et al. [K+92] were not in disagreement with their own Ge K-

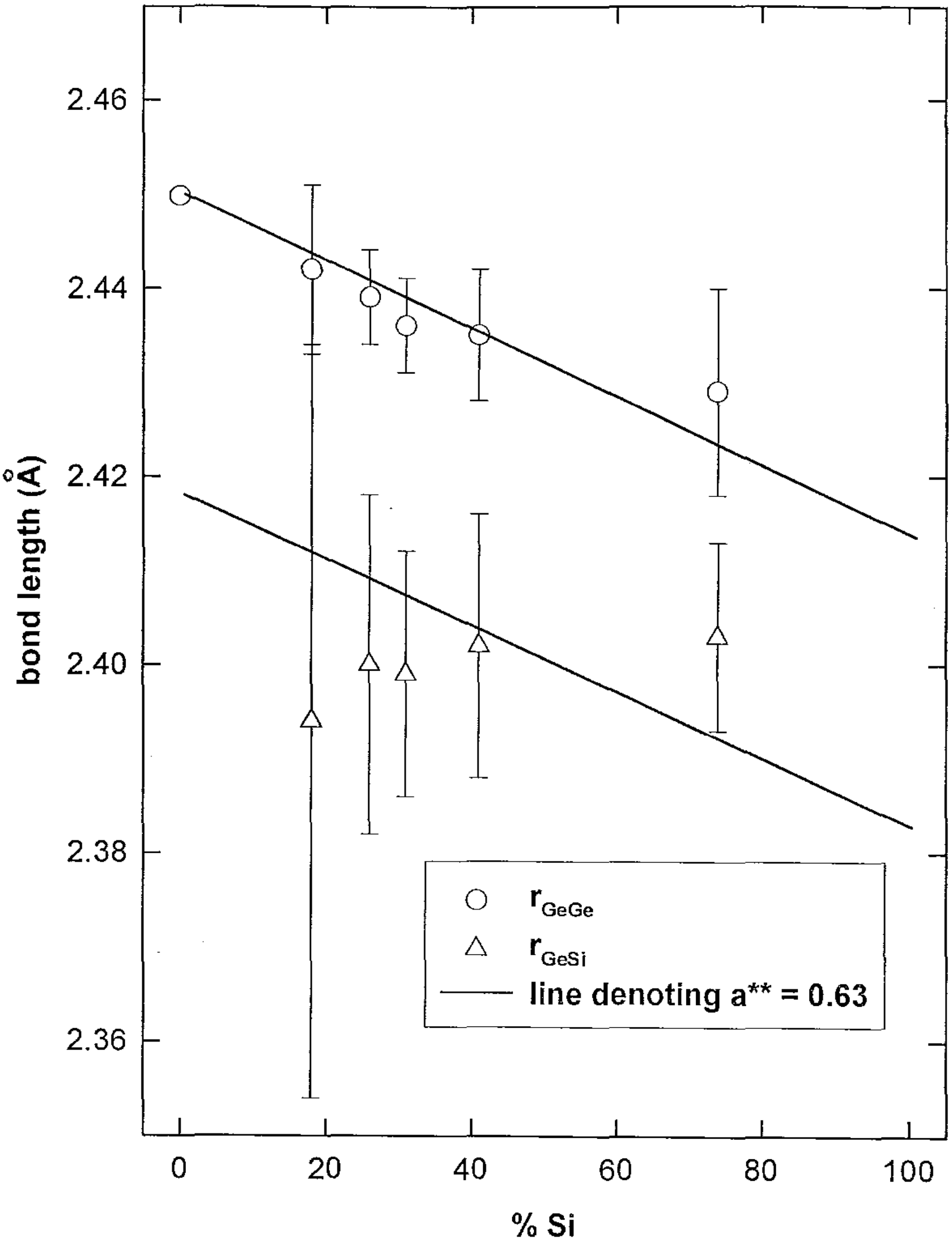

Figure 3.3 - The Ge K-edge EXAFS fitting results of Aldritch et al., indicative of mixed type bonding behavior, described with a**=0.63.

edge results for SiGe relaxed films on Si(100). They arbitrarily assigned uncertainties of ± 0.02 Å for the data of Kajiyama et al., and found that the magnitude of the error bars excluded the possibility of concluding that the bonding was completely Pauling-type. Aldritch et al. admit that the size of the assigned errors is probably too large for some of the points in the results of Kajiyama et al. (especially for the points at high %Ge compositions), and as such, the reconciliation between their conclusions is not necessarily complete.

Aldrich et al. [ANS94] have calculated **a**** from theoretical data of several sources ([CT92, WN92, MZ84]) and found that in general, 0.6<**a****<0.7, suggesting weak Vegard behavior. From their $\mathbf{r_{GeGe}}$ data points (i.e. not using their $\mathbf{r_{GeSi}}$ points, which do not show the expected slope), they have calculated $a^{**} = 0.63^{+0.08}_{-0.13}$ (see Figure 3.3), which agrees somewhat with the calculated results of Mousseau et al. [MT92], and more so with that of others [WN92, GGB91, I+90].

3.3 Proposal

It is this author's opinion that the EXAFS results of Aldritch et al. [ANS94] are not entirely adequate for a firm conclusion concerning the true first shell structure of relaxed, single crystal SiGe alloys to be made. Specifically, the large error bars for the points in Figure 3.3 and the lack of experimental $\mathbf{r_{SiSi}}$ are considered to be limitations. The error bars do not permit an unambiguous conclusion of mixed-type behavior to actually be made. Additionally, the lack of corresponding Si K-edge data does not permit the problem to be fully addressed within the framework of the CT theory [MT93].

This research has attempted to obtain the best quality Si and Ge K-edge EXAFS of SiGe alloys on Si for a selection of samples covering the full compositional range. A simultaneous, multi-edge, multi-spectrum, curve fitting methodology has been used to determine the first shell bond lengths r_{SiSi}, r_{SiGe}, and r_{GeGe} and co-ordination numbers, N_{SiSi}, N_{SiGe}, and N_{GeGe}, for relaxed alloy samples. Additionally, this work has evaluated the improvement in precision obtained by using EXAFS data from both edges in a constrained simultaneous fit. From the bond length results a value for the parameter **a**** has been derived and discussed in the context of the previous results presented in the literature. While strained samples are inherently more interesting, their use presents significant problems (sample thickness, competing epitaxial/compositional strain effects). Thus, as in the work of Aldritch et al. [ANS94], only relaxed (or very nearly so) samples were studied in detail. Nonetheless, in addition to the main portion of this work, for the small selection of strained/relaxed sample pairs available we have performed a preliminary exploration of bond length dependence upon strain. The results of this study are also presented in this work.

4.0 EXPERIMENTAL DETAILS

This chapter covers the experimental aspects of this work. The chapter begins with a short description of sample growth and characterization by x-ray diffraction. The subject then shifts to the synchrotron beamlines where the EXAFS experiments are performed. After a brief description of the EXAFS instrumentation, the experimental details of the present XAFS experiments are described. Finally, the chapter closes with a discussion of an anomalous signal specific to the CSRF-DCM beamline where the Si K-edge data was obtained, which limited the range of SiGe alloy compositions for which useful Si K-edge EXAFS could be obtained.

4.1 Sample Growth and Inventory

The SiGe materials used in this study were produced by Jean-Marc Baribeau at the Institute for Microstructural Sciences (IMS) at the National Research Council (NRC) in Ottawa, Ontario. The samples were grown in a VG Semicon V80 molecular beam epitaxy (MBE) system using solid Si and Ge sources with electron beam evaporators. Base chamber pressure was typically $1\text{-}2*10^{-10}$ mbar, with an order of magnitude increase during growth. Samples were grown on commercial (100) oriented Si and Ge wafers. Ex-situ wafer preparation consisted of 10 minutes in a UV/ozone reactor for hydrocarbon removal, followed by a 10 minute in-situ thermal oxide desorption process at 900°C under a 0.01 nm/s Si flux on the Si wafer (600°C for Ge, no flux). Typical growth temperatures were approximately 500°C, with a 0.2 nm/s flux rate for the Si and

Ge beams. Source fluxes were measured by oscillating quartz crystal monitors.

Sample composition was determined by adjusting the relative Si and Ge fluxes within the MBE system. Afterwards, the composition and strain relaxation was verified by reciprocal lattice mapping of the substrate and alloy $(\overline{2}\overline{2}4)$ peaks using a Phillips Research Diffractometer (PRD), and the accompanying PRD-HRS software. Figure 4.1 depicts a reciprocal lattice map for a SiGe alloy. From the relative peak alignments in reciprocal space, one can determine the amount of retained strain in the samples. In all measurements, strained layers were found to be at least 90% strained, while relaxed layers were found to be at least 75% relaxed. Also, from the difference between the substrate and alloy peak positions, one is able to determine the lattice parameter of the alloy layer. For the samples used in the EXAFS fitting, lattice parameters were extracted from the maps, and were compared to the experimental results of Kasper [K95] in order to extract the true compositions of the samples. The c-Si and c-Ge used in this work were portions of commercially available wafers. Note also that the sample S91s was included in the fitting with the relaxed samples, despite that it is fully strained. At 91% Si on an Si substrate, the epitaxial strain is very slight (hardly detectable in the reciprocal lattice map), and thus, any strain effects on the bond length are negligible.

SiGe alloy samples which were used in the analysis presented in this work are detailed below in Table 4.1. Note that some of the samples were included in the main portion of this work, while others were included in the SiGe NEXAFS project contained in Appendix A. Note also that for the SiGe alloys, a labeling system has been developed for ease of sample identification. The labeling system consists of 4 alphanumeric digits. The first, a letter, refers to the substrate upon which the films is grown. The second, a two digit number, refers to the sample composition. The final, another letter (s,r,a), refers to the strain state (strained, relaxed, annealed).

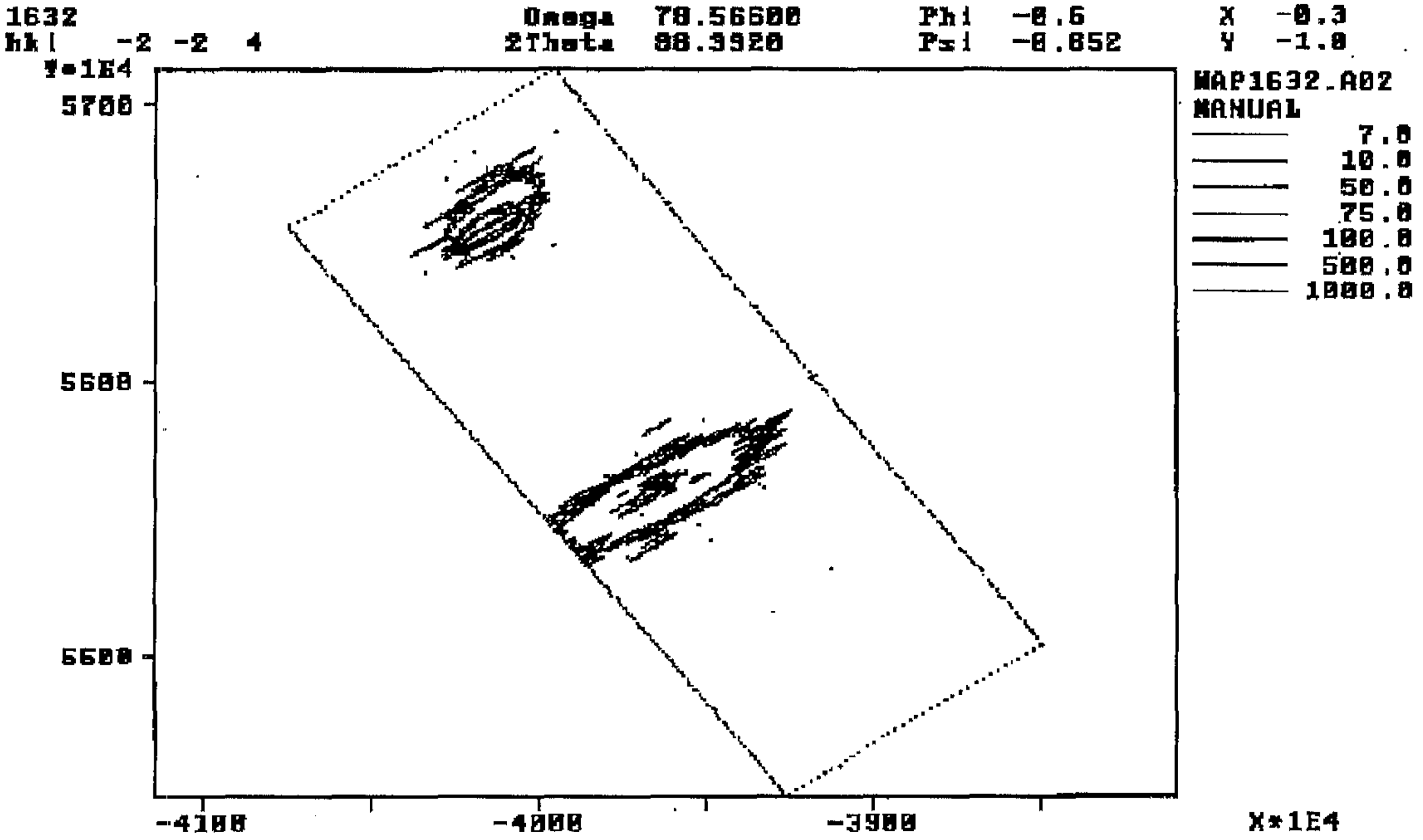

Figure 4.1 - Reciprocal lattice map of a SiGe alloy grown on Si. The narrow topmost peak is the substrate diffraction peak. The broader bottom peak is the peak for the alloy film. Relaxation of the alloy lattice has shifted the alloy peak from the x-axis position of the substrate peak.

Table 4.1: SiGe Sample Inventory

Sample Code	NRC Code	% Si	Substrate	Thickness (nm)	Strain State	Lattice Parameter (A)	Notes
G10r	425	10	Ge	200	relaxed		
G30s	1498	30	Ge	40	strained		
G30a	1498a	30	Ge	40	annealed		annealed at 900C for 30s
G30r	1645	30	Ge	150	relaxed		
G50s	1476	50	Ge	10	strained		
G50a	1476a	50	Ge	10	annealed		annealed at 900C for 30s
G50s2	1646	50	Ge	10	strained		
G70s	1499	70	Ge	2	strained		
G70a	1499a	70	Ge	2	annealed		annealed at 900C for 30s
G90s	1500	90	Ge	1	strained		
G90a	1500a	90	Ge	1	annealed		annealed at 900C for 30s
S25s	1631	25	Si	2	strained		
S29r	1475	29	Si	100	relaxed	5.5909	
S42r	1633	42	Si	250	relaxed	5.5579	
S50s	1473	50	Si	10	strained	5.5411	
S56r	1201	56	Si	300	relaxed	5.5298	
S61r	1632	61	Si	250	relaxed	5.5189	
S71s	927a	71	Si	105	strained		
S75s	1629	75	Si	200	strained		
S76s	1474	76	Si	100	strained	5.4469	
S78r	1478	78	Si	200	relaxed	5.4798	
S80s	930a	80	Si	180	strained		
S91s	1630	91	Si	500	strained	5.4369	

4.2 EXAFS Measurements

4.2.1 Introduction To Synchrotron Radiation

The growth in popularity of XAFS studies directly parallels the growth in availability of synchrotron radiation sources. According to Maxwell's rules, any charged particle undergoing an acceleration must lose energy by emitting electromagnetic radiation. For charged particles moving at relativistic velocities in a closed continuous orbit, this radiation is termed synchrotron radiation. Thus, an electron (or positron) circular accelerator with appropriate fittings (linac injector, beamlines, insertion devices, etc.), termed a synchrotron, is a source of very intense, tunable photon beams.

While XAFS studies are plausible using other x-ray sources (and in fact, XAFS were first discovered using these sources [SSL71]), the measurements are particularly laborious. Synchrotrons offer a wide array of advantages, including a) extremely high intensity (greater than non-synchrotron sources by a factor of 10^5 or more) over a spectrum covering IR to hard x-ray, b) excellent beam collimation (providing high brightness), c) linear polarization with the electric field vector parallel to the ring orbit plane, d) absolute calculability of all source properties, and e) cleanliness of the source [K79].

4.2.2 Experiments At The C2 Station At CHESS

Ge K-edge EXAFS measurements were obtained in the C2 station at the Cornell High Energy Synchrotron Source (CHESS) at Cornell University in Ithaca, New York. The CHESS facility is a parasitic facility to the Cornell Electron Storage Ring (CESR), a dual ring facility, which simultaneously stores both electron and positron current for high energy collision studies. The CESR ring has a diameter of 500 m, and typically operates at an energy of 5.44 GeV with injected currents typically approaching 160 and 120 mA for electrons and positrons, respectively.

The C2 station is a high energy beamline built tangentially to the storage ring, extending from an orbit-bending magnet. The line, which is equipped with a water-cooled double crystal monochromator (DCM), for isolation of the desired photon energy, provides photons spanning an energy range of 3 to 35 keV. The Ge K-edge, at 11.103 keV, is well within this range, ensuring a high flux for measurements. Figure 4.2 is a schematic of the C2 beamline. Si (111) or Si (220) monochromator crystals were used for these measurements.

Due to the high energy of the CESR ring, higher harmonics (for Ge K-edge: 22.2 and 33.3 keV) are a significant problem. In order to avoid their inclusion into the beam, the second crystal in the DCM is typically “de-tuned” from the Bragg angle. Due to their much narrower rocking curves, higher harmonics intensity is reduced by several orders of magnitude, while I_0 intensity reduction is only approximately 50% [C85].

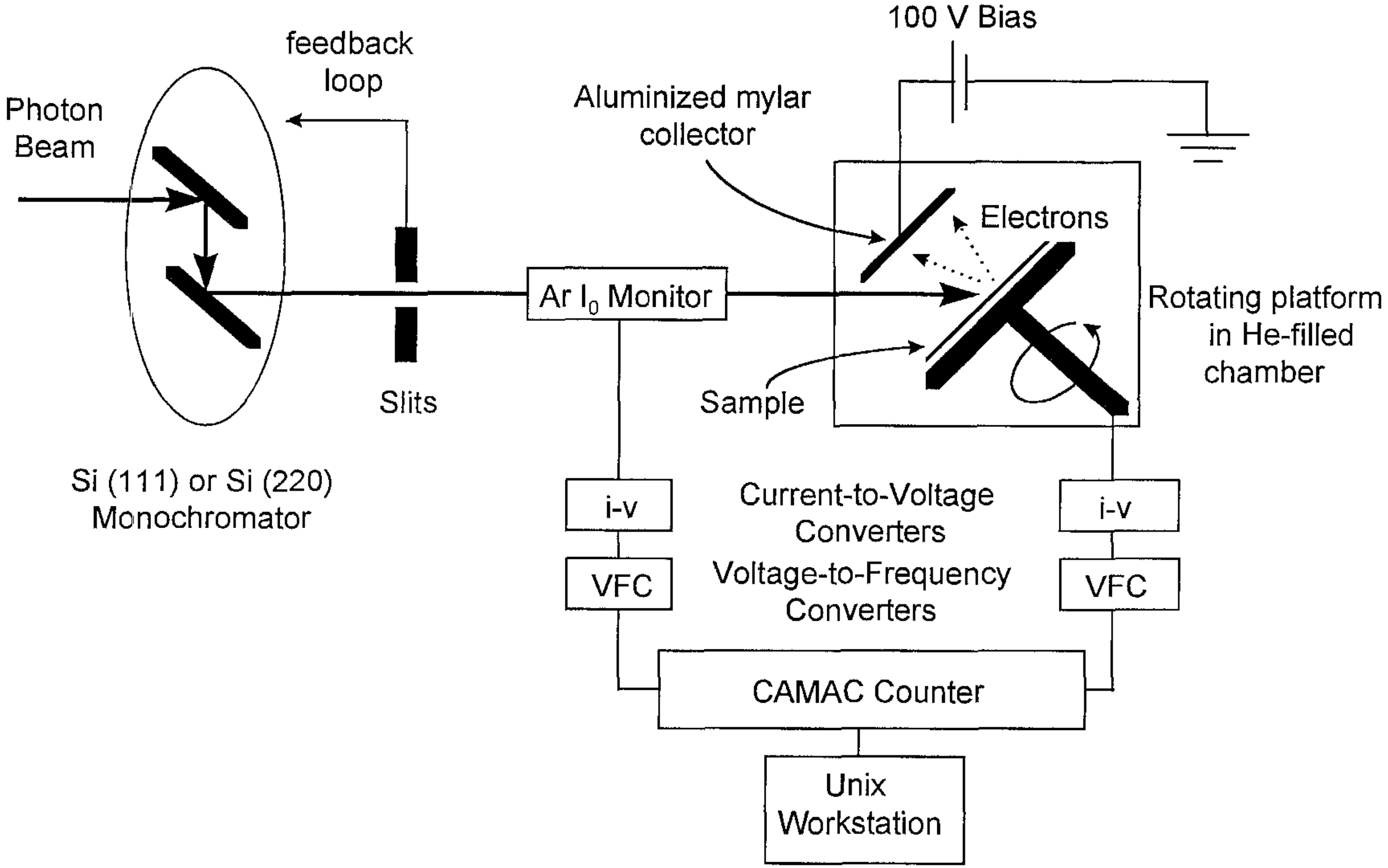

Figure 4.2 - Schematic representation of the C2 end-station at CHESS.

Downstream from the DCM are a set of slits, which are used to control the beam width at the exit port. These slits are critical for the present experiments since it is essential to ensure that the beam strikes only the sample inside the detector apparatus. I_0 measurements are typically made using Ar gas monitors that operate simply by photocurrent detection. The current is converted to a voltage, and then to a frequency, and this serves as the I_0 input into a summing CAMAC counter.

CHESS operation is parasitic to the high energy physics experiments, and thus, dependent upon their operation schedule. Electron injection (termed "fills") are performed every 1-1.5 hours, in order to maximize the time integral of the electron-positron collision luminosity. Frequent filling is convenient, in that photon flux is always high; however, the 1.5 hour cycle is often inconvenient, limiting the available scan time to approximately one half hour.

Many methods of detection are employed in EXAFS measurements. Transmission measurement, the simplest method, is useless in studying thin films, due to substrate absorption. A better method is to detect the absorption decay products: fluorescent photons and photo-/secondary electrons. Fluorescent yield (FY) detection is not a particularly good method to employ for single crystals, since it is strongly affected by Bragg diffraction from the sample. In addition, FY is also complicated by other problems such as absorption saturation effects and poor signal-to-noise ratios due to small acceptance angles and detector saturation.

The best method of detection for semiconductor films is total electron yield (TEY) detection [E+88]. The process involves collecting the photoelectrons and subsequent secondary electrons caused by inelastic scattering. Due to the limited escape depth of secondary electrons (calculated to be less than 1000 Å for Si at the Ge K-edge [E+88]) TEY detection is a surface-sensitive mode that is very well suited for semiconductor thin films. To facilitate detection, a bias is often applied to the sample (relative to the detector), in order to increase the numbers of electrons collected by the detector. Also, a small amount of non-absorbing gas, such as He, in a sealed chamber (or one in which the flow is low) can serve to amplify the TEY signal, serving as a ready source for more secondary electrons.

Figure 4.3 is a schematic diagram of the gas ionization TEY detection apparatus that was used at CHESS. It is composed of a metallic stage upon which the sample is mounted with conductive Ag paint. To this, a 100 V bias relative to the detector is applied. The stage is sealed in a small chamber which is back-filled with ~ 1 atm of He. The photons enter through a non-absorbing mylar window, and strike the sample at ~15° incidence. The electrons are collected with a piece of aluminized mylar, producing a current which is converted to a voltage. This voltage is recorded using a voltage-to-frequency converter and a summing CAMAC counter, which produces the EXAFS data.

During spectral acquisition, the sample was rotated at approximately 100 rpm, in order to smear the numerous diffraction peaks into the background signal, thereby removing their influence from the spectra. Figure 4.4 compares Ge K-edge EXAFS spectra for a piece of Ge-doped InP, one obtained with sample rotation and the other obtained without. Clearly, without rotation, the spectra are nearly useless, since the Bragg peaks are so large and numerous.

Measurements were performed over a range of 1000 eV beyond the absorption edge. Point spacings were typically 1-3 eV/point, with an approximate energy resolution limit of 1 eV. Dwell times during acquisition typically were 2-4 seconds (depending upon the counts), with a 1 sec pause between each point for settling. Energy scale calibration was performed at the Ga, Ge, and As K-edges, with wafer sections of GaAs and Ge.

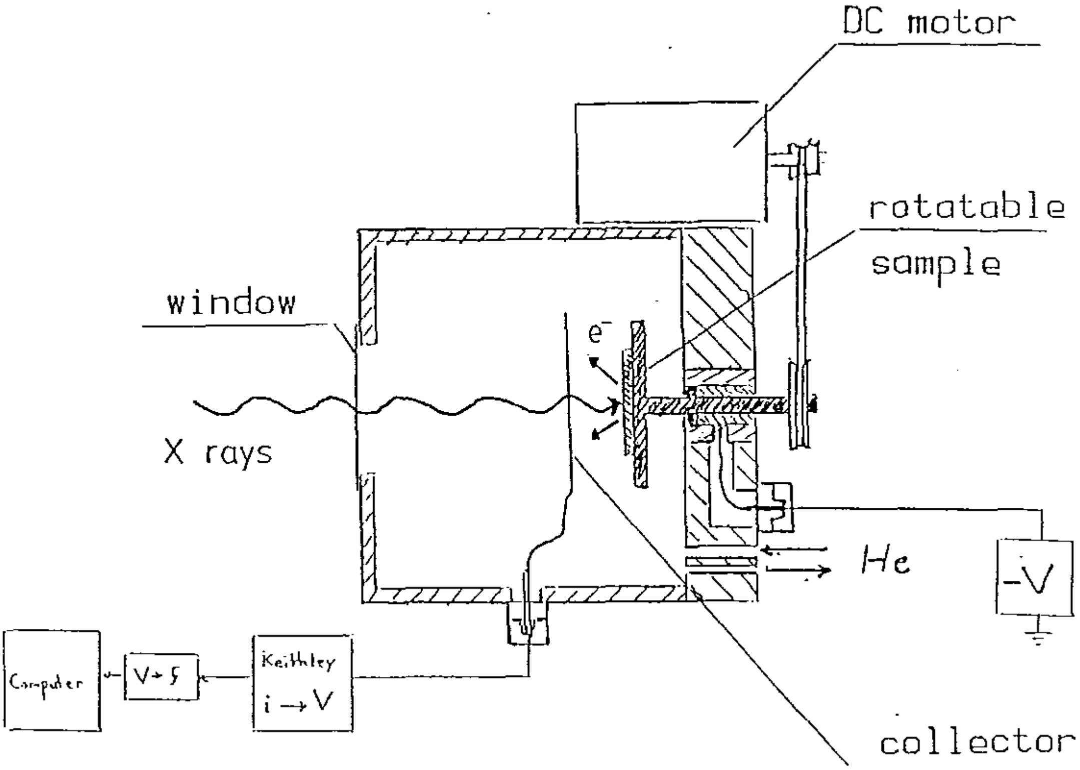

Figure 4.3 - Schematic representation of the detector apparatus used in EXAFS measurements at CHESS.

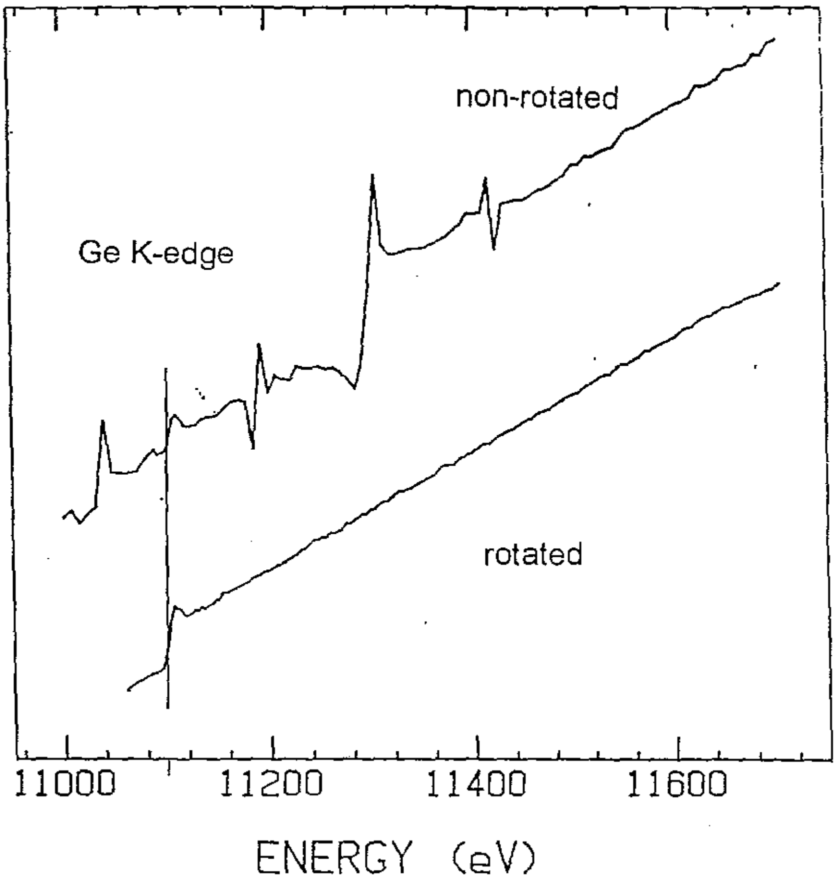

Figure 4.4 - Ge K-edge EXAFS spectra of Ge-doped InP epilayers. Rotation "smears" out the diffraction peaks in the top spectra.

4.2.3 Experiments at the CSRF DCM at SRC

All Si K-edge experiments were performed at the soft x-ray DCM line at the Canadian Synchrotron Radiation Facility (CSRF) at the Synchrotron Radiation Center (SRC) in Stoughton, Wisconsin. The SRC is a dedicated vacuum ultraviolet (VUV)/soft x-ray facility, providing operation at 800 MeV and 1 GeV energies, with a typical injected electron ring current of 200 and 150 mA for the two beam energies, respectively. Most Si K-edge EXAFS were obtained at 1 GeV operation, due to the higher flux (by approximately a factor of 5) available for the relatively high energy Si K-edge. The CSRF-DCM is a soft x-ray line built off a bending magnet. The line offers access to an energy range of 1500 to 3300 eV; however, these relatively low photon energies require that the beam is maintained under high vacuum conditions. Figure 4.5 is a schematic representation of the CSRF-DCM beamline.

The CSRF-DCM line has a DCM monochromator, and InSb (111) crystals were used in the experiments. Down stream from the monochromator are a set of horizontal metallic wire slits used for detection of beam position. Feedback from the slit current was used to control the angle of the second crystal, thereby maintaining beam position relative to the sample. A horizontal Ni-coated focusing mirror after the monochromator is used to reduce the beam size to a small spot (3 mm * 3 mm). I_0 detection is accomplished by use of a N_2 gas cell (0.1 torr pressure), enclosed by 2 Be windows (12.5 μm thickness) which, unfortunately, reduces the incident flux by about 42%. As with the C2 station at CHESS, the induced photocurrent in the N_2 gas cell is converted to a voltage; however, at the CSRF-DCM, this voltage is then converted to a digital signal in an analog-to-digital converter. Multiple inputs at each energy were used to average the signal over a given sampling time.

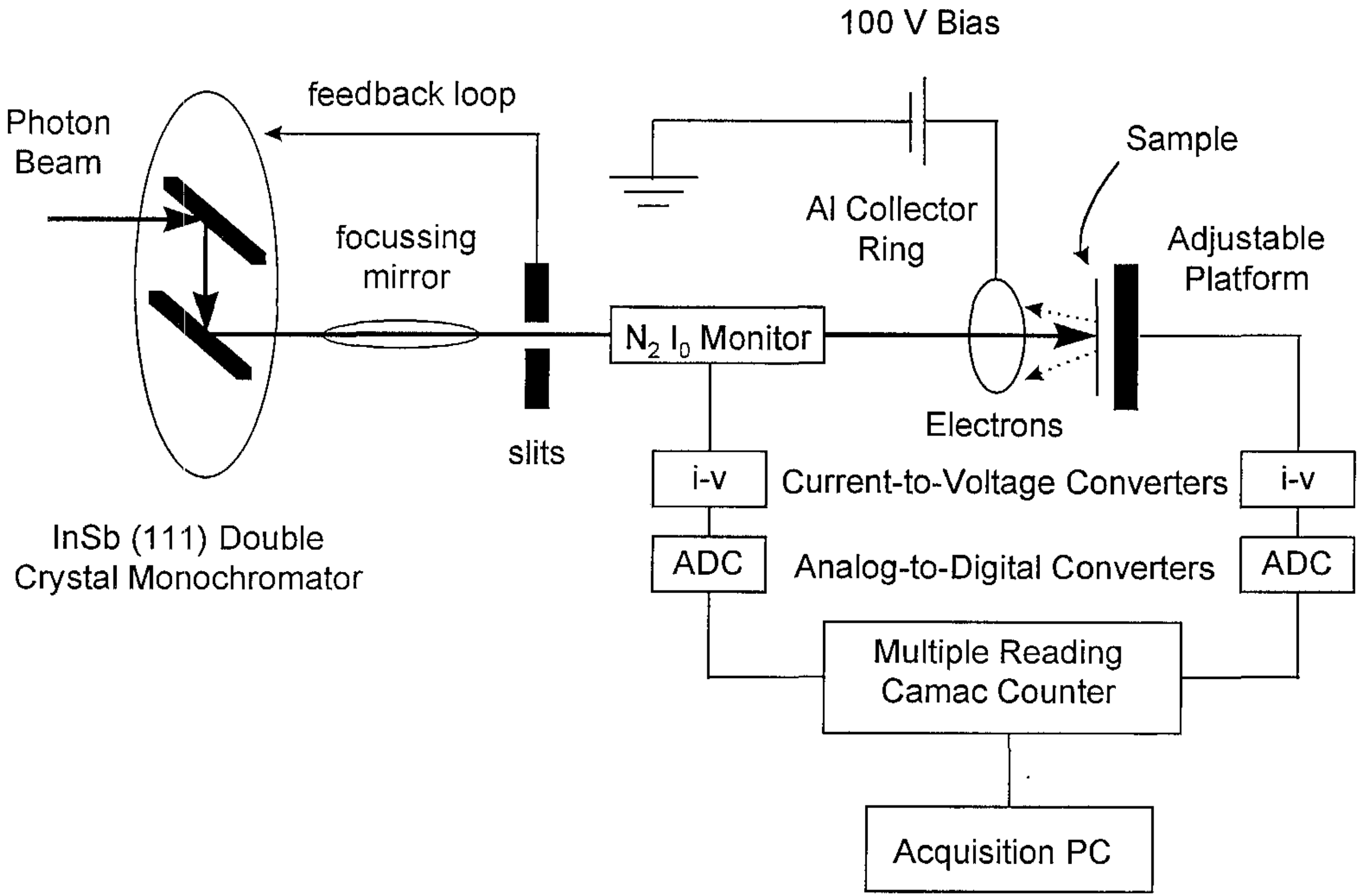

Figure 4.5 - Schematic representation of the CSRF-DCM beamline at SRC.

Just as at CHESS, TEY detection was employed at the CSRF-DCM; however, He amplification was not used. The size of the chamber at the CSRF-DCM creates too long of a path (20cm) for absorption by the He. Additionally, small He pressure fluctuations are difficult to stabilize in the large chamber; hence, noise in the signal becomes a problem. Also, sample rotation was not used for most spectra obtained at SRC, as it is exceedingly difficult to get good operation of the rotation apparatus within the vacuum enclosure. Thus, sample diffraction problems were dealt with by simply manually adjusting the incidence angle until there were no sizable diffraction peaks within the energy range of interest. Measurements were usually performed over a range of 1000 eV beyond the absorption edge. Point spacings were typically 2 points/eV at the low energy end of the spectra, up to approximately 0.33 points/eV at the high energy end of the spectra. Energy resolution was typically 1.0 eV. Dwell times during acquisition typically were 2-4 seconds (depending upon the counts), with a 1 sec pause between sampling for settling of vibrations in the monochromator. Energy scale calibration was performed by measuring the onset of the absorption edge for SF_6 (S K-edge), $CHCl_3$ (Cl K-edge), and Ar. Subsequent corrections were made to the energy scale of the Si K-edge data (the error amounted to 23 eV at 3189 eV). Calibrated spectra for c-Si were compared with FEFF theoretical results (the program is detailed below, in Chapter 5), and found to be in good agreement.

Many Si-based materials oxidize very quickly when exposed to oxygen, and the SiGe alloys used in this study are no exception. Because TEY detection is so surface-sensitive, it is important to ensure that the sample surface represents the bulk environment as closely as possible. Thus, prior to all Si K-edge measurements, the samples were etched in 10% HF in water solution, in order to remove any surface oxide. Etching in this manner leaves an oxide-free, hydrogen terminated surface that is stable in air for several minutes, at least. This provides ample opportunity to load the sample into the vacuum chamber at the beamline end station, where it will be well protected from oxidation. Note that for Ge K-edge measurements at CHESS, HF etching is not necessary, since TEY samples much more deeply at the higher beam energy (11 keV). The change in the work function of the sample surface (induced by the oxide layer) is not a problem, since the He-amplification samples mostly high energy electrons, rather than low energy electrons which would have trouble escaping an oxide barrier.

4.2.4 The I_0 Oscillation at SRC

It became apparent in January 1996 that the Si K-edge results at SRC were contaminated by a spurious signal. Figure 4.6 depicts the Si K-edge EXAFS data for a dilute (25%) alloy, along with the analogous Ge K-edge EXAFS amplitude envelope **(A(k))** for comparison. One does not expect the Ge and Si K-edge amplitude envelopes to be identical; however, one expects that they should be very similar, since the backscatterers are about the same. Clearly, the beat in the Si K-edge data at 9 $Å^{-1}$ differs significantly from what is seen in the Ge K-edge amplitude envelope. Figure 4.7 shows the variation in "beat" magnitude as a function of composition. In each case, the Ge K-edge compliment does not show the same feature. In addition, the signal was present in solid and gaseous samples, which ruled out any possible diffraction effects.

It became clear that the signal is instrumental in nature. As a test, a piece of standard crystalline Ge wafer was placed in the experimental chamber, and a Si K-edge EXAFS run was performed. Figure 4.8 depicts the results. Spectrum a) is that of the I_0, which is free of any obvious oscillating signal (note that the large blip at 2050 eV is due to a monochromator glitch). Spectrum b) is the corresponding TEY signal. Again, there is no visible signal oscillation here. Finally, spectrum c) depicts the resulting TEY/I_0 ratio, magnified and background subtracted for presentation clarity. The result,

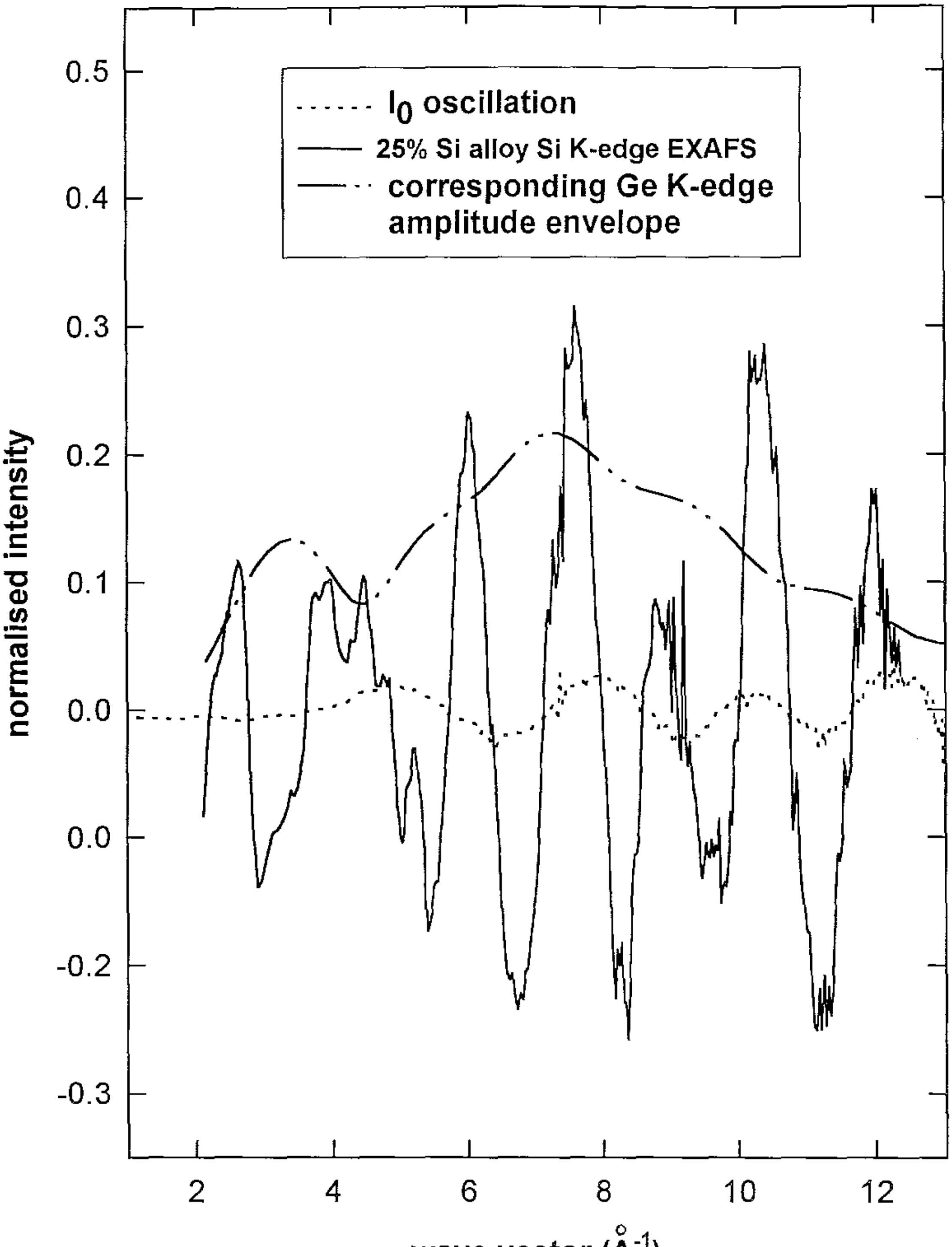

Figure 4.6 - The E-space oscillation superimposed upon the Si K-edge EXAFS data of a dilute alloy, along with the Ge K-edge EXAFS amplitude envelope for the same alloy. Clearly, the E-space signal is strongly contaminating the alloy Si K-ede EXAFS data.

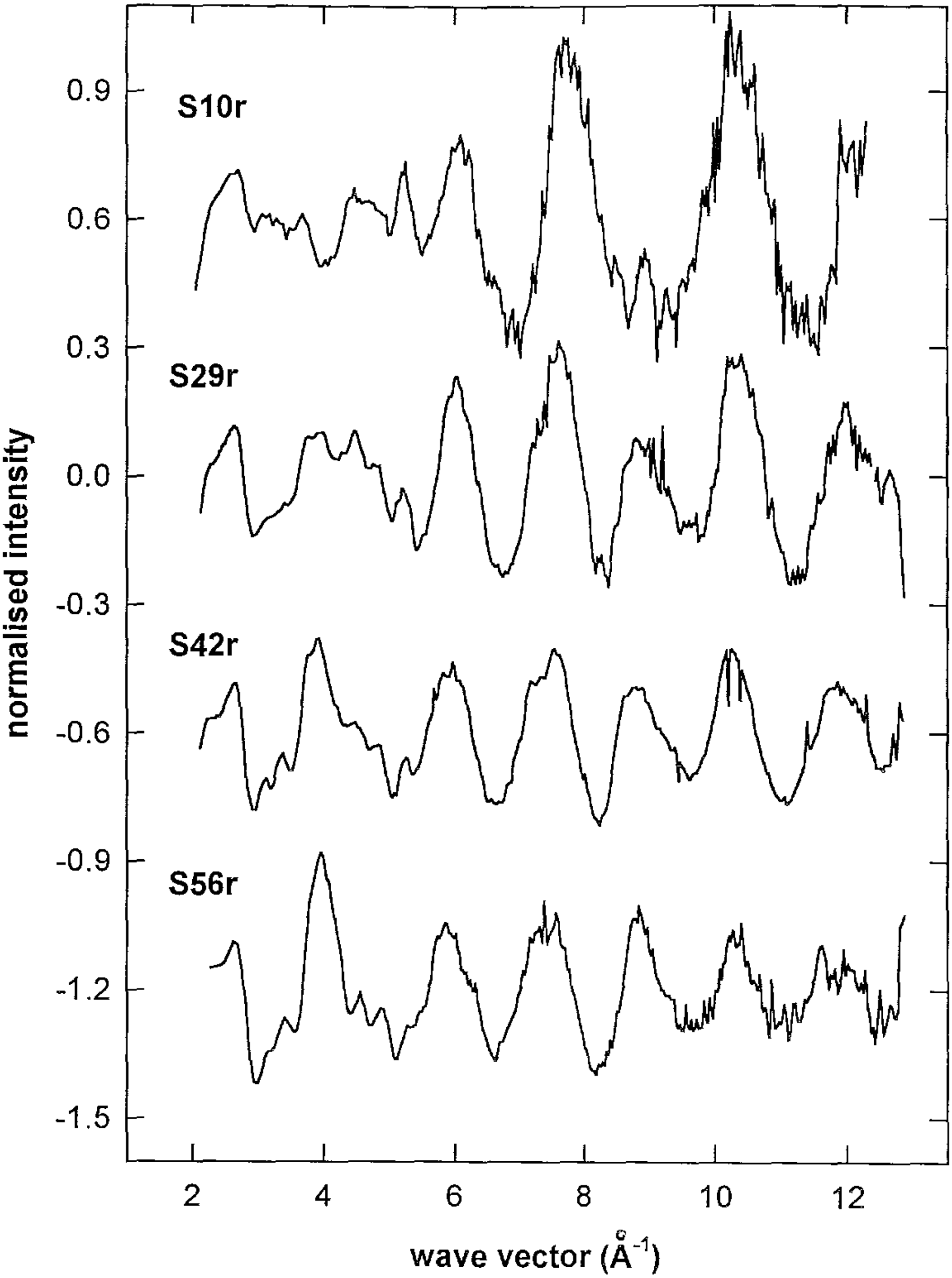

Figure 4.7 - Beat magnitude as a function of alloy composition. The remarkable trend is a result of the decreasing strength of the I_0 oscillation with respect to the signal of the absorbing Si atoms.

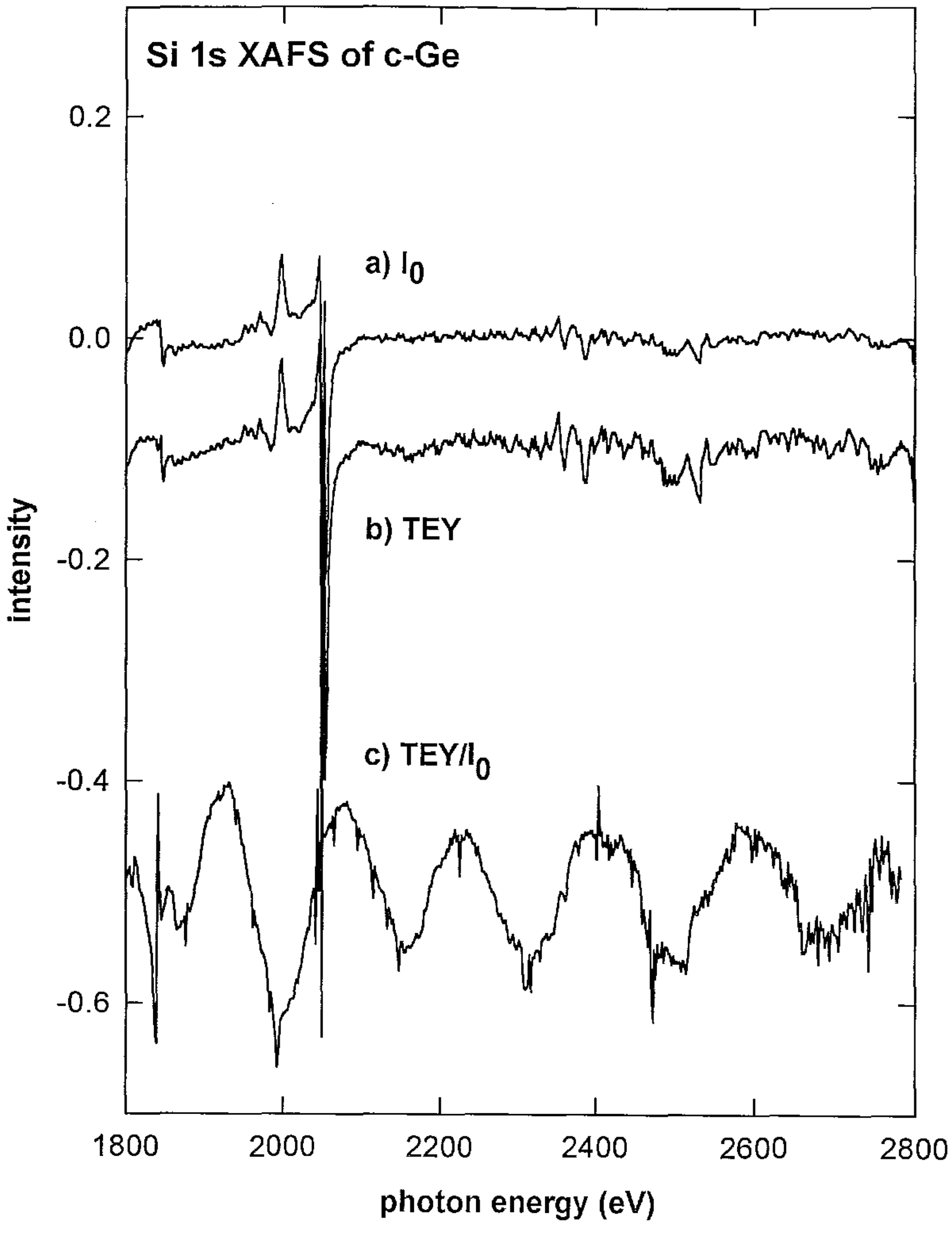

Figure 4.8 - Si K-edge spectra of crystalline Ge: a) and b) are the I_0 an TEY signal, free of oscillations, and c) is the TEY/I_0 ratio. Note that the large glitch in the I_0 signal is due to a diffraction effect in the monochromator. Also, there is a weak Si absorption in the ratio signal at 1839 eV, due to some weak Si surface contamination.

an energy space oscillation, is the spurious signal that was confounding the analysis. Note that the signal cannot be due to Si contamination of the Ge wafer. While there is a small Si K-edge edge jump in the ratio spectrum, the oscillation is far too large in comparison to Si EXAFS and is periodic in energy space as opposed to k-space, with a period of approximately 200 eV. The signal is plotted in k-space in Figure 4.6, and here its insidious effects on the experiment become most evident. This signal is the source of the anomalous beating in the Si K-edge EXAFS.

The source of the signal is still not clear; however, recently, a publication by Oyanagi et al. [OHK96] has provided new insights. In their publication, the authors demonstrate various methods of controlling the second crystal in a DCM. What was found was that simultaneous control of the x and y plane of the 2nd crystal produced oscillations in the I_0 and the resulting Ge K-edge EXAFS spectra of an extremely dilute SiGe alloy. The period of their oscillations approximately match the period of the oscillation present at the SRC. Controlling the y plane alone, or leaving both uncontrolled, resulted in featureless I_0 signals. Oyanagi et al. attribute the oscillations in the x- and y- controlled mode to possible variations in higher harmonics in the I_0. In the case of the Si K-edge work at SRC, this cannot be the case, since the ring energy is too low for considerable higher harmonic generation. Nonetheless, the energy space oscillations are very probably the same, and it is reasonable to conclude that the signal is an artifact, and not part of the Si K-edge signal. Recent communications with the CSRF-DCM personnel indicate that there is a vibrational problem in the second crystal of the monochromator, and this may be the source of the problem.

The most attractive option for dealing with the energy space oscillation shown in Figure 4.6 was to obtain new Si K-edge data at a different beamline. Unfortunately, EXAFS beamlines in the Si K-edge energy range are few and far between. An attempt was made in April 1996 to use the X24A beamline at the National Synchrotron Light

Source (NSLS) at Brookhaven National Laboratory (BNL) in Upton, New York; however, the beamline proved to be inadequate for such experiments, and there was no time to make improvements. The second option was to simply use the I_0 signal from crystalline Ge to "clean" the contaminated spectra. While this is generally undesirable (as it adds subjective processing steps), an attempt was made nonetheless. Figure 4.9 depicts the cleaned $\chi(\mathbf{k})$ spectra for three samples. One would expect a generally smooth amplitude envelope for the true EXAFS spectra, and hence, the cleaned spectra, showing no "beating" signal at 9 Å^{-1}. Unfortunately, the "cleaning" proved to be inadequate for the more dilute samples, often leaving invisible distortions, and not fully removing the I_0 signal. In Figure 4.9, the bottom two spectra, at 29 and 42% Si, seem to be acceptable; however, subsequent fitting indicated that these spectra were still highly distorted. Thus, the final option available was chosen: no data for compositions below 56% Si was used. The spectra for the 56% Si samples were not "cleaned", since at this composition, the I_0 signal is weak, and most of it is removed in the background subtraction. Nonetheless, the energy space oscillation represents a significant source of error for the dilute Si K-edge data.

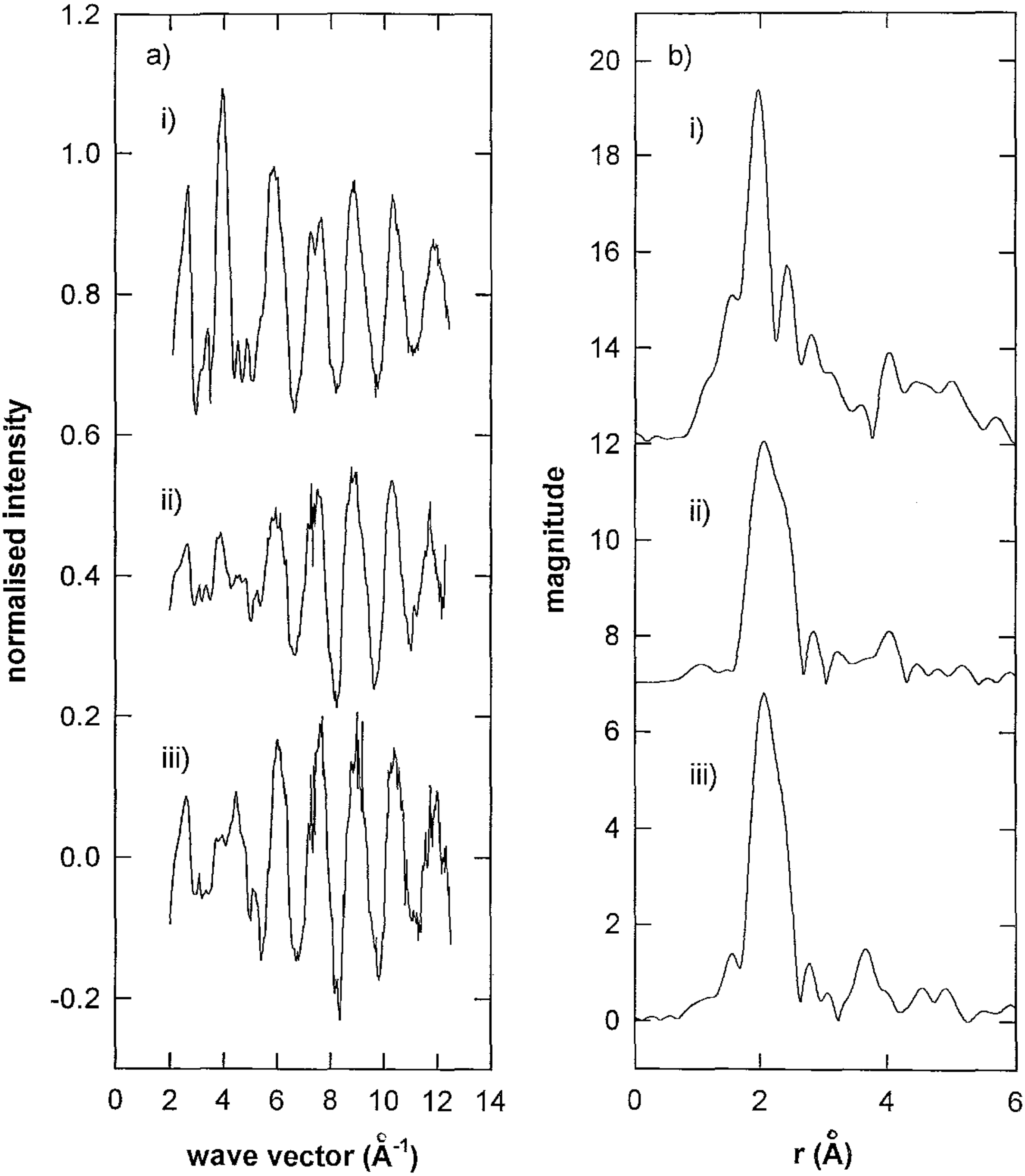

Figure 4.9 - Attempts at cleaning "contaminated" data. Panel a) depicts the cleaned chi(k) data, while panel b) depicts the resulting FT. The spectra are from alloys i) S56r, ii) S42r, and iii) S29r.

5.0 DATA ANALYSIS

In this chapter, the detailed analysis procedures are presented, including an example of step-by-step processing of data for a SiGe alloy. Included with this is a short description of the processing software. This is followed by a detailed discussion of the fitting procedure, including fitting models and the simultaneous multi-edge multi-spectra fitting using the MFIT program. The chapter concludes with a discussion of the error analysis methodology.

5.1 Regular Processing Details

EXAFS data analysis is not a routine procedure. Long before one can do any curve fitting, proper data processing techniques must be developed. Without these, the results obtained from fitting will be unreliable. The process described in Chapter 2 for crystalline germanium does not adequately communicate the intricacy of the process. In most cases (and certainly in the case of SiGe alloys), the data is far more complex than the relatively "clean" data of crystalline Ge; consequently, processing decisions become significantly less clear. To illustrate this, a detailed procedure for analysis of an alloy Si K-edge spectrum is described below.

The first step in the process is a pre-edge background subtraction. In many cases, pre-edge data is not linear, due to many sources, such as inelastic Compton scattering, impurity absorption, instrumental effects, and other processes. This is largely a cosmetic issue and in most cases, either linear backgrounds are removed, or nothing at all is done, since the spline procedure used to remove the background signal will also take into account most effects from non-linearities in the pre-edge signal.

The next step is "glitch" removal. "Glitch" refer to artifacts in the spectra such as diffraction effects from single crystal samples, instrumentation irregularities, etc. Often during spectral acquisition, artifacts are unavoidable (especially diffraction glitches with single crystals at SRC). Figure 5.1 presents an assortment of common glitches that appear in EXAFS experiments. Spectrum a) depicts a rather large step in k-space data. It is very easy to overlook such a glitch in the raw data (especially when they are even smaller!), since it often can be mistaken for noise or dropped points (a result of electronics problems). Without removal, a step glitch such as this will distort the background subtraction, and ultimately, the isolated EXAFS signal. Spectrum b) depicts a monochromator glitch from a spectrum obtained at the CSRF-DCM. At the photon energy corresponding to this monochromator angle, higher harmonic diffraction is greatly intensified. As a result, the normalization procedure produces a distorted signal for this specific energy, which appears as the monochromator glitch in the spectrum. It presents little problem in the analysis (it is often indistinguishable from noise), and is left untreated in this work. Spectrum c) depicts a sample diffraction glitch in Si K-edge XAFS data. Clearly, the effects of the glitch are large, introducing a step into the data, and severely distorting a long (50 eV) portion of the spectrum.

If the glitches are sizable (i.e. on the same order as the XAFS) and unavoidable by instrumental means, they must be removed. The simplest method is to delete the glitch region of the data (a useful method for getting around monochromator induced glitches when necessary); however, this leaves a portion of the spectrum without corresponding data points. One may attempt to interpolate this region, though this is usually undesirable. Worse still are steps in the background signal of the data, which also must be removed, usually by piece-wise removal of linear backgrounds. To

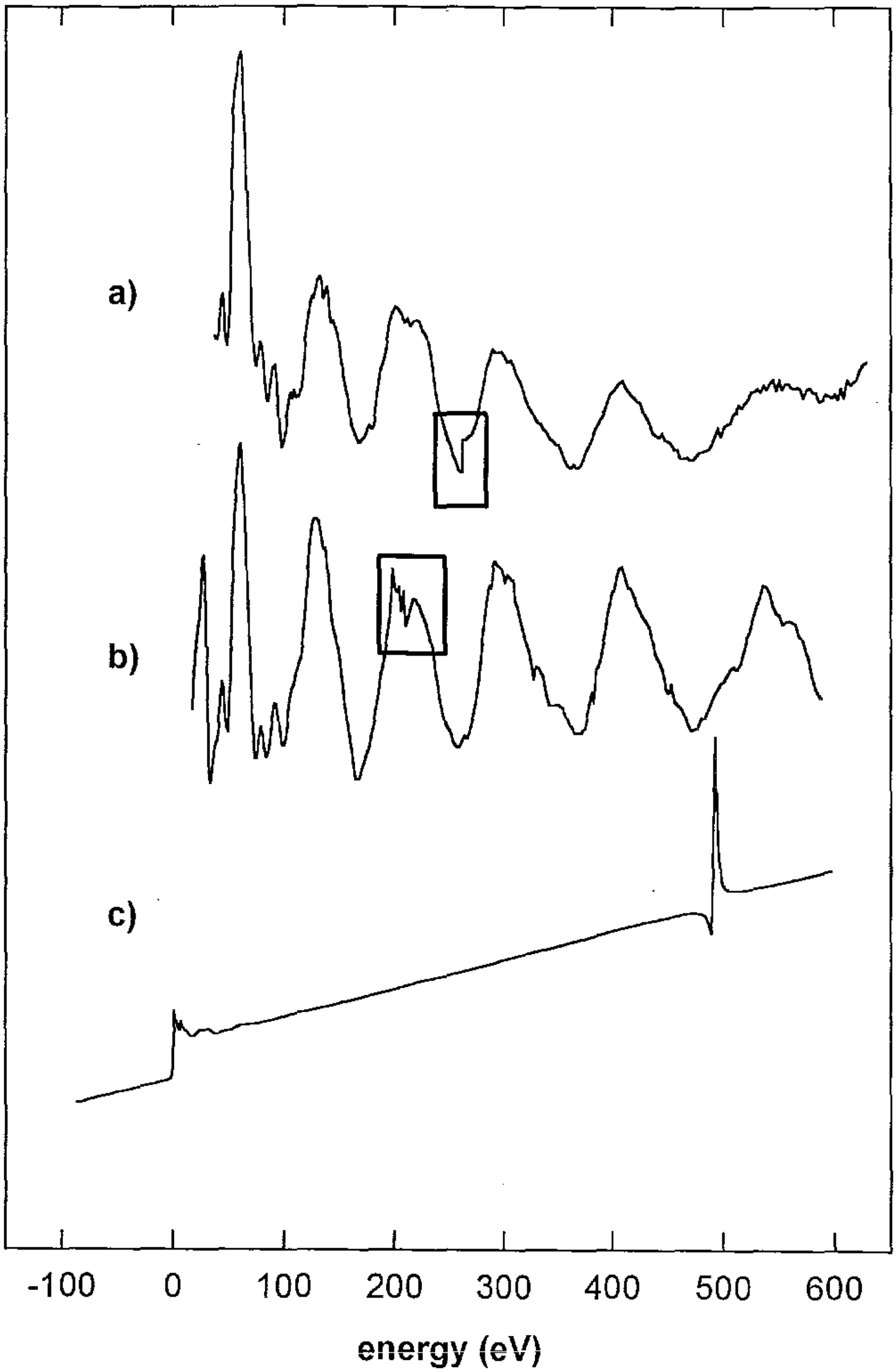

Figure 5.1 - Gallery of glitches: a) step glitch, b) monochromator glitch, and c) sample diffraction glitch.

remove diffraction glitches, one may "cut-and-paste" spectra together, but this is arduous and mostly undesirable, since it tends to introduce distortions. The best way to minimize the effects of diffraction glitches is to: a) rapidly change the angle of the sample with respect to the incident x-ray beam, as is described in Chapter 4 for Ge K-edge EXAFS experiments at CHESS, or b) adjust the angle such that the diffraction glitch is shifted outside the energy range of interest, as is described in Chapter 4 for Si K-edge EXAFS experiments at CSRF-DCM.

The next critical processing issue is the separation of the NEXAFS from the EXAFS. The choice of where to truncate involves three competing interests: 1) the desire to minimize the influence of multiple scattering contamination in the EXAFS, 2) the desire to extend the k-range of the data to low k (especially important for low Z backscatterers, such as Si, where most of the backscattering amplitude lies), and 3) the need to properly align the background subtraction at the low k end of the data. Figure 2.1 (inset) depicts the choice for Si K-edge data of c-Si. In this case, 19 eV past the edge was found to be the best choice for Si K-edge EXAFS data after many iterations of fitting. In general, the choice is not obvious, and the best choice can only be made with experience in data analysis.

Background subtraction, the next step in the analysis, is probably the most critical. Equation 2.4 requires that the atomic absorption component, $\mu_0(k)$, is removed from the data; however, one can never obtain $\mu_0(k)$ experimentally ($\mu_0(k)$ is the atomic absorption for an isolated atom within the same environment, i.e. EXAFS without backscattering, but within the same backscattering environment). Thus, one must make approximations to $\mu_0(k)$. Many different software packages for this exist; however, they all share the same basic fundamental process, which is to subtract background-approximating curves from the data, in either energy- or k-space. The usual method involves subtraction of multi-sectioned splines, which are multi-sectioned polynomial functions (usually cubic) whose first derivatives are continuous at the nodes. The number of spline sections required is dictated by the experimental spectra - longer spectra, or spectra with extremely convoluted background shapes require more sections and/or higher order polynomials.

The choices in background subtraction are very important; too flexible splines will selectively rob the EXAFS oscillations of their intensity, while too inflexible splines will not adequately remove the background. The results of improper background subtraction becomes readily visible in the $\mathbf{F_n(r)}$. Figures 5.2a-c depict examples of background subtractions for Si K-edge data of a SiGe alloy. In this example, the choice of optimum background is complicated by a very complex background shape, as well as the need to include significant low-k information. Too much background subtraction (case i) introduces tremendous distortions in the low r region of the $\mathbf{F_n(r)}$, and often results in signal depletion in the first shell. Inadequate subtraction (case iii) leaves powerful low frequency (<1.0 Å) signals that leak into the first shell signal. In general, one seeks to have smooth, featureless backgrounds that do not show any sort of oscillation (the correct background, case ii); however, this can often be complicated by multiple scattering signals at low-k, and complex background shapes (either instrumentally induced, or a result of multi-electron processes) [LBB94].

After background subtraction, the data must be normalized by $\mathbf{\mu_0(k)}$. Typically, one uses the magnitude of the edge jump, along with a correction for differing pre- and post-edge slope differences as the normalization factor. Figure 5.2b depicts the isolated EXAFS data for Figure 5.2a after background subtraction and normalization.

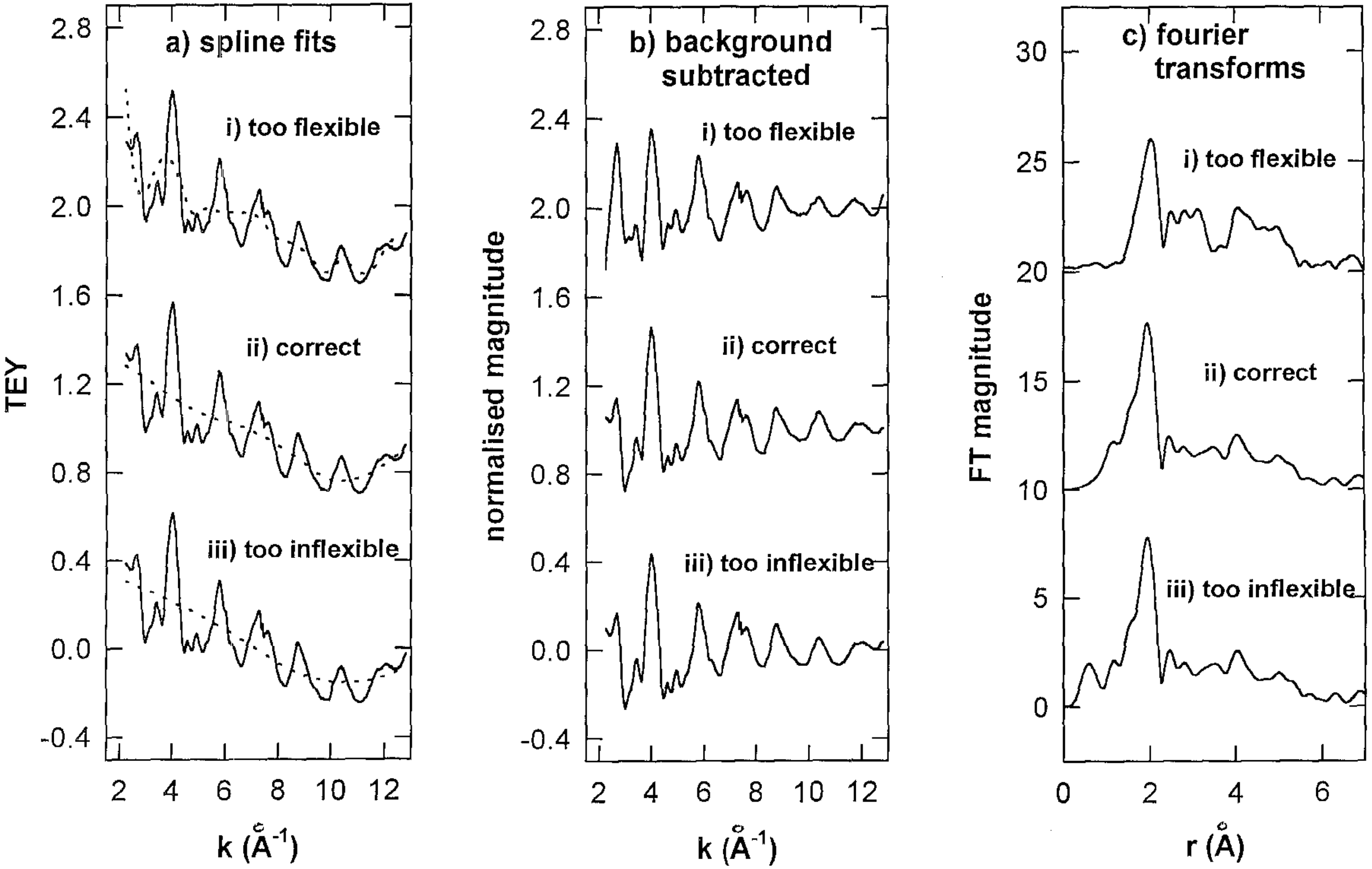

Figure 5.2 - Panel a) depicts three possible background choices (i-iii) for the isolated EXAFS of a 75% Si alloy. Panel b) depicts the results of the background subtractions, while panel c) depicts the resulting Fourier Transforms.

At some point in the analysis, the choice of k-weighting (i.e. the choice of the exponent n for the $-1/k^n$ term in the EXAFS equation) must be made. Previously, the convention was **k** weighting should be dependent upon the atomic number of the backscattering atoms, i.e. **k** weightings of 1, 2, and 3 for backscatterers with approximately Z>57, 36<Z<57, and Z<36, respectively [SSL75]. In this fashion, the **Z** dependence of the element-specific backscattering $\mathbf{f(\pi,k)}$ was reduced, forcing the amplitude envelopes to be more Gaussian-shaped. This involved a trade-off, in that higher **k** weighting tends to emphasize higher energy data where signal to noise ratio is poorer. Current thinking on this issue has reversed, preferring the use of lower **k** weighting (i.e. 0 or 1), due to a need to include much of the lower k data for proper analysis, and leave the amplitude envelope undistorted [R+91]. For SiGe alloys, $\mathbf{k}^1$ weighting is probably best, since Si is a low **Z** element, and thus most of its backscattering signal is at low **k**. $\mathbf{k}^0$ weighting is not particularly desirable, since it tends to broaden the peaks in the $\mathbf{F_n(r)}$, such that Fourier filtering is hindered.

Discrete Fourier transformations introduce a variety of distortions into the data, of which, data termination effects are probably the most important to be considered. The finite nature of the data set results in the addition of weak signals extending throughout the range of the resulting Fourier transform. These signals, termed ringing, are much like thickness fringes in diffraction, being necessary for adequate accounting of the abruptness of the data (the shape of the envelope of the $\chi\mathbf{(k)}$ data). Ringing signals pose significant problems in higher shell analysis, where the physically significant, but weak higher shell signals can be confounded by the artificially added ringing signal. For first shell analysis, ringing is less of a problem, though it can introduce minor distortions that becomes evident in subsequent fitting. Ringing strength is inversely related to k-space data length; hence, it is always desirable to maximize the length of experimental spectra. In addition, the use of apodizing window functions in transforms can reduce ringing effects, at the expense of some additional peak broadening. More of a problem for first shell analysis is peak broadening, another data termination effect. The peak resolution in the $\mathbf{F_n(r)}$ is inversely related to the data k-range, and for shorter k-range data (such as the Si K-edge data, relative to the Ge K-edge data), the peaks in the $\mathbf{F_n(r)}$ are broadened. Again, this is impetus to extend the usable data range.

At this point, it would be easy to conclude that EXAFS data analysis is more art than science. In order to guard against this artistic component, processing must be done systematically, ensuring that in any comparison, each spectrum is processed identically. In doing this, distortions introduced by processing will be as similar as possible from spectra to spectra, and incorrect interpretations can be avoided. For these reasons, this author has made use of an automated processing program, entitled Bandit, written by T. Tyliszczak. The program requires a macro (Figure 5.3) to be supplied which contains the names of the data files, along with the user's pre-set specifications for processing the data. Using these specifications, the program performs the following functions (processing parameters are indicated in parentheses):

a) reads in the energy-space data
b) strips away the near-edge information and truncates at the high energy end (using the $\mathbf{E_{min}}$ and $\mathbf{E_{max}}$ cutoffs),
c) calibrates the edge position (at the edge-jump fraction, 0.0-1.0),
d) background subtracts splines (using the polynomial order and number of sections),
e) converts to k-space (using the $\mathbf{k_{min}}$ and $\mathbf{k_{max}}$ cutoffs),
f) Fourier transforms to r-space, and

```
09 ;# of files
 File names
g1475x.1
g1633x.1
g1201x1.1
g1632x.1
g1478x.1
g1474x.1
g1473x1.1
gbw1x.1
g1630x.1
 limits for edge determination
    10.00       100.0       500.0      ;below edge; min above; max  above
    .5000       .0000    ;edge calibration y-position (0.-1.), energy shift
    17.00       1000.    ;truncation limits in energy space
    2.000       16.00    ;truncation limits in k space
 k-weighting:1,kind of spline:3,# of sections:3,alpha(backg.corr):0
    0.400       3.000    ;filter limits
 filter type:S,filter factor 0-1:    .30
 file format (bin,ascii,non):A,stop for deglitching:N,start from FT:N,print:N
 xcol:0 ycol:0 ycol_a:0 ycol_b:0 log:N
                                              stop at final display:Y
```

Figure 5.3 - Sample of a user-inputted macro file for the Bandit Program

g) Fourier filters to q-space (using the window ranges, types, and sill steepness factor). Thus, the output of the program, the $\chi(k)$, $F_n(r)$, and $\widetilde{\chi}(q)$ spectra, have all been processed in an identical manner, using the same specifications, thereby minimizing any effects of processing distortions.

In this work, all spectra were processed using the Bandit software. Figures 5.4a-c and 5.5a-c depict the $\chi(k)$, $F_n(r)$, and $\widetilde{\chi}(q)$ spectra for the Si and Ge K-edge data of the SiGe alloys as well as crystalline Si and Ge. The edge position was calibrated to the midway point of the edge jump. Data truncation for Ge K-edge data was at 15 eV beyond the edge jump, out to 1000 eV beyond the edge jump (signal-to-noise limited). For Si K-edge data, truncation was at 19 eV beyond the edge jump, out to 630 eV (monochromator glitch limited). The truncated spectra were then normalized to the height of the edge jump. In both cases (Si and Ge K-edge spectra), a three section cubic spline was subtracted from the energy space data, in order to remove the background. While this may seem too inflexible for the length of the Ge K-edge data, it has proven to be sufficient, given the relatively smooth backgrounds. Transformation to k-space was then performed, using k^1 weighting. Finally, the k-space data below 2 $Å^{-1}$ was truncated, yielding k-ranges of 2-16 $Å^{-1}$ for Ge K-edge data, and 2-12.8 $Å^{-1}$ for Si K-edge data. Fourier transformation was performed using a zero-filling window. Filtering was performed over the first shell peak in the $F_n(r)$ (ranges 0.4 - 3.0 Å), using a symmetric Hanning window with a steepness factor of 0.300, and r_{min} and r_{max} values of 0.40 and 3.0 Å. The Fourier filtered q-space data were the input for subsequent fitting. The above procedure is summarized below in Table 5.1, which lists some of the important Bandit input parameters:

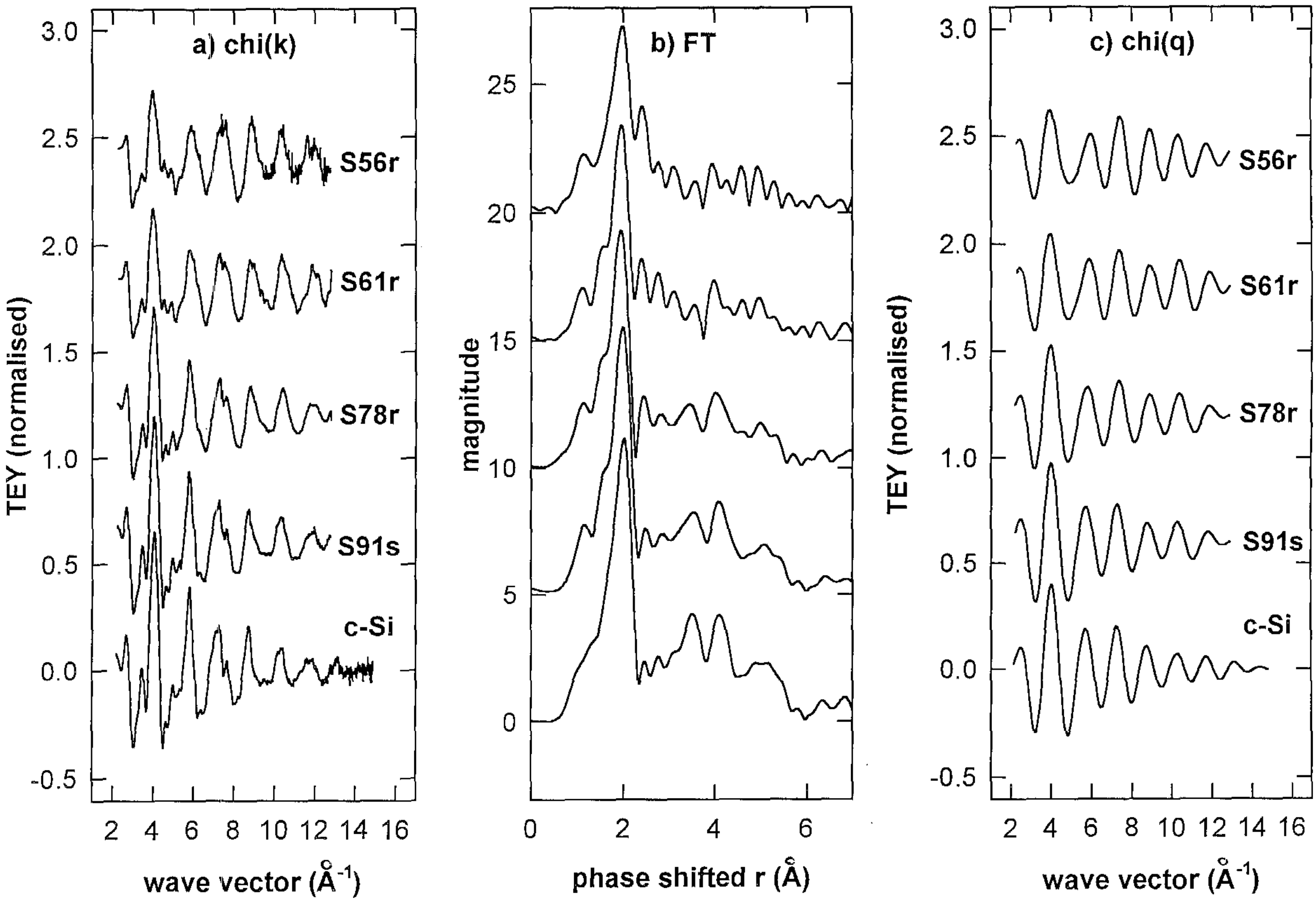

Figure 5.4 - Si K-edge spectra: a) chi(k) spectra, b) Fourier transforms of a), and c) first shell Fourier filtered spectra obtained from b). Note the transition from Ge- to Si-dominated backscattering as the %Si increases.

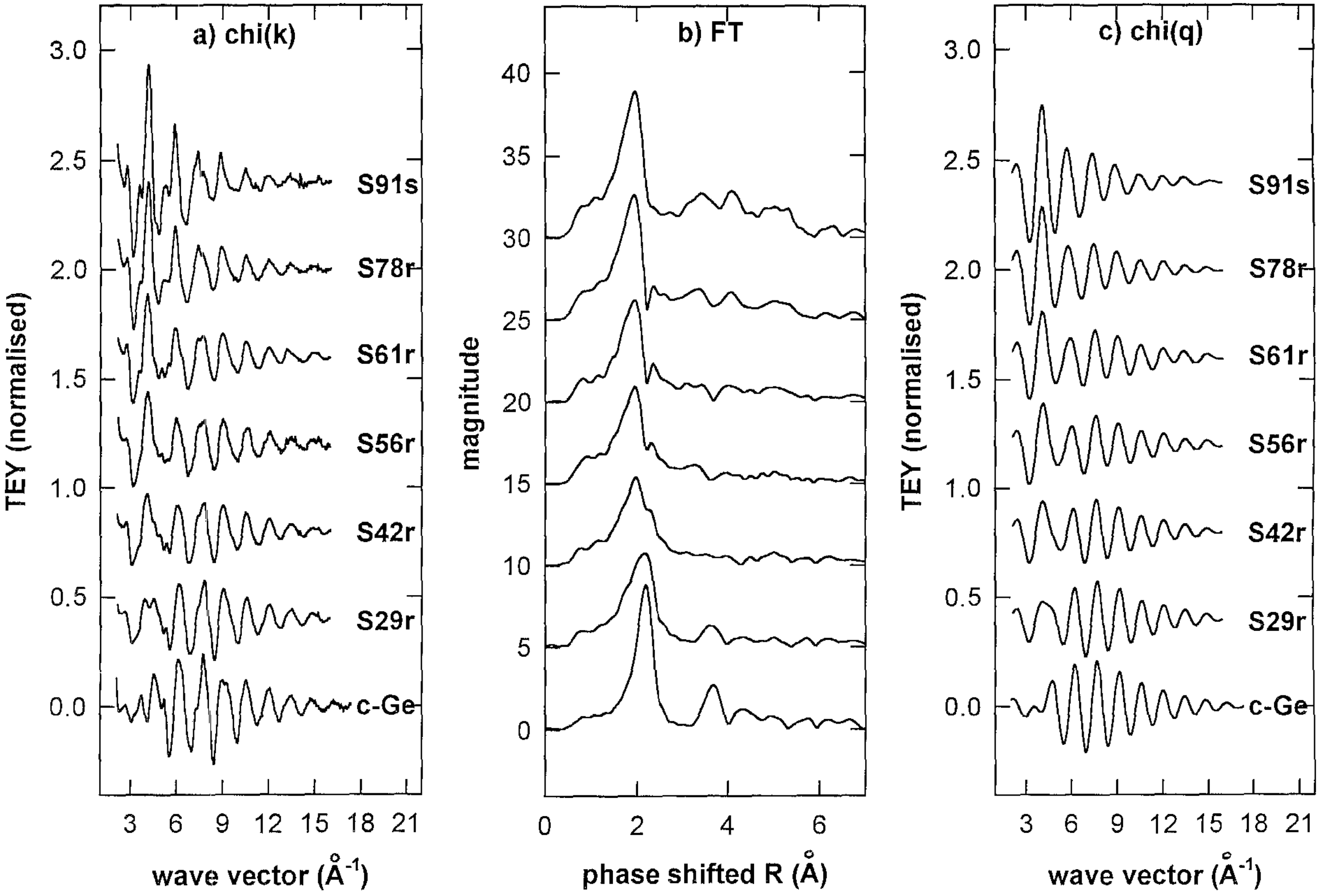

Figure 5.5 - Ge K-edge spectra: a) chi(k) spectra, b) Fourier transforms of a), and c) first shell Fourier filtered spectra obtained from b). Note the transition from Ge-dominated to Si-dominated backscattering, as the % Si content increases.

Table 5.1: Bandit Parameters For Data Processing

Bandit Parameter:	Ge K-edge Spectra	Si K-edge Spectra
Edge height calibration point	0.5	0.5
E_0 shift (eV)	0.0	0.0
E_{min}, E_{max} (eV)	15.0, 1000	19.0, 630
k_{min}, k_{mac} (Å)	2.0, 16.0	2.0, 12.8
k weighting	1	1
Spline polynomial order, no. of sections	3,3	3,3
Window type, sill steepness factor	symmetric, 0.300	symmetric, 0.300
Window limits r_{min}, r_{max} (Å)	0.4, 3.0	0.4, 3.0

5.2 Non-Linear Least Squares Curve Fitting

5.2.1 Introduction To EXAFS Curve Fitting

Once the experimental spectra have been obtained and methodically processed to obtain the Fourier-filtered first shell $\tilde{\chi}(q)$ spectra, there remains the rather arduous task of extracting quantitative structural information. A popular method of doing this involves fitting the EXAFS equation (Equation 2.5) to the $\tilde{\chi}(q)$ data, producing quantitative results for the EXAFS parameters, r_j, N_i, σ_j, and $E_{0,l}$ for each absorber-backscatterer pair. Non-linear curve fitting is a complex process, with abundant difficulties. Proper fitting analysis requires not only a detailed understanding of the critical parameters, but also an effective strategy.

5.2.2 Fitting Models

Aside from data processing, the most critical aspect of EXAFS fitting is choice of models to be used in the fitting routine. As mentioned previously, fitting requires the use of phase shifts, $\delta_j(k)$, and atom-specific amplitude functions, $f(\pi,k)$ for each type of co-ordination being fitted. Viable options for use as models in SiGe fitting are tabulated below:

Table 5.2: Models For Use in EXAFS Curve Fitting

Heteroatomic Co-ordination	Homoatomic Co-ordination
Experimental GaP	Experimental c-Si and c-Ge
FEFF calculated	FEFF calculated
Experimental GaP corrected by FEFF calculated	

Each of the models listed in Table 5.2 has its own benefits and drawbacks, which will be discussed below.

For homoatomic bonding, amplitude functions and phase shift models for Ge-Ge and Si-Si bonding were extracted from experimental EXAFS data for crystalline Ge and Si, respectively. Crystalline Ge and Si represent perfect models for homoatomic bonding in SiGe alloys. Nonetheless, the XAFS calculation package FEFF6.01, was used to produce calculated models [R+91], in hopes that using these models would perhaps eliminate the inadequacies of the heteroatomic FEFF models. The calculations produce theoretical EXAFS spectra for user defined atom clusters. For the calculated homoatomic models, the defined structures were Ge or Si atoms in a 191 atom cluster (10 co-ordination shells) approximating the crystalline Ge or Si lattice. Processing from the calculated energy space absorption curve was performed in an identical manner to that of the SiGe alloy EXAFS spectra, except the energy range of the data was extended to a slightly lower $\mathbf{E_{min}}$. When fitting, $\mathbf{E_0}$ changes result in the compression/expansion of the model spectra q-range (because $\mathbf{E_0}$ determines the linearity of the k-scale - see equation 2.3), and fitting is limited to the length of the model. Thus it is useful to have longer model data ranges than fitted spectra, to avoid truncation of fitted region in the alloy data.

The calculated models for Ge-Ge and Si-Si bonding were tried in the fitting; however, the sums of squares result using these models was significantly higher (by a factor of 4) than when using experimental models. Thus, the experimental c-Si and c-Ge models were selected for the homoatomic models. Note that the data processing for the models was identical to that of the SiGe alloy data, though the useful energy range was extended to account for $\mathbf{E_0}$ shifting in the fitting.

Heteroatomic models for SiGe EXAFS fitting present some interesting problems. As described in Chapter 4, Si K-edge measurements for the ideal experimental models, ultra dilute alloys, are inaccessible to us, and so theoretical FEFF6.01 models and GaP are the available choices. For the theoretical models, the defined structures were impurity atoms (either Ge or Si) substituted onto a site in a cluster approximating a crystalline lattice, without making any changes to any bond lengths. Thus, $\mathbf{r_{GeSi}} = 2.352$ Å, and $\mathbf{r_{SiGe}} = 2.450$ Å in these models. These two structures, Si in c-Ge and Ge in c-Si, are the closest possible representation of ultra-dilute alloys, without making any significant changes to the lattice-approximating host clusters. This method (implicitly Vegard-like in nature) was chosen because the alternative, reconstructing the entire cluster to accommodate bond length strain about the impurity atom, was not viable. The calculations were performed using the correlated Debye models for thermal vibrations for crystalline Si and Ge as an approximation to thermal disorder in real crystals. Additionally, E_0 corrections were made directly in the calculation, in order to account for deficiencies in the Fermi level calculation of the software package [N95].

Experimental GaP EXAFS represent another option available for heteroatomic co-ordination models. Experimental heteroatomic models, when available, can have significant advantages over FEFF calculations. Because the data for the GaP model is obtained in the very same manner as that of the SiGe samples, and processed identically along with the SiGe alloy spectra within the Bandit software, similar systematic errors will be included in the model data. Thus, in the subsequent fitting analysis, one expects that these systematic errors would largely cancel out. Additionally, the FEFF correction procedure detailed by Li et al. [LLB95] was used to improve the match between the experimental model and the SiGe system.

Figures 5.6a-b and 5.7a-b depict the amplitude and phase functions of the heteroatomic models which have been tested in the EXAFS fitting. Table 5.3 lists the models used in fitting, along with the respective sums of squares per data file.

Table 5.3: Criteria For Selection of Heteroatomic Models

Used in Single Edge Fitting

Model	Ge K-edge			Si K-edge		
	N	S/f	N*S/f	N	S/f	N*S/f
GaP	47	4.78E-03	0.23	41	6.93E-02	2.84
FEFF corrected GaP	47	7.26E-03	0.34	41	8.14E-02	3.34
FEFF	47	9.46E-03	0.45	41	6.77E-02	2.78

Note: N is the number of parameters, and S/f is the sums of squares per file.

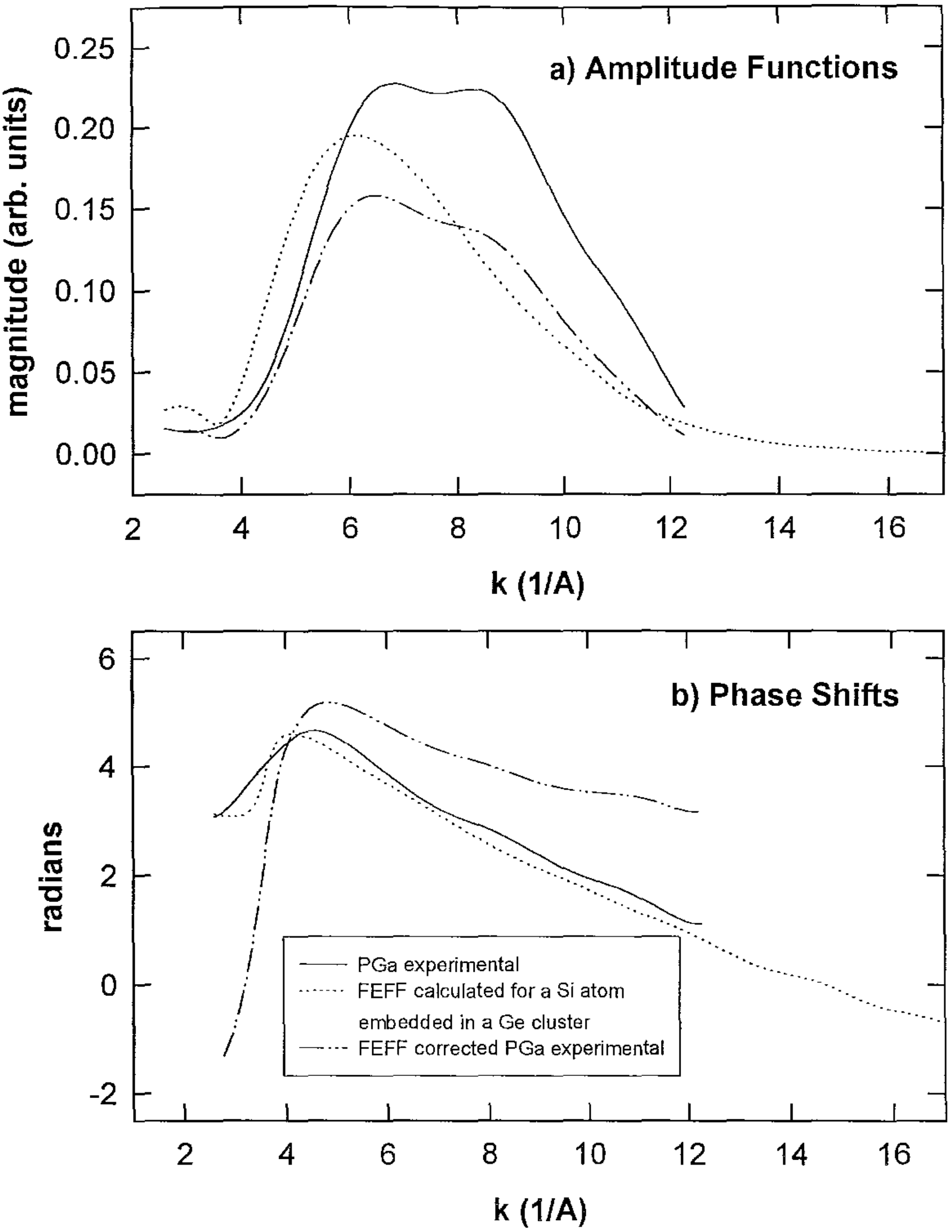

Figure 5.6 - Fitting models for Ge backscattering around a Si central atom.

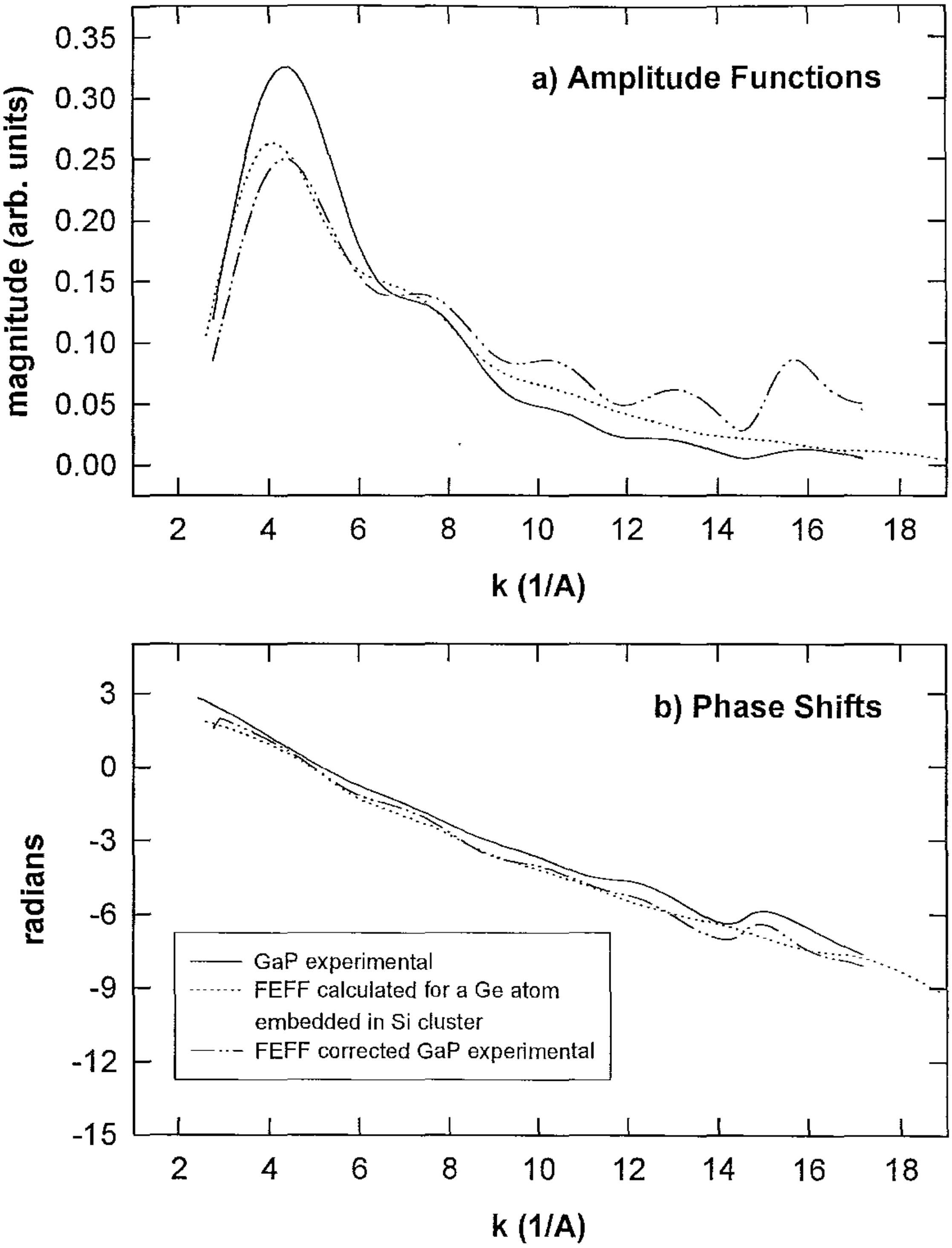

Figure 5.7 - Fitting models for Si backscattering around a Ge central atom.

Of immediate note is the presence of large, unphysical oscillations in the FEFF-corrected GaP model for Si around a central Ge atom (Figure 5.7). These oscillations are a result of the correction procedure (the smaller oscillations in the FEFF amplitude functions create much larger analogues in the FEFF corrected spectra). The resulting fit using these spectra are extremely poor, as evidenced by the much higher sums of squares in Table 5.3. For Ge EXAFS, the best heteroatomic model has proven to be GaP; however, fitting Si K-edge data with P K-edge GaP model spectra produces non-physical results. For Si K-edge data, FEFF models have proven to be the best. Thus, it appeared as though the FEFF theoretical models were the best option, in the single edge fitting. In the multifitting (detailed below), various models were tested again. In addition to the GaP and FEFF models (FEFF-corrected GaP was left out), mixed GaP and FEFF was attempted. Also, a modified approach was tried for the FEFF models: the same model phase and amplitude functions were used, but within the fitting software, the value of the bond length of the heteroatomic model was changed to approximately that predicted by Martins and Zunger [MZ84], i.e. $\mathbf{r}_{GeSi}$ = 2.380 Å (dilute Ge in Si), and $\mathbf{r}_{SiGe}$ = 2.420 Å (dilute Si in Ge). The purpose of this was to try to avoid the implicit Vegard assumption in the FEFF structure. The resulting sums of squares per file are detailed in Table 5.4:

Table 5.4: Criteria For Evaluating Heteroatomic Models Used In Multifit

Model	N	S/f	N*S/f
GaP	88	2.31E-02	2.03
mixed GaP/FEFF	88	1.91E-02	1.68
FEFF	88	1.26E-02	1.11
modified FEFF	88	1.60E-02	1.41

From the sums of squares result, as well as from the plausibility of the fit results (i.e. whether all spectra were fit reasonably, whether the results were considered physically plausible), we concluded that the FEFF models were the best option.

5.2.3 Simultaneous Fitting of Multiple EXAFS Spectra

Fitting occasionally does not produce physically meaningful results. Parameter correlation, model inadequacies, and complex data processing requirements can all confound fitting. This is a critical problem when dealing with systems having more than one component, i.e. when the fit routine must fit to a complex beating pattern from two backscatterers. This author has experienced significant problems fitting to single spectra, even in the case of high quality Ge K-edge data of SiGe alloys. Quite often, the fitting produced non-physical results as the highly correlated E_0 and **r** values would result in the fit becoming "trapped" in a local minimum in a non-physical region of parameter space.

There are various techniques available for improving fitting. One possible refinement is to fit multiple spectra from similar samples simultaneously. This author has made use of a program entitled MFIT, developed by T. Tyliszczak [A+92], that permits simultaneous fitting. The program allows for a logical basis of the reduction of the number of degrees of freedom (parameters) in the fit. In the case of a series of SiGe alloy spectra, for example, one can force all of the fits to the Ge K-edge spectra to have the same values for the $E_{0,GeGe}$ term, thereby constraining the fitting and producing highly consistent results within the data group. A further refinement on multiple fitting of mixed systems, such as SiGe alloys, involves using data from different absorption edges of different atoms, i.e. both Si and Ge K-edge data [A+92]. Multi-edge MFITting permits simultaneous analysis from two different "perspectives", allowing for more constraints in the fitting. Again, using the SiGe example, one can force the fits to the two edges to have an identical heteroatomic bond length for a given composition (i.e. set r_{SiGe} and r_{GeSi} to be equal). The desired result, of course, is to produce the most accurate quantitative data with the smallest possible error margin, and simultaneous multi-edge multi-sample fitting facilitates this [A+92]. Additionally, the MFIT software permits the user to "tinker" with the fitting parameters in a highly novel manner. For example, this author has experimented with forcing the MFIT program to fit not individual bond lengths to the SiGe alloy series' $\tilde{\chi}(\mathbf{q})$ spectra, but rather linear trend lines (slope and intercepts) to the three distinct groups of bond lengths, r_{GeGe}, r_{SiGe}, and r_{SiSi}. In this manner, one can further explore different methods of extracting quantitative results from series of spectra. Figure 5.8 is a portion of a MFIT parameter input file for a reduced sample set.

In this work, all fitting was performed using the MFIT software. A variety of fit strategies (parameter sharing and fixing) was tested. In general, in order to reduce the number of free parameters, we sought to constrain the fitting with parameter sharing as much as possible. Thus, the heteroatomic bond lengths for the same sample, measured at the two different absorption edges, were forced to be the same, where possible. In addition, the $\mathbf{E_{0,GG}}$, $\mathbf{E_{0,GS}}$, $\mathbf{E_{0,SG}}$, and $\mathbf{E_{0,SS}}$ terms were shared as well, i.e. all Ge K-edge data was fit with the same $\mathbf{E_{0,GG}}$, and $\mathbf{E_{0,GS}}$ terms, while all Si K-edge data was fit with the same $\mathbf{E_{0,SG}}$, and $\mathbf{E_{0,SS}}$ terms. This was the basic strategy from which we tested other methods, such as fixing the homoatomic $\mathbf{E_0}$ terms, or forcing the heteroatomic Debye-Waller factors for the same sample to be the same at both Ge and Si K-edges ($\sigma^2_{GeSi}(\mathbf{x}) = \sigma^2_{SiGe}(\mathbf{x})$ for all $\mathbf{x}$). Table 5.4 below lists the resulting sums of squares per file for the various methods:

```
No files= 4  No of parameters=24

No comp in file
1   1  gexx1.f
2   1  g1201x.f
2   1  1201x3.f
1   1  sijan95s.f
No of amplitude model files  = 4
1   2.447E+00  1  4.000E+00 gexx1.a
2   2.352E+00  1  4.000E+00 models\gesixmu.a
3   2.352E+00  1  4.000E+00 sijan95s.a
4   2.447E+00  1  4.000E+00 models\sigexmu.a
No of phase shift model files= 4
1   2.447E+00  gexx1.p
2   2.352E+00  models\gesixmu.p
3   2.352E+00  sijan95s.p
4   2.447E+00  models\sigexmu.p
F  1A  1P  2A  2P  3A  3P  4A  4P - Attr of model # to file
1   1   1
2   1   1   2   2
3   4   4   3   3
4           3   3
No Nam    value      - fitting parameters
 1 rg1  2.447E+00  2 ng1  4.000E+00  3 dg1  1.500E-03  4 eg1  0.000E+00
 5 rg2  2.425E+00  6 ng1  2.000E+00  7 dg2  1.500E-03  8 eg2  0.000E+00
 9 rs2  2.395E+00 10 ns1  2.000E+00 11 ds2  1.500E-03 12 es2  0.000E+00
13 rg3  2.395E+00 14 ng1  2.000E+00 15 dg3  1.500E-03 16 eg3  0.000E+00
17 rs3  2.365E+00 18 ns1  2.000E+00 19 ds3  1.500E-03 20 es3  0.000E+00
21 rs4  2.352E+00 22 ns1  4.000E+00 23 ds4  1.500E-03 24 es4  0.000E+00
Matrix of parameters (b-fit par, a-coeff, i-file #, j-comp #
a(1,i,j)*b(m)+a(2,i,j)*b(n)+a(3,i,j) + a(4,i,j)*dexp(a(5,i,j)*b(k))
file 1 component 1
R  1.000E+00  1  0.000E+00  0 0.000E+00  0.000E+00  0.000E+00   0
N  1.000E+00  2  0.000E+00  0 0.000E+00  0.000E+00  0.000E+00   0
D  1.000E+00  3  0.000E+00  0 0.000E+00  0.000E+00  0.000E+00   0
E  1.000E+00  4  0.000E+00  0 0.000E+00
file 2 component 1
R  1.000E+00  5  0.000E+00  0 0.000E+00  0.000E+00  0.000E+00   0
N  1.000E+00  6  0.000E+00  0 0.000E+00  0.000E+00  0.000E+00   0
D  1.000E+00  7  0.000E+00  0 0.000E+00  0.000E+00  0.000E+00   0
E  1.000E+00  4  0.000E+00  0 0.000E+00
file 2 component 2
R  1.000E+00  9  0.000E+00  0 0.000E+00  0.000E+00  0.000E+00   0
N  1.000E+00 10  0.000E+00  0 0.000E+00  0.000E+00  0.000E+00   0
D  1.000E+00 11  0.000E+00  0 0.000E+00  0.000E+00  0.000E+00   0
E  1.000E+00 12  0.000E+00  0 0.000E+00
file 3 component 1
R  1.000E+00 09  0.000E+00  0 0.000E+00  0.000E+00  0.000E+00   0
N  1.000E+00 14  0.000E+00  0 0.000E+00  0.000E+00  0.000E+00   0
D  1.000E+00 15  0.000E+00  0 0.000E+00  0.000E+00  0.000E+00   0
E  1.000E+00 16  0.000E+00  0 0.000E+00
```

Figure 5.8 - Portion of a sample user-inputted parameter file for the MFIT program.

Table 5.5: Criteria For Evaluating Fit Strategies

Strategy	N	S/f	N*S/f
Basic	67	1.24E-02	0.83
Homoatomic E_0s Fixed at 0.0	67	1.26E-02	0.84
Shared Debye-Waller Factors	63	1.72E-02	1.08

The basic strategy produced the best fit by sums of squares; however, fixing the homoatomic E_0 terms reduced the amount of scatter in the bond length-composition plot (see Chapter 6 below). This strategy involves the assumption that the muffin tin potentials for the homoatomic atom pair is not a function of composition, which is reasonable (conversely, for the heteroatomic atom pair, the E_0 terms cannot be shared, since the heteroatomic models are different for the two environments, i.e. Si around a Ge central atom, and Ge around a Si central atom). Unfortunately, forcing the fits to share heteroatomic Debye-Waller factors did not improve the fit. This is probably a result of a lack of flexibility in the fitting, i.e. not enough free parameters for the fitting to find the global minimum. Thus, the fitting strategy employed in this work was the basic strategy, described above, with the homoatomic E_0 terms fixed at 0.0.

In this work, two fits were performed: Fit 1, which was an exploration of the bond length dependence upon composition for a wide range of alloys, and Fit 2, which was an exploration of bond lengths for a small selection of complimentary strained and relaxed samples grown on Si(100). For Fit 1, Si and Ge K-edge q-space data were combined for the alloys S50r, S60r, S75r, and S90s. Additionally, Ge K-edge q-space spectra for S25r and S40r were included. The corresponding Si K-edge spectra for these two samples were too contaminated by the I_0 oscillation, and hence, unusable. Note that all samples are relaxed, excepting S90s, for which the amount of strain (magnitude of the strain tensor) is very slight, due to the very high Si content.

Experimental q-space spectra for crystalline Si and Ge were also included in the fit, in order to expand the data range and help stabilize the fit.

For Fit 2, Ge K-edge q-space data for alloys S50s, S50r, S75s, and S75r were included in the fitting. Si K-edge q-space data was also included for S50r, S75r, and S75s; however, Si K-edge data for S50s is unavailable, due to the extreme thinness of the sample (too much contamination by the Si(100) substrate in the TEY signal). All other aspects were performed identically as in Fit1, i.e. inclusion of crystalline Si and Ge in the fitting, shared homoatomic E_0 parameters (fixed at 0.0), and shared $\mathbf{r_{SG}}$, where possible.

5.2 Error Analysis Methodology

Estimations of uncertainties in the final results are a critical part of any analysis, and EXAFS analyses are no different. In EXAFS data fitting, many options are available for error analysis; however, one of the more common methods is to vary individual EXAFS parameters until a significant change in the sums of squares is observed. Parameters are typically adjusted in both directions, i.e. positively and negatively, as the sums of squares is, to a first approximation, parabolically dependent upon the change in the best fit value for the parameter. Note that the selection of the significance of change in the sums of squares is quite arbitrary; Matsuura et al. chose 100% [MTC93], while Aldritch et al. [ANS94] and Li et al. [LLB95] chose 10%.

Using this method for error analysis, one has a important choice: for a given change in an EXAFS parameter, one must choose whether to allow the program to refit the spectra with the new, fixed parameter value, or whether to not allow for a refit. Refitting is more conservative, in that it better accounts for parameter correlation effects in determining the sums of squares [N95]; however, most programs (including

MFIT) cannot "sense" what are physical or unphysical results for a given parameter. Thus, in minimizing the sums of squares, the free parameters can adopt clearly unphysical values that would otherwise be rejected immediately. Thus, the error bars are too broad. The alternative, not allowing a refit, is not considered to be more accurate in determining the true error value [N95].

In this work, EXAFS parameter errors were evaluated according to the magnitude of a parameter change required to change the overall sums of squares by a factor of (10% divided by the number of spectra - 14). Additionally, after the parameter was changed and fixed, the program was allowed to refit. The resulting maximum and minimum values for the parameters were used for the error bars, and the best fit value was changed to the midpoint between the maximum and minimum errors. A significant problem with this method, however, is an implied assumption that each spectrum contributes equally to the sums of squares. This is a poor assumption, in that the Si K-edge data is significantly shorter in length than that of the Ge K-edge. While there are less points in the Si K-edge data to contribute to the sums of squares, there are less points in which to fit the EXAFS parameters. From fitting spectra individually, we have determined that Si K-edge data contributes approximately twice as much to the sums of squares as Ge K-edge data does. Thus, the error bars found for bond lengths were scaled by a ratio of the data lengths: Ge K-edge error bars were reduced by a factor of 1.25 (16/12.8), while the Si K-edge error bars were increased by the same factor. Aside from the above arguments, the justification for this scaling is apparent in the results (presented in Chapter 6), where the adjusted error bars better match the actual spread of the data points.

6.0 RESULTS AND DISCUSSION

The results of the EXAFS fitting are described in this chapter, along with a discussion of the results in the context of the literature. The first section details the fitting process, and presents the results of Fit1, the R vs. %Si plots for a compositional range of relaxed SiGe alloys. The second section details the separate set of results for Fit2, a preliminary investigation into strain/relaxed bond length comparisons.

6.1 EXAFS Fitting Results: Fit 1

Figures 6.1 and 6.2 show the fitted spectra from the multfit to the Fourier filtered Ge and Si K-edge data. Generally speaking, the fits are not perfect, showing substantial residuals in places (especially in the beat region (5-7 $Å^{-1}$) where the Si and Ge backscattering signals interfere strongly). Contributing factors to the residuals include such things as the I_0 oscillation in the Si K-edge data, model inadequacies, and inadequate background subtraction. Additionally, the constraints of the combined multifitting are contributing factors as well. Nonetheless, given the complexity of the SiGe system, and the difficulty experienced in data processing, the fits are considered to be acceptable. The results of the combined multifit are tabulated below:

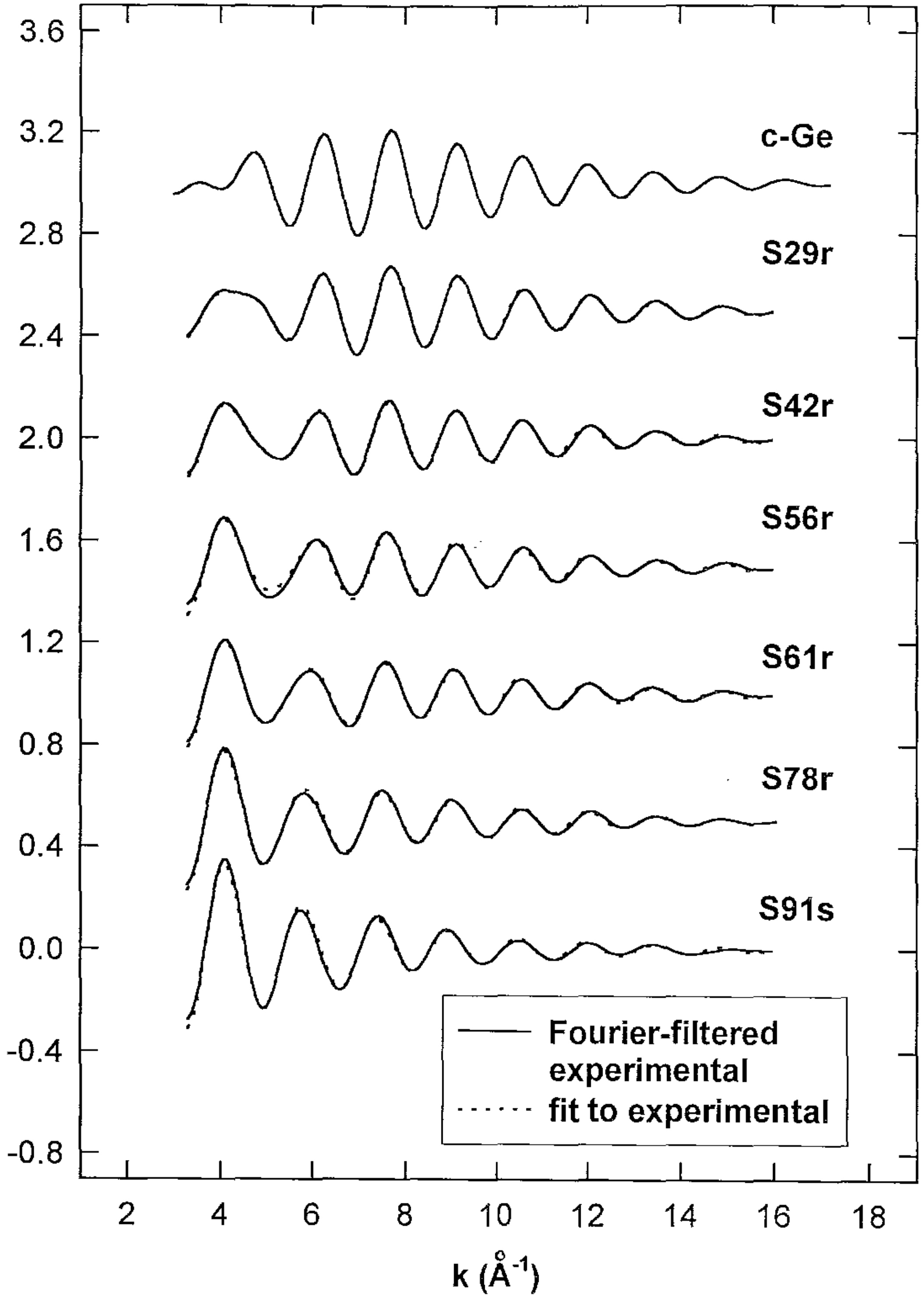

Figure 6.1 - Fit 1 fitted spectra for Ge K-edge experimental spectra

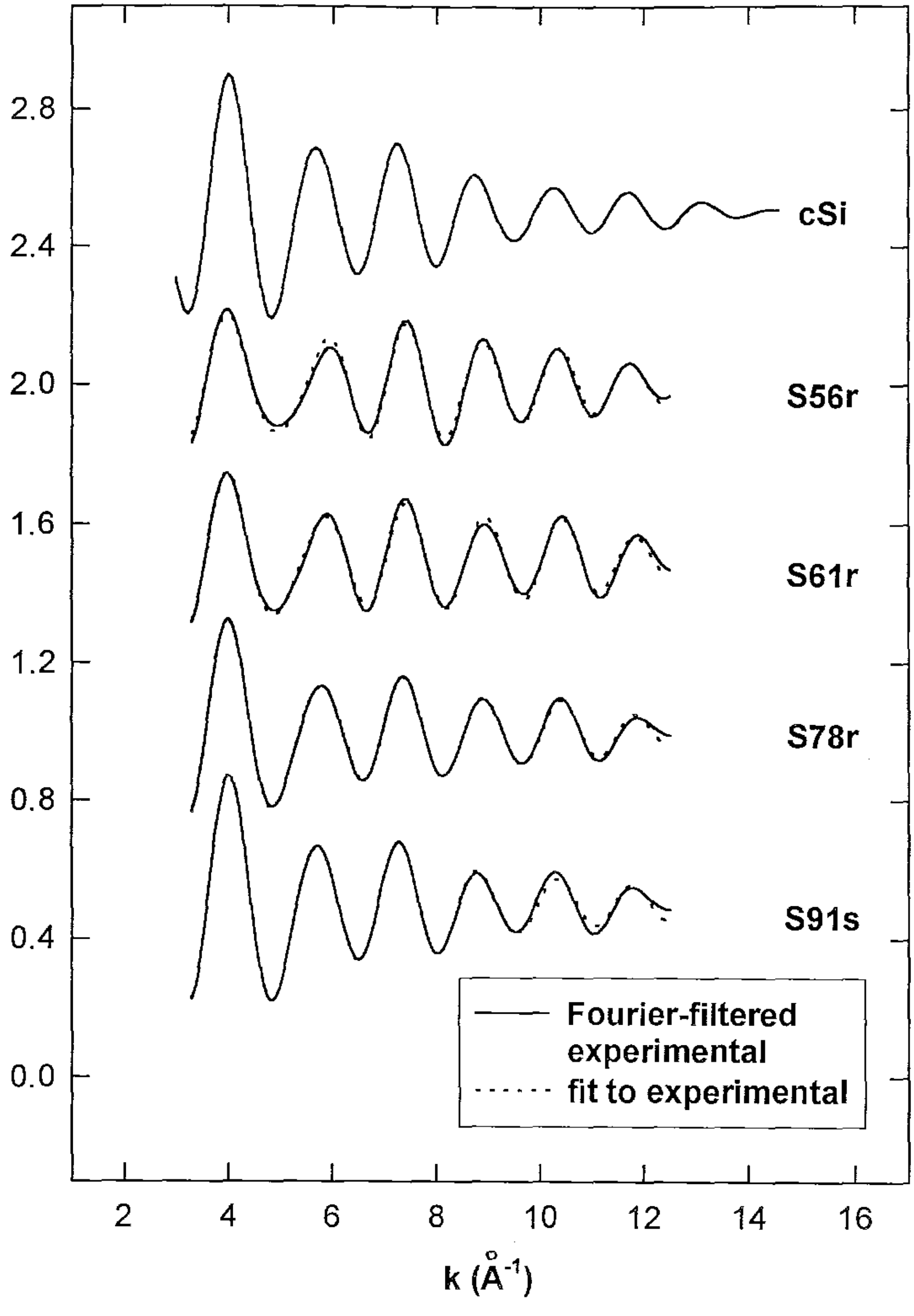

Figure 6.2 - Fit 1 fitted spectra for Si K-edge experimental spectra

Table 6.1: EXAFS Fit Results For Fit1

Ge K-edge

Sample	r_{GeGe} (Å)	+/-	r_{GeSi} (Å)	+/-	N_{Ge}	+/-	N_{Si}	+/-	σ^2_{GeGe} ($*10^{-3}$)	σ^2_{GeSi} ($*10^{-3}$)
cGe	2.450	0.002			4.00	0.20			3.3	
S29r	2.438	0.008	2.407	0.018	3.63	0.50	1.06	0.30	3.8	3.0
S42r	2.438	0.008	2.402	0.012	2.84	0.45	1.51	0.25	4.0	3.0
S56r	2.439	0.009	2.400	0.009	2.30	0.40	2.06	0.25	3.3	6.2
S61r	2.433	0.012	2.400	0.007	2.01	0.45	2.08	0.21	3.8	2.8
S78r	2.423	0.019	2.396	0.007	1.44	0.47	2.66	0.23	3.9	3.2
S91s	2.392	0.053	2.391	0.008	0.48	0.34	2.98	0.37	2.1	3.2

Si K-edge

Sample	r_{SiSi} (Å)	+/-	r_{SiGe} (Å)	+/-	N_{Si}	+/-	N_{Ge}	+/-	σ^2_{SiSi} ($*10^{-3}$)	σ^2_{SiGe} ($*10^{-3}$)
S29r	NA		NA		NA		NA		NA	NA
S42r	NA		NA		NA		NA		NA	NA
S56r	2.368	0.007	2.400*	0.009	2.20	0.17	1.91	0.30	1.3	2.8
S61r	2.363	0.007	2.400*	0.007	2.81	0.24	1.08	0.23	3.7	3.6
S78r	2.357	0.005	2.396*	0.007	3.66	0.25	0.70	0.23	4.6	2.9
S91s	2.349	0.005	2.391*	0.008	3.81	0.20	0.16	0.14	2.5	2.5
cSi	2.352	0.002			4.00	0.21			1.9	

*denotes constrained to match the value for Ge K-edge

E_0 Values

E_0 Term		Value	+/-
$E_{0,GeGe}$	fixed at	0.00	
$E_{0,GeSi}$		0.45	0.45
$E_{0,SiSi}$	fixed at	0.00	
$E_{0,SiGe}$		-0.07	1.21

A useful measure of the quality of the fit is to compare the EXAFS sample composition (i.e. co-ordination number ratios) for the two different edges, with that of the known diffraction results. While this is not a completely accurate test, due to the inability to separate out the various S_o^2 terms from the N_j terms, it does help in identifying obviously incorrect fits (perhaps the result of secondary minima, totally inadequate models, etc.). Figure 6.3 depicts the EXAFS co-ordination numbers versus the composition determined from the diffraction results, assuming fully random alloys. As can be seen, the results are in reasonably good agreement in all cases. There is a noticeable difference between the Ge and Si K-edge results; the Ge K-edge fits tend to underestimate N_{Si}, and Si K-edge fits tend to overestimate N_{Si} and underestimate N_{Ge}. This is perhaps a result of the various S_o^2 terms.

Another check on the results of the fitting is to compare the lattice parameter derived statistically from EXAFS bond lengths, with that of found from x-ray diffraction [MTC91]. The average nearest neighbor bond length, <r>, in a random solid solution with an average lattice that is diamond cubic is related to the lattice parameter **a** by:

$$\boxed{<r>=\frac{\sqrt{3}}{4}a} \qquad \textbf{(6.1)}$$

The average nearest neighbor bond length, <r>, can be calculated using EXAFS results according to [MTC91]:

$$\boxed{<r>=(1-x)^2\bar{r}_{GeGe}+x^2\bar{r}_{SiSi}+2x(1-x)\bar{r}_{GeSi}} \qquad \textbf{(6.2)}$$

where **x** is the %Si, and $\bar{r}_{GeGe}$, $\bar{r}_{SiSi}$, and $\bar{r}_{GeSi}$ are the average nearest neighbor bond lengths. For a completely random solution, such as SiGe alloys, these are simply the bond lengths found in EXAFS. Using the average lattice parameter of the obtained from x-ray diffraction, one can compare to the EXAFS-derived lattice parameter:

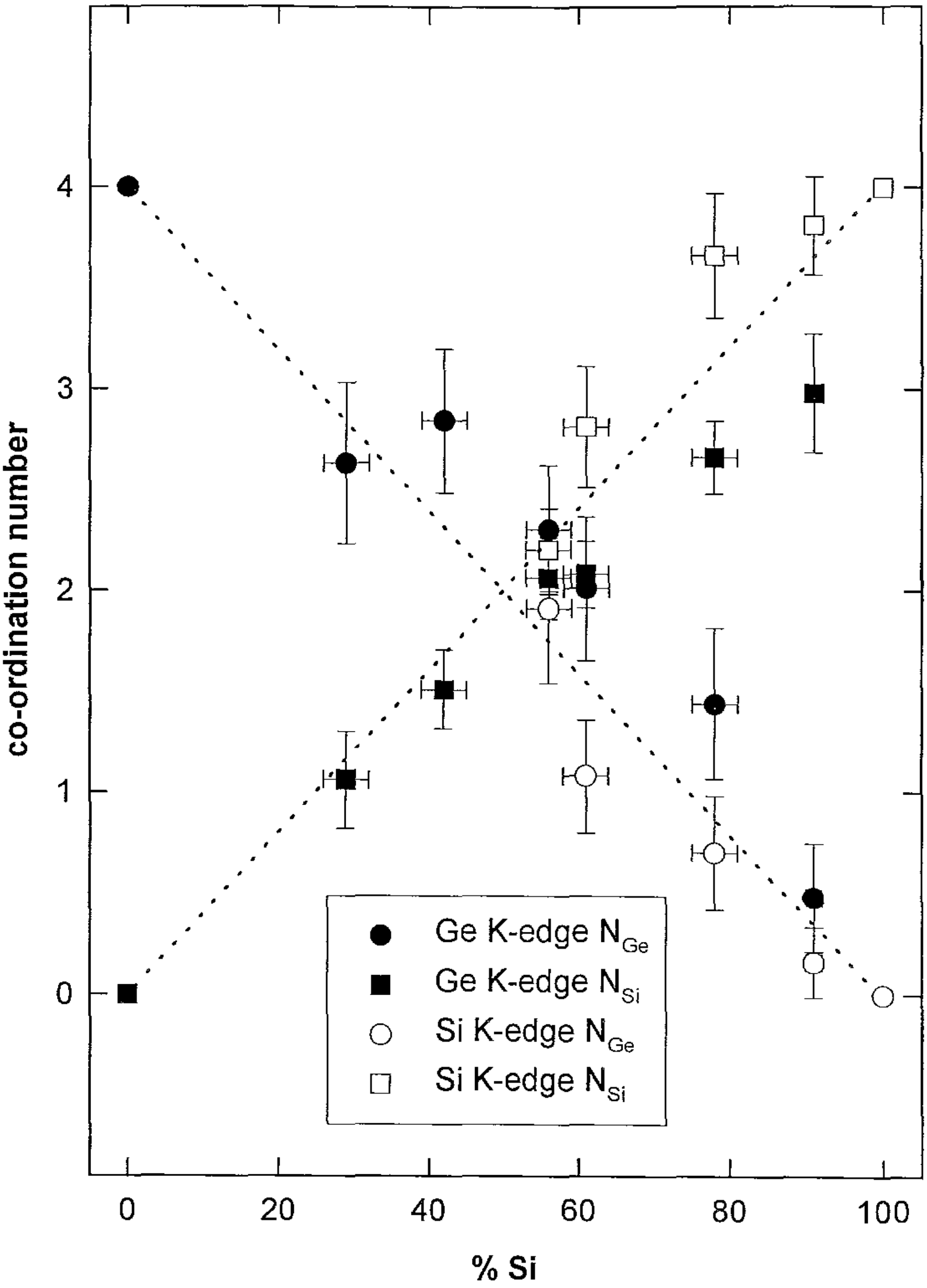

Figure 6.3 - EXAFS co-ordination numbers for Ge and Si K-edge fit results.

Table 6.2: Lattice Parameter Comparisons

Sample	EXAFS-derived <R> (A)	Calculated Lattice Parameter (A)	Diffraction Lattice Parameter (A)	Difference (A)
S29r	2.423	5.596	5.591	0.005
S42r	2.410	5.566	5.558	0.008
S56r	2.402	5.547	5.541	0.006
S61r	2.392	5.524	5.519	0.005
S78r	2.376	5.487	5.480	0.007
S91s	2.357	5.443	5.437	0.006

As can be seen, the agreement is excellent (within 4% of the maximum possible change), which provides further confidence in the EXAFS fit results. The differences are all positive, though, which seems to be somewhat non-statistical. This could be a result of assuming perfect tetrahedral bonding in Equation 6.1.

Figure 6.4 depicts the Debye-Waller terms, σ^2_j, as functions of composition. The error bars in this figure are estimated from the scatter of the points, rather than systematic evaluations. In general, the points seem to cluster (excepting a couple of outliers) in the region 0.002 to 0.005, and could be replaced in the fitting with a single value, were it not for the resulting loss of fit flexibility.

EXAFS fitting is a complicated procedure, and obtaining final results requires the achievement of many interim goals. In this work, interim goals included such stages as Ge K-edge multifits, Si K-edge multifits, and combined, constrained multifits. Figure 6.5 depicts the separate Ge and Si K-edge fit results for bond lengths as functions of composition. In each case, the homoatomic E_0 values were forced to zero, while the heteroatomic E_0 values were shared, but allowed to vary. In presenting the Ge K-edge fit, the R_{GG} result for the most dilute alloy (S91s 91% Si) was not put in the figure, as its corresponding error bars were too large to incorporate. Included in Figure 6.5 are the linear regression lines for the three different bond types. The agreement between the heteroatomic bond lengths, determined from the two separate edges, is not good.

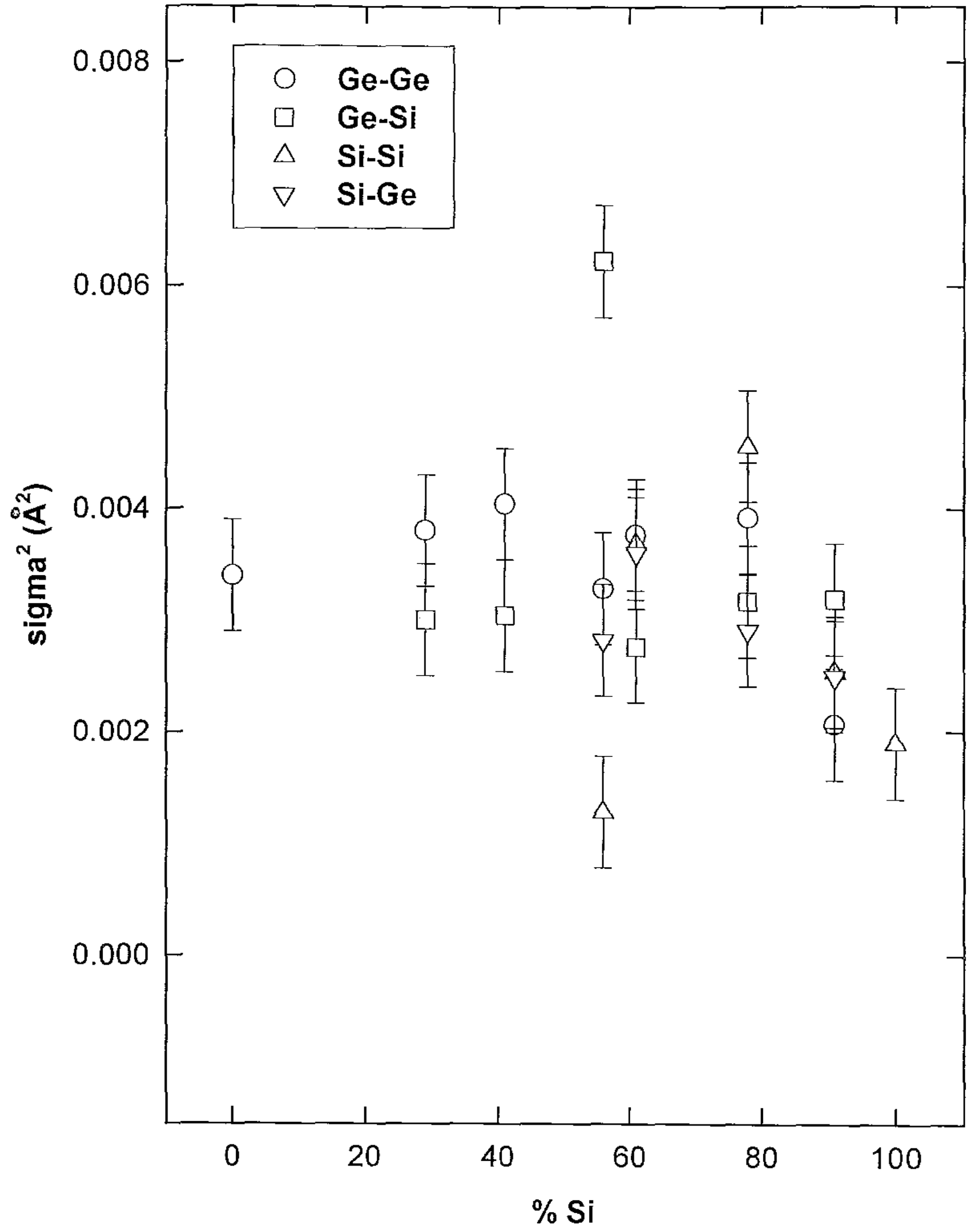

Figure 6.4 - Debye-Waller factors as functions of composition. Clearly, there is no noticeable trend.

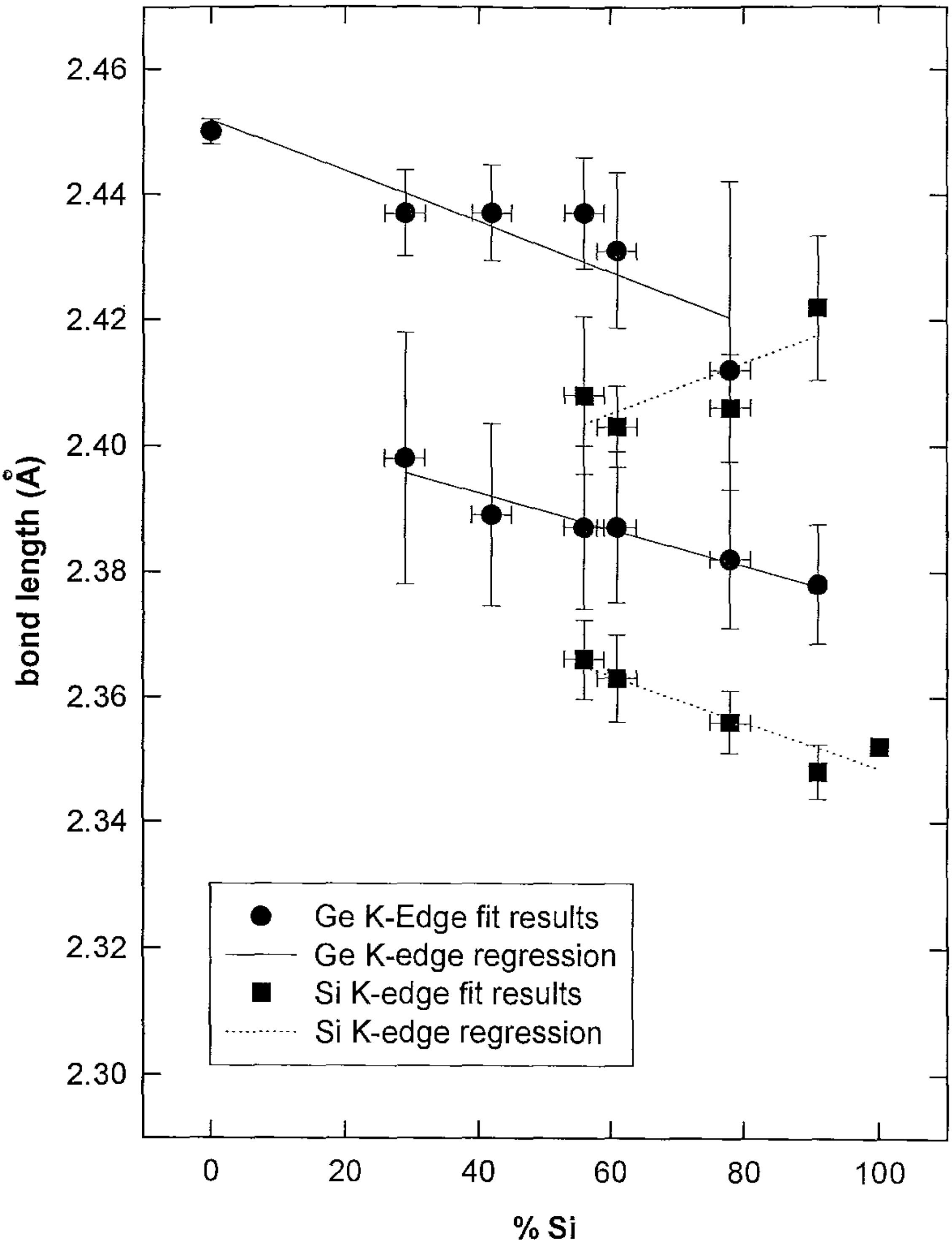

Figure 6.5 - Fitting results for the separate Ge and Si K-edge data. Clearly, the agreement between the results for the two data sets is poor.

Nonetheless, Figure 6.5 represented an interim success in the overall fitting process.

Figure 6.6 depicts the bond length result of the multifit with simultaneous fitting to both Ge and Si K-edge EXAFS data. As in the previous fits, homoatomic E_0 values were fixed at zero, and the heteroatomic E_0 values were shared and allowed to vary. Additionally, the heteroatomic bond length parameters, r_{SiGe} and r_{GeSi}, were shared for the two different K-edge data groups. This constraint is the advantage of multiple data file, multiple edge fitting: in total, the number of independent parameters was reduced from 80 to 67. It was anticipated that doing this would significantly improve the fitting results. Clearly, the results are much better in Figure 6.6 than in Figure 6.5, showing less scatter with error bars that better reflect this.

In keeping with the CT theory, three parallel lines have been fit to the bond length data in Figure 6.6. Using Equation 3.3, and fitting to the data points themselves produces a best fit value of **a**** = 0.70. From the spread of the data points, the possible maximum and minimum **a**** values have been determined, which are 0.79 and 0.67, respectively. Thus, from the results in Figure 6.6, we find that for relaxed SiGe alloys, **a**** = $0.70^{+0.09}_{-0.03}$. Furthermore, our result for the heteroatomic bond length of a 50% alloy (2.402 Å), is in good agreement with the assumption that $r^0_{SiGe} = \frac{1}{2}(r^0_{SiSi} + r^0_{GeGe}) =$ 2.401 Å, made by Cai and Thorpe in developing their analytical model.

The result of **a**** = $0.70^{+0.09}_{-0.03}$ overlaps within the mutual error margins of **a**** = $0.63^{+0.08}_{-0.13}$, determined from Ge K-edge measurements by Aldritch et al. [ANS94]. Figure 6.7 depicts our results, along with the results of Aldritch et al. Of note, is the addition of r_{SiSi} points, and the clear compositional variation in all three bond lengths. Specifically notable is the distinct monotonic trend in the data points for r_{SiGe} of the present work, while the heteroatomic

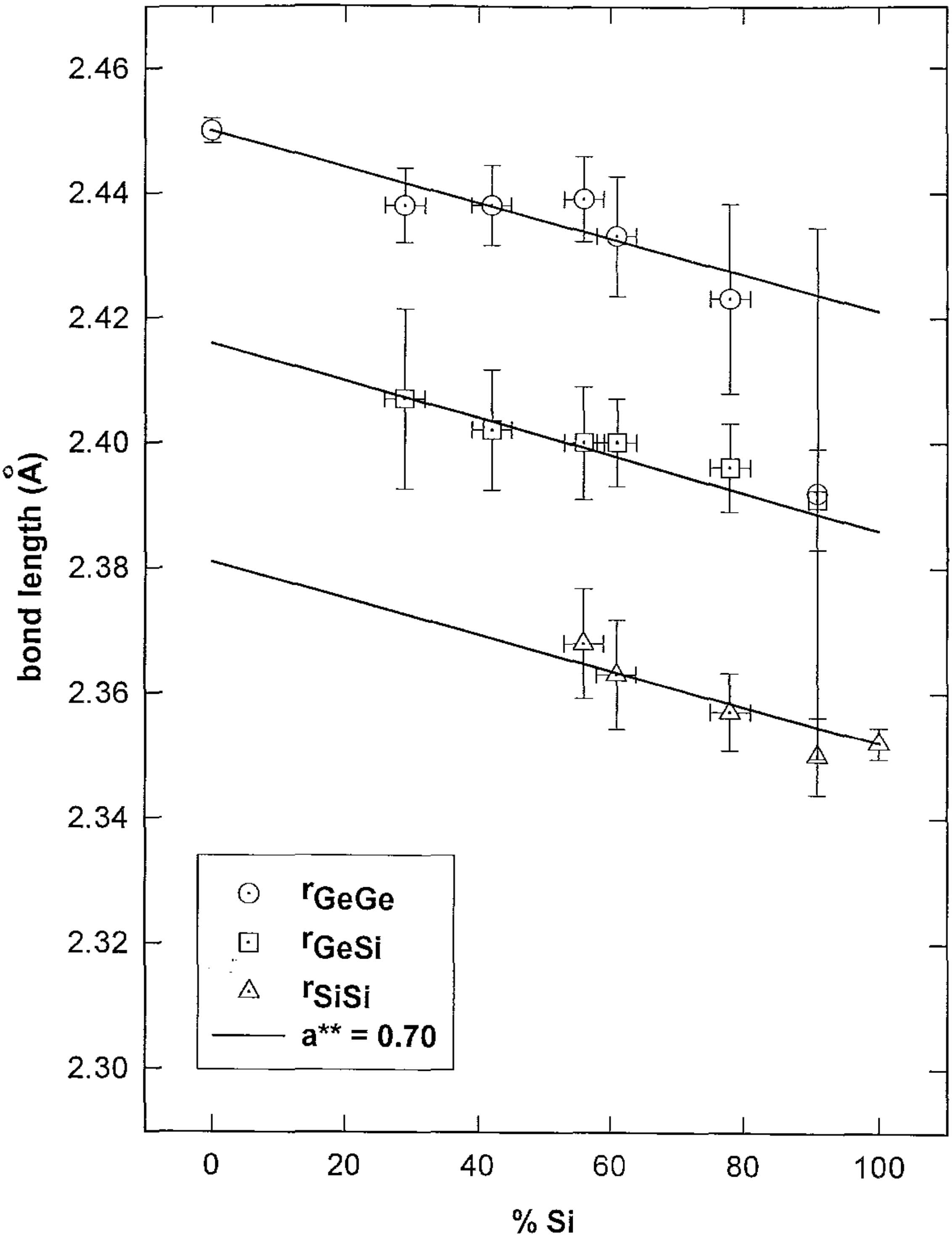

Figure 6.6 - Bond length vs. composition plot for the results of the EXAFS fitting for the SiGe alloys, along with the calculated limits for a** values.

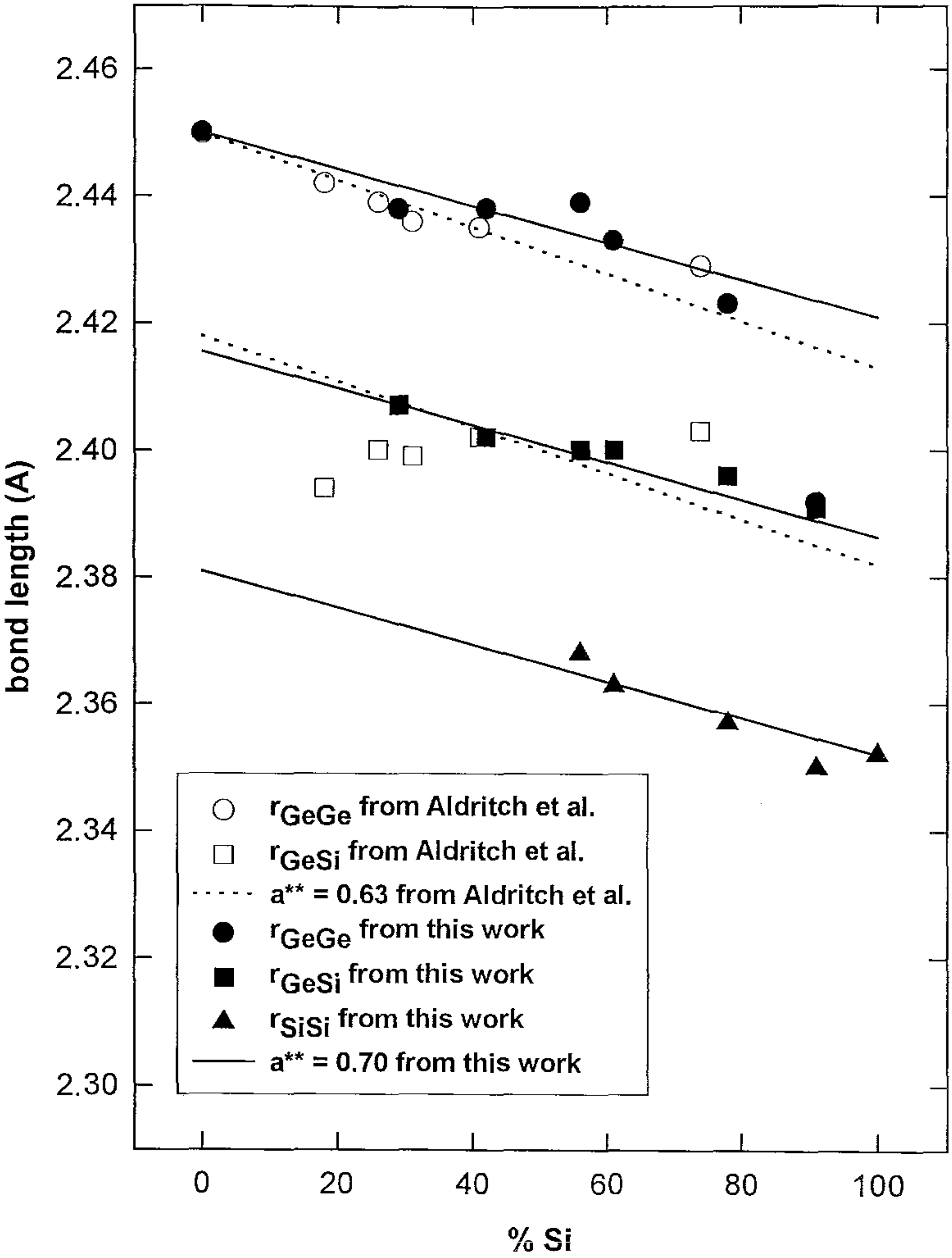

Figure 6.7 - Comparison of the fit results of Aldritch et al. with the results of this work.

bond length data of Aldritch et al. lack this clear trend. In general, though, the results are in rather good agreement.

Figure 6.8 depicts our results along with all the other experimental listed in Chapter 3. Interestingly enough, our results are in reasonable agreement with that of Kajiyama et al. [K+92]. Imposing reasonable error bars on their points (say, ±0.01 for the low %Si samples, double for the higher %Si samples) would bring their results into quite acceptable agreement with our own. The results of Woicik et al. and Matsuura et al., however, are not in good agreement with our results. We attribute the disagreement to their use of only single edge (Ge K-edge) data. In Figure 6.5, our Ge-Ge and Ge-Si bond length results for the separate Ge K-edge fit are similar to those of Woicik et al. and Matsuura et al., i.e. quite different than the results in Figure 6.6 for the constrained multi-edge fit. Of the bond length results for the amorphous materials found by Nishino et al.[N+88], Filliponi et al. [F+86], and Incoccia et al. [I+85], only Filliponi et al. have results that agree somewhat with our own. We attribute the disagreement to the amorphous material, which we feel cannot be directly compared to crystalline material, since the bonding is known to differ significantly [MT92].

The results for **a**** in this work are in excellent agreement with the calculated results presented in Chapter 3 (Figure 6.9). Specifically, the **a**** result in this work is in excellent agreement with the calculated results of de Gironcoli et al., which was calculated by Mousseau and Thorpe to be **a**** = 0.707 [MT92]. The agreement is less, but still reasonable, with Ichimura et al. [I+90], which we calculate to be **a**** = 0.63, and with Martins and Zunger [MZ84], which Aldritch et al. calculate for their results to be **a**** = 0.60.

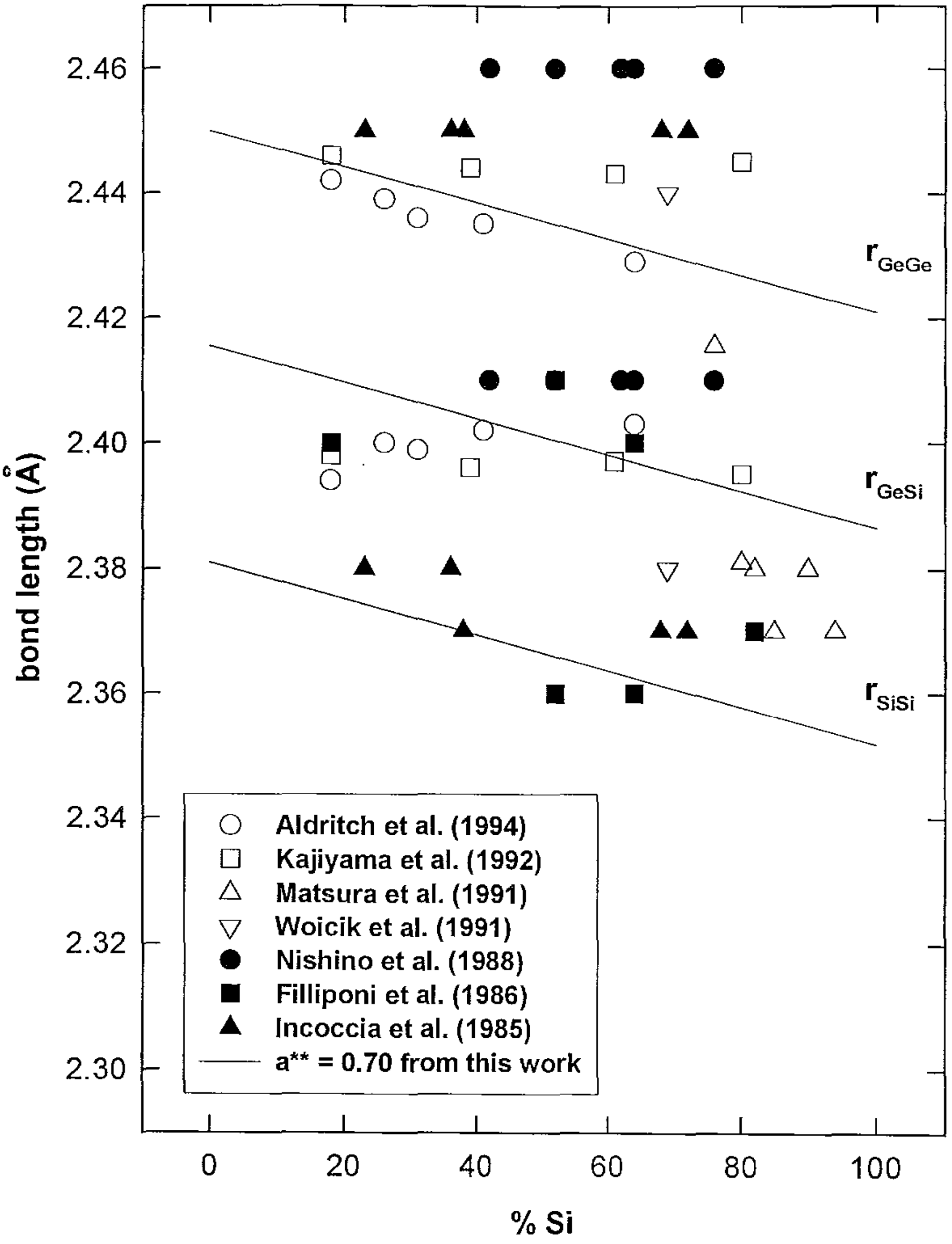

Figure 6.8 - The experimental results of the literature, compared with the results of this work. Open symbols are for crystalline samples, closed symbols are for amorphous samples.

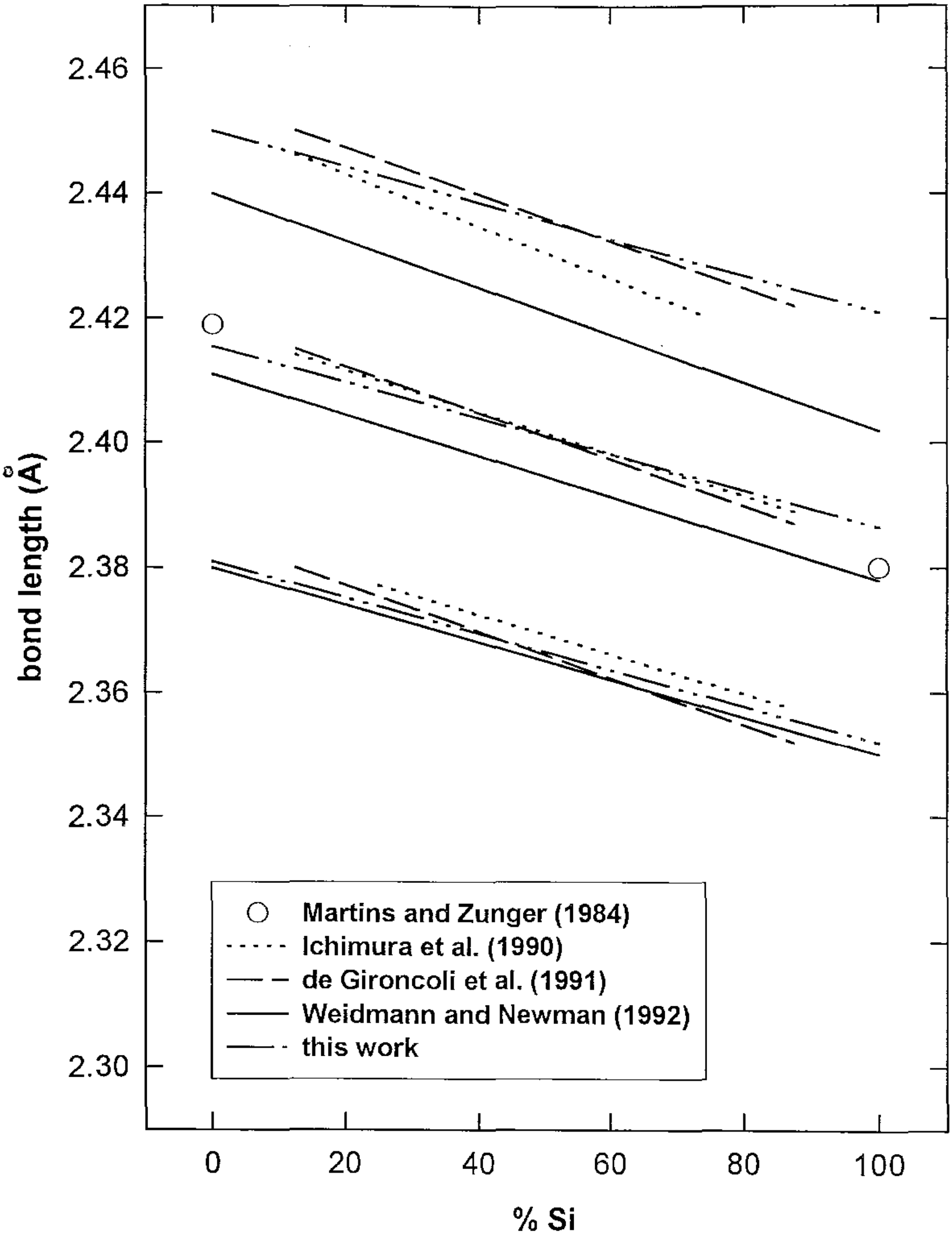

Figure 6.9 - Comparison of the results of Fit 1 with previous calculated results. The agreement is best with the results of Ichimura et al. (1990), and worst with that of Weidmann and Newman (1992).

6.2 Discussion Of Fit 1 Results

Thus, it seems that SiGe alloys have somewhat more rigid lattices than predicted by Pauling (and Bragg), but far softer than predicted by the VCA. The value of **a**** = $0.70^{+0.09}_{-0.03}$ indicates that indeed, the lattice is capable of forcing bond length changes in order to accommodate steric strain, but not much. An examination of EXAFS results of other alloy systems yields similar results, i.e not completely Pauling-dominated bonding, as found here. A previous study [BM83] has found that the highly covalent (In,Ga)As system is very Pauling-like (Cai and Thorpe [CT92] calculated **a**** = 0.8). Sasaki et al. [S+85] found similar bonding, but with more lattice rigidity (more VCA-like) for another III-V, Ga(As,P) (we calculate **a**** = 0.63). Much more ionic materials, such as II-VIs, have also shown similar behavior. Specifically, (Zn,Mn)Se, (Zn,Cd)Te, and (Cd,Mn)Te have been shown to have Pauling-dominated bonding (we calculate **a**** = 0.80. 0.82 and 0.90, respectively) [B+85, P+90, B87]. Even nearly completely ionic materials have demonstrated mixed-type behavior, as evidenced by the results for (K,Rb)Br and Rb(Br,I) (we calculate **a**** = 0.52 and 0.64, respectively) [BM85]. Thus, the highly, but not completely Pauling-type result for **a**** in completely covalent SiGe alloys is not atypical. In fact, the result found in this work seems to be rather typical of semiconductor and ionic alloys.

To our knowledge, there has not been a report in the literature as yet of an EXAFS study of first shell bond lengths in random crystalline metal alloys; however, Frenkel et al. [F+96] have reported a multi-edge (Cu K- and Au L-edges) study of metastable CuAu alloys at the most recent XAFS-9 conference (Grenoble, Aug 1996). They found significant mixed-type behavior in Au-Au, Cu-Au, and Cu-Cu bond lengths, showing appreciable dependence upon composition, much as in the SiGe system (and others described above). Thus, one could say that the mixed bonding description seems to be somewhat standard for alloys in general, regardless of type of material (i.e. semiconductor, ionic salt, metal, etc.).

The CT theory seems to be an adequate description of the bonding in SiGe alloys. The points in Figure 6.7 seem to indicate good agreement between the EXAFS results and the predictions of the theory, at first glance. Looking more closely at the r_{GeGe} results in Figure 6.6, it is possible that the CT theory does not provide an entirely adequate description of bonding at the impurity limits. The work of Martins and Zunger [MZ84] calculated bond lengths of single atom impurities in a host lattice, but what of a dimeric impurity, such as two adjacent Ge atoms in a Si lattice? Would the bond lengths extend to a length of 2.414 Å, as calculated from Figure 6.6? Or, would the surrounding Si lattice force the bond length between the Ge atoms to compress? To our knowledge, calculations such as these do not exist; however, the sample S91s is a reasonably close representation of just this problem. At 91% Si, any Ge-Ge bonding is most likely due to isolated Ge-Ge dimers. The bond length obtained in this work, r_{GeGe} = 2.391 Å, is much shorter than that predicted using the CT theory. Granted, the uncertainty associated with this point is very large, owing to the dilute composition. Nonetheless, the absolute value of the bond length alone, along with the other points for r_{GeGe}, seems to indicate that perhaps a curve through the r_{GeGe} points would be a better model than a straight line. One possibility is demonstrated in Figure 6.10, in the form of hypothetical curves (curves through the r_{GeSi} and r_{SiSi} points are also included). The data points seem to fit very well to this alternative curve shape. It would be extremely useful to see the results of impurity dimer bond length calculations, and see how they compare to the predictions of the CT theory. The results may indeed show that the CT theory underestimates bond length changes at the impurity limits. Weidmann and Newman [WN92] have performed modeling studies of bond length

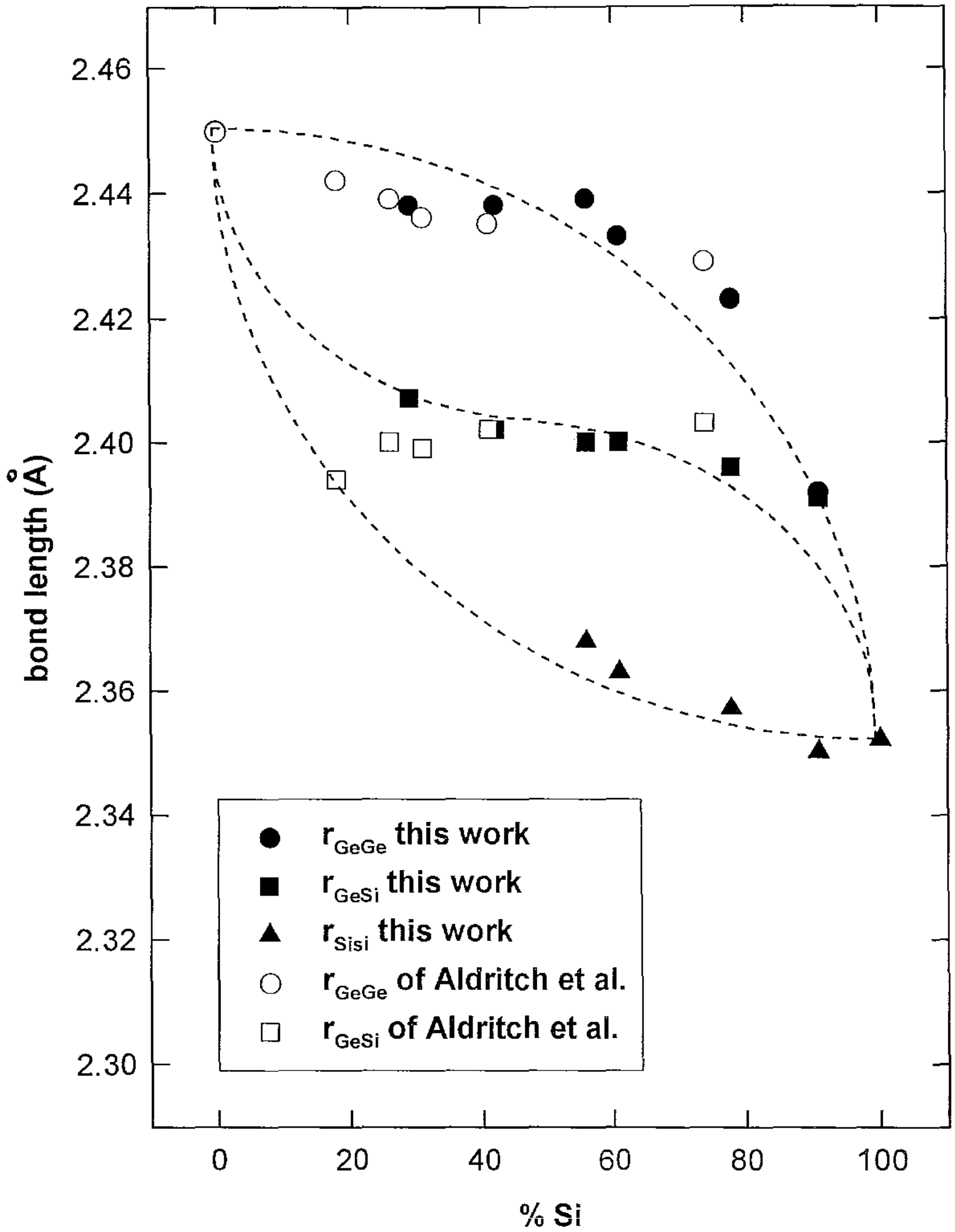

Figure 6.10 - Hypothetical curves (dotted) representing possible non-linear behaviour in bond length-composition curves. The curves fit well to the results of this work; however, the fit to the results of Aldritch et al. is less good, especially with the heteroatomic bond length.

distributions in alloys at the dilute limits, and their results indicated that the distributions were highly complex, i.e. far from the Gaussian-shaped distribution predicted by the CT theory. Thus, the dilute limits could present a very interesting area to explore further.

Also of interest are the findings of Frenkel et al. [F+96], who found that a single **a**** parameter was not adequate to describe the bonding behavior in their CuAu alloys. They determined that their results required *two* parameters, one for Cu-Cu and Cu-Au co-ordination, and another (more Pauling-like) for Au-Au co-ordination. They justified this conclusion with an intriguing model of the CuAu alloy structure. Since Au atoms are significantly larger than Cu atoms, Frenkel et al. reasoned that the Au atoms in the alloy formed a long range network (i.e. "cage") that essentially determined the lattice parameter of the alloy. The Cu atoms, being much smaller, fit into the "holes" in the Au "cage". Thus, $\mathbf{r}_{\mathbf{AuAu}}$ was found to be less dependent upon composition than $\mathbf{r}_{\mathbf{CuAu}}$ and $\mathbf{r}_{\mathbf{CuCu}}$. In support of this model, the authors found from their fitting results that the $\sigma^2_{\mathbf{CuCu}}$ and $\sigma^2_{\mathbf{CuAu}}$ values were significantly larger than that of $\sigma^2_{\mathbf{AuAu}}$. From these results, Frenkel et al. questioned the applicability of the CT theory to all systems. Thus, the utility of the CT theory to all alloys at all compositions is questionable. For sure, further studies in this area are needed.

The SiGe system is often used as an example of a near-ideal solution, possessing 100% miscibility [OB85]. Recent work, however, has shown that SiGe materials grown by non-equilibrium methods, such as MBE or CVD, may not be as ideal as the bulk material. Specifically, published results by a large number of groups seem to indicate that thin film SiGe alloys may have *ordered* regions [C+96, T+95, J+93, J+92, LB92, JPB91, M+91, LKI90, L+90, L+87, L86, MZ86, OB85]. The specific nature of the ordered regions is still a subject of lively debate; however, it seems clear that the ordering is a result of kinetics and strain, and not thermodynamics [GGB91, JPB91].

Tentative structural models for the ordering include CuPt- and CuAu-I-type ordering [T+95], where Ge-Ge and Si-Si dimers are preferentially arranged on various planes.

If significant ordering is present in the SiGe alloys used in this work, the Ge K-edge EXAFS results, particularly the co-ordination numbers, would be significantly affected. For example, in the sample S91s, which has only 9% Ge, ordering of Ge into dimers would increase the amount of Ge-Ge co-ordination from that of a truly random alloy. Thus, Ge K-edge EXAFS measurements of this sample would indicate a local composition significantly different from the long range composition. Additionally, some of the structural models proposed in the literature would involve large microscopic strains [T+95]. This could affect local bond lengths determined from Ge K-edge EXAFS. Diffraction studies of samples grown by the same method (by the same person in the same MBE chamber) as used in this study indicate that the amount of ordered phase is very little [T+95]. Thus, it was anticipated that ordering would have only insignificant effects on the results presented in this work. Nonetheless, we have explored the possibility of whether there is detectable ordering in our results.

Cargill and Spaepen [CS81] developed an order parameter $\Gamma_{A\text{-}B}$, which they used to determine whether ordering of B atoms about a central atom A was detectable in their EXAFS fitting results. The parameter is defined as follows:

$$\boxed{\Gamma_{A-B} = \frac{y}{x}\frac{xZ_A + (1-x)Z_B}{Z_A} - 1} \qquad (6.3)$$

where **y** is the fraction of one type of atom around the central atom (determined from EXAFS), **x** is the composition, and $Z_{A,B}$ is the number of co-ordinated atoms around **A** or **B**. For SiGe alloys, where each atom is 4-co-ordinate, Equation 6.3 reduces to:

$$\boxed{\Gamma_{A-B} = \frac{y}{x} - 1} \qquad (6.4)$$

Thus, a positive value for $\Gamma_{A\text{-}B}$ indicates ordering, while a negative value indicates the opposite of ordering, segregation. For a completely random alloy, the fraction of a given atom around a central atom is equal to that predicted by the composition, and $\Gamma_{A\text{-}B}$ is zero. For a completely ordered alloy, where atom B completely surrounds atom A, Equation 6.3 reduces to [E92]:

$$\boxed{\Gamma_{A-B}^{\max} = \frac{x_A}{1 - x_A}} \qquad (6.5)$$

where x_A is the sample composition in terms of %A.

Figure 6.11 depicts the order parameter calculated for Ge ordering for our Si and Ge K-edge fit results, along with curves for the cases of complete randomness and order. The error bars for the value of the order parameter (± 0.2) were arbitrarily assigned, based upon the minimum size of errors in the co-ordination numbers (note that this is much more conservative than percentage or rms calculations). The comparison of order parameters for high %Si alloys derived from Ge K-edge results relative to those of Si K-edge results is quite interesting. In Figure 6.11, it seems that Ge is preferentially co-ordinated to itself, rather than with Si. The corresponding plot for Si ordering, Figure 6.12, does not show the same distribution.

This suggestion of Ge self-co-ordination is a surprising result, especially since Figures 6.11 and 6.12 indicate that both Si and Ge K-edge EXAFS are sensitive to it.

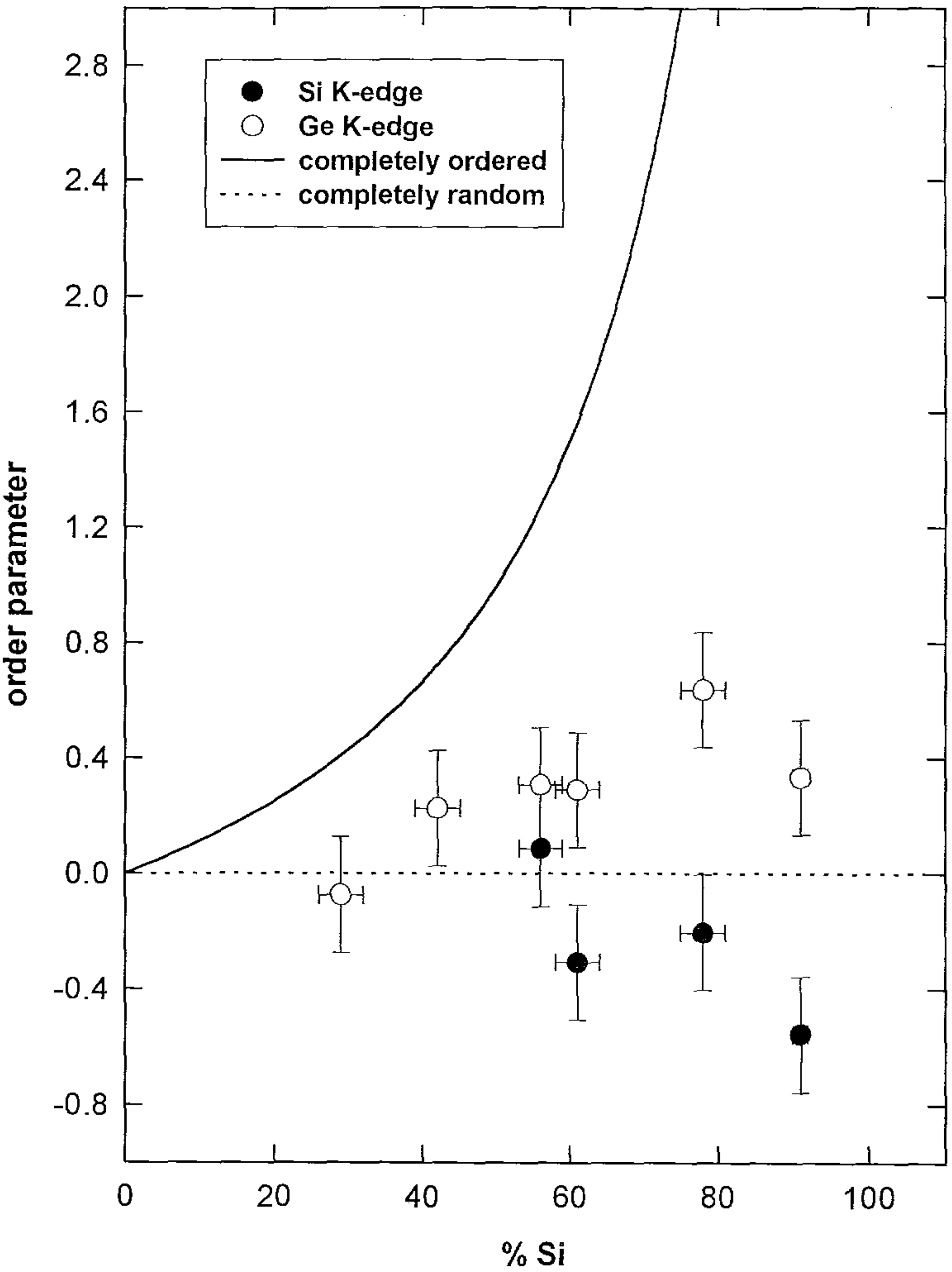

Figure 6.11 - Order parameter as a function of composition for Ge ordering.

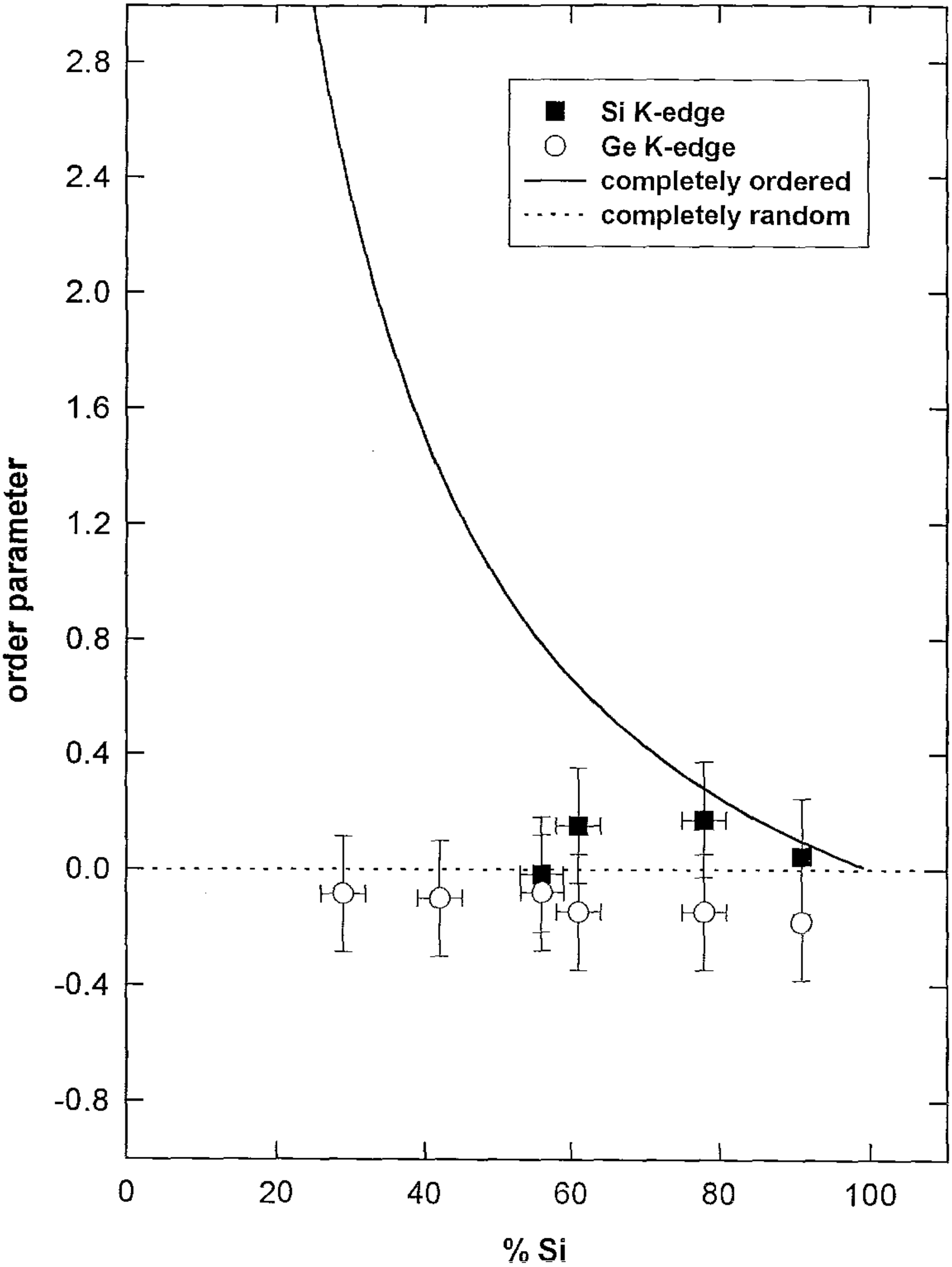

Figure 6.12 - Order parameter as a function of composition for Si ordering.

Whether this is truly indicative of ordering in these samples is unknown. As mentioned previously, we have not made an attempt to account for the passive electron reduction factors. If $\mathbf{S_o^2}$**(GeGe)** was somewhat greater than 1.0, the Ge-Ge co-ordination numbers obtained from the fitting would be too high. This is possible for materials with highly non-spherical charge distributions about the absorbing atom, such as highly covalent systems (i.e. SiGe alloys) [N95, LLB94]. Similarly, if $\mathbf{S_o^2}$**(GeSi)** was somewhat less than 1.0 (somewhat contradictory to the previous two statements, but nonetheless possible), the Ge-Si co-ordination numbers would be too low. The result of these inaccuracies could produce the order parameter distribution seen in Figure 6.11. Until a detailed attempt at analyzing the passive electron reduction factors is made, a clear determination of ordering cannot be made.

Even if there is significant ordering in our samples, an ordering-induced $\mathbf{r_{GeGe}}$ change is unlikely to be observable, given the size of the error bars at such dilute levels of Ge. Most likely, the only observable effect would be a slight distortion in the co-ordination numbers. Thus, we conclude that our results for the bond lengths in SiGe are unaffected by ordering.

6.3 EXAFS Fitting Results: Fit 2

Figures 6.13 and 6.14 show the fitted spectra from the multifit to the Fourier filtered Ge and Si K-edge data. As in Fit 1, the fits are not perfect, again showing substantial residuals. The results are tabulated below:

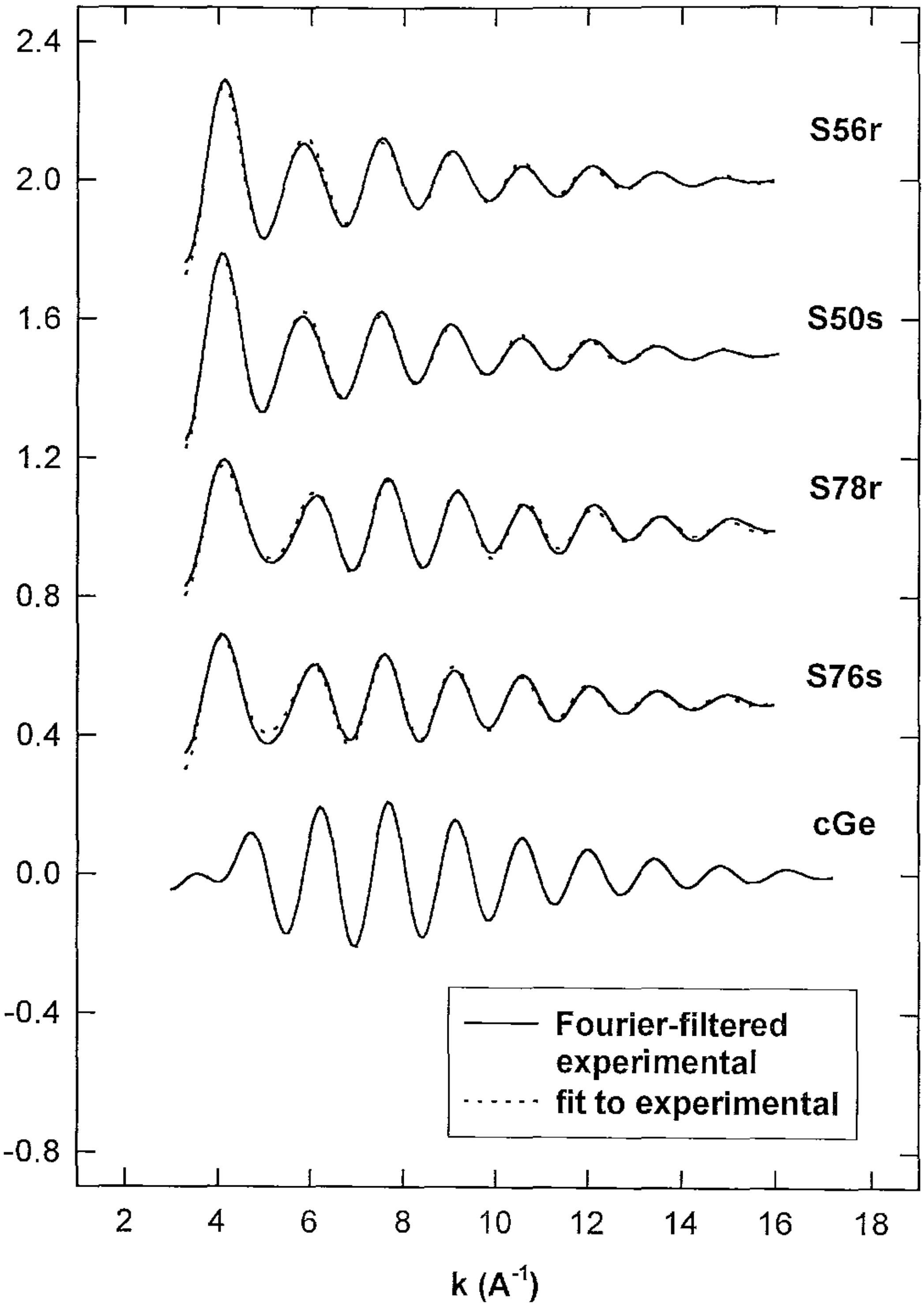

Figure 6.13 - Fit 2 fitted spectra for Ge K-edge experimental spectra

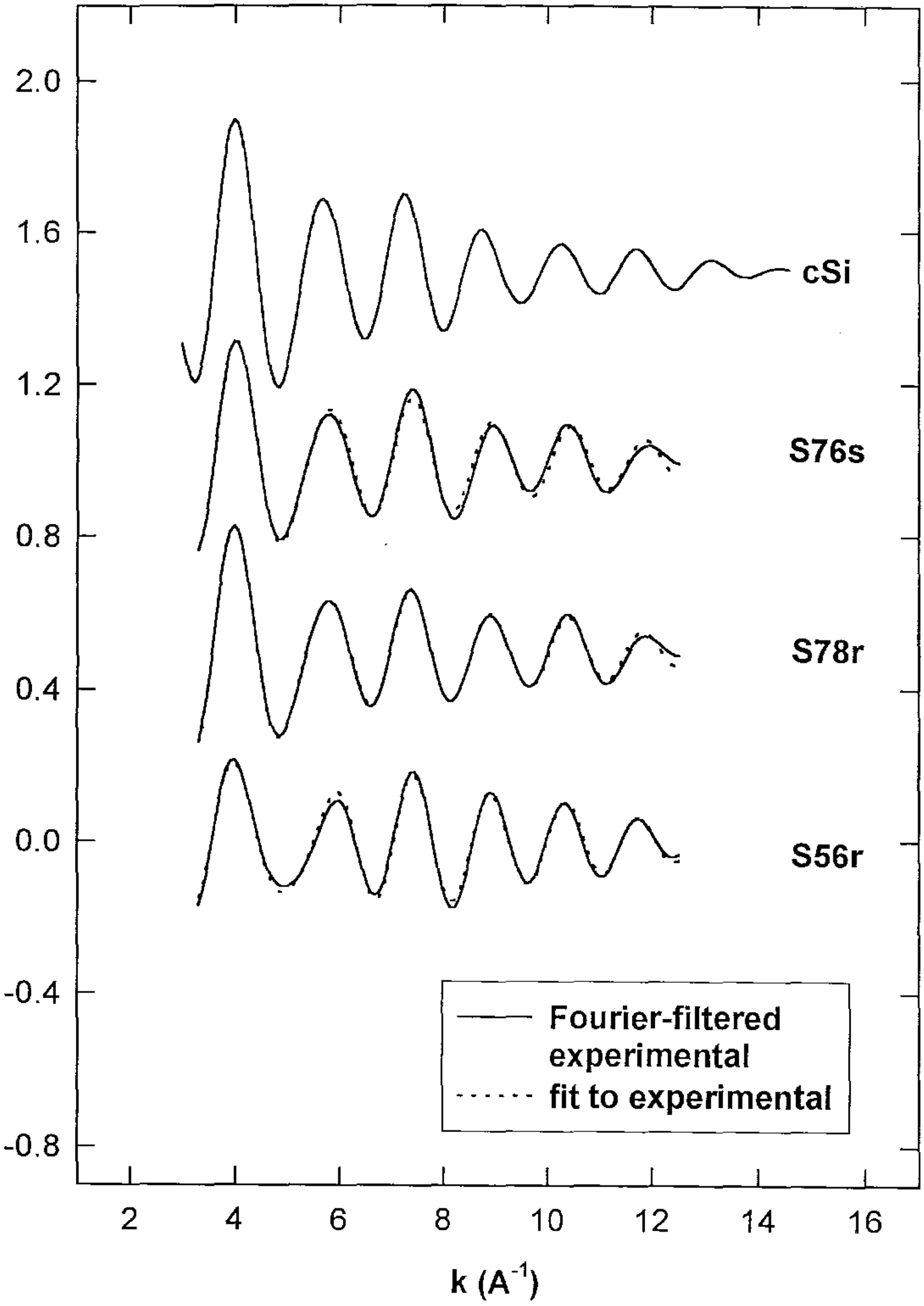

Figure 6.14 - Fit 2 fitted spectra for Si K-edge experimental spectra

Table 6.3: EXAFS Fit Results For Fit 2

Ge K-edge

Sample	r_{GeGe} (Å)	+/-	r_{GeSi} (Å)	+/-	N_{Ge}	N_{Si}	σ^2_{GeGe} ($*10^{-3}$)	σ^2_{GeSi} ($*10^{-3}$)
cGe	2.450	0.002			4.00	0.20	3.3	
S56r	2.440	0.020	2.406	0.020	2.39	2.01	3.6	5.5
S50s	2.423	0.020	2.392	0.020	2.38	1.87	3.2	3.9
S78r	2.421	0.020	2.400	0.020	1.49	2.67	3.9	3.0
S76s	2.413	0.020	2.389	0.020	1.46	2.61	4.4	2.8

Si K-edge

Sample	r_{SiSi} (Å)	+/-	r_{SiGe} (Å)	+/-	N_{Si}	N_{Ge}	σ^2_{SiSi} ($*10^{-3}$)	σ^2_{SiGe} ($*10^{-3}$)
S56r	2.364	0.020	2.406*	0.020	2.22	1.89	1.7	3.1
S50s	NA		NA		NA	NA	NA	NA
S78r	2.355	0.020	2.400*	0.020	3.63	0.72	2.5	7.0
S76s	2.342	0.020	2.389*	0.020	3.34	0.69	2.9	6.8
cSi	2.352	0.008			4.00		1.9	

*denotes constrained to match the value for Ge K-edge

E_0 Values

E_0 Term		Value	+/-
$E_{0,\ GeGe}$	fixed at	0.00	
$E_{0,\ GeSi}$		0.45	0.45
$E_{0,\ SiSi}$	fixed at	0.00	
$E_{0,\ SiGe}$		-0.07	1.21

Note that the errors for the bond lengths are quite large. This is a result of the very limited set of samples included in the fitting. Figure 6.15 depicts the bond lengths as functions of composition. Clearly, the very large error bars on the points preclude any definitive statement regarding strain effects on bond lengths. Nonetheless, the points themselves seem to indicate that the strained samples have shorter bond lengths. Whether the difference is significant or not, is the critical question that can only be answered after a thorough analysis of more measurements on a larger set of samples.

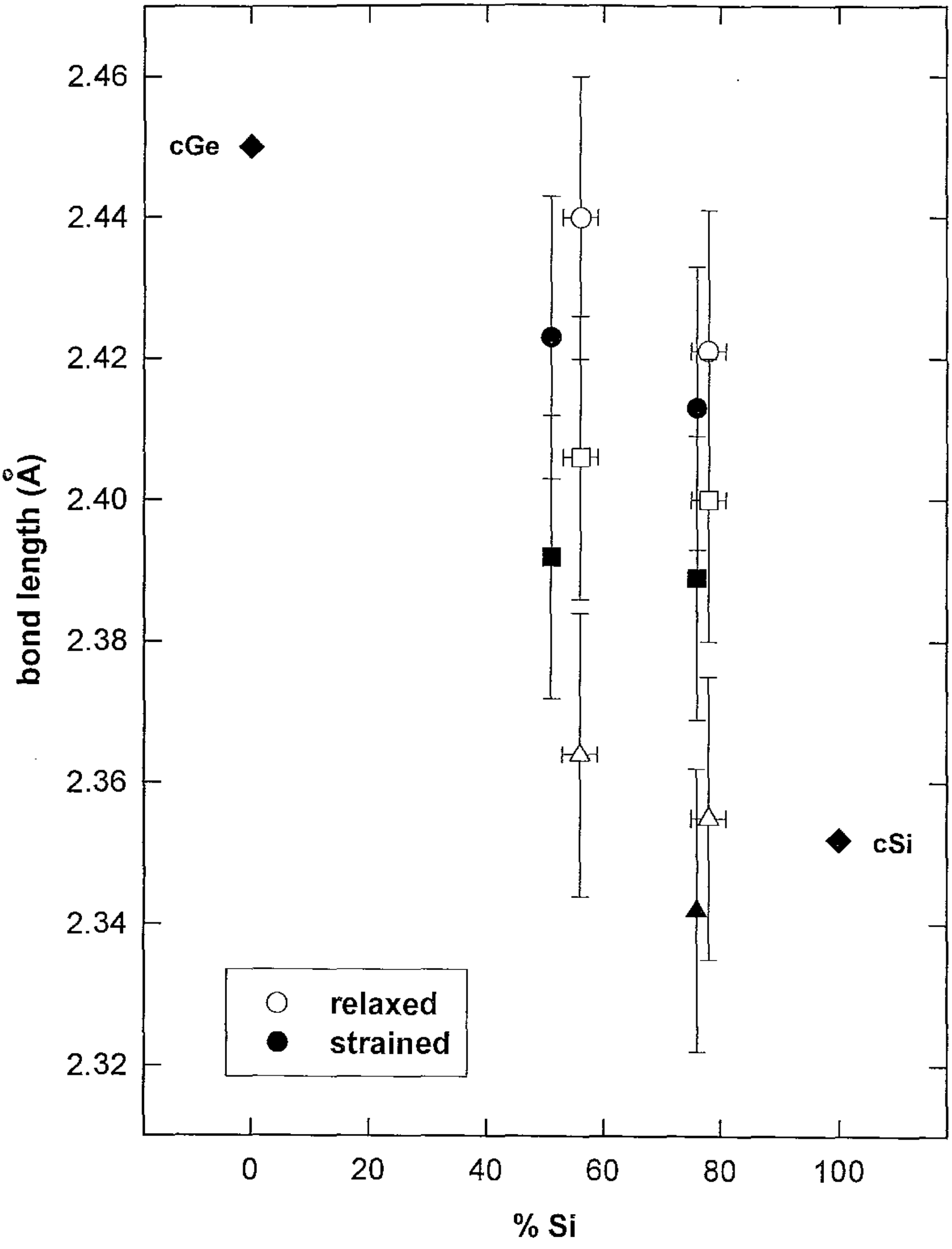

Figure 6.15 - Bond length dependence upon strain, for a series of relaxed and strained complimentary samples.

As stated previously, the error bars in Figure 6.15 are too large to make any conclusions regarding the bond lengths in strained vs. relaxed samples. The data points themselves are tantalizing, seeming to indicate that strain induces a slight bond length contraction. Furthermore, it has been this author's experience that in every fit, no matter what model was chosen or what "tricks" were implemented, strained SiGe alloys on Si(100) always had slightly shorter bond lengths. This observation is important, as it seems to indicate that epitaxial strain is accommodated, at least in part, by bond length changes, much as steric strain was shown to be in this work.

Sample S76s and S78r are reasonably close in composition (76.0 ± 0.05% Si and 78.0 ± 3.0% Si, found by fitting to (114) reflectivity profile and lattice mapping of the $(\overline{22}4)$ peaks, respectively). This permits a quantitative comparison of lattice parameters to be made. Table 6.4 below details the results of the comparisons:

Table 6.4: Lattice Parameter Comparisons

	S76s	S78r	Volume Expansion
composition (%Si)	76.0 ± 0.05	78.0 ± 3.0	
diffraction lattice parameter (Å)	5.4469 (perp) 5.43105 (par)	5.4800	
unit cell volume ($Å^3$)	160.66	164.57	2.38%
EXAFS lattice parameter (Å)	5.46	5.48	
unit cell volume ($Å^3$)	163	165	1.31%

These calculations allow two inferences to be made. The first inference is that the magnitude of the suspected change in bond lengths is reasonable (i.e. the resulting change in unit cell volume is within that measured by diffraction). The second inference concerns the nature of strain accommodation within the unit cell. The measured 2.38% volume contraction due to epitaxy can be accommodated by bond length contraction and/or bond angle changes. From the results shown above in Table 6.4, it seems that slightly over 50% of the accommodation is due to bond length compression.

Again, it is necessary to reiterate that these results are rather tentative. The uncertainties in the points in Figure 6.15 must be significantly reduced (by about a factor of 2) in order to make firm conclusions regarding a possible bond length contraction in strained materials. This should not be too difficult a task with a much larger sample set.

7.0 CONCLUSION

In this chapter, a very brief summary of the results of this work will be given, followed by a few closing remarks, including a discussion of possible future work in SiGe EXAFS.

7.1 Summary

In Fit 1, Si and Ge K-edge EXAFS spectra of a range of relaxed single crystal SiGe alloys have been obtained. Analysis of the first shell EXAFS data was performed using the in-house MFIT software for constrained, non-linear curve fitting of multiple spectra. The bonding in SiGe alloys has been found to be mostly, but not completely, Pauling-type in nature. Using the CT model of Cai and Thorpe [CT92, MT92], for these materials we find a value of **a**** = $0.70^{+0.09}_{-0.03}$, where **a**** is the topological rigidity parameter (**a**** = 0.0 is completely Vegard, **a**** = 1.0 is completely Pauling). The results are in good agreement with both experimental [ANS94] and theoretical [MT93, MT92, WN92, GGB91, I+90, MZ84] published results.

Additionally, in Fit 2, Si and Ge K-edge EXAFS spectra for a small range of relaxed and strained single crystal SiGe alloys have been obtained. Much as in Fit 1, first shell EXAFS analysis was performed using the MFIT program. Tentatively, we have obtained results which suggest that strained samples have slightly shorter bond lengths than their relaxed counterparts, such that approximately 50% of strain accommodation within the unit cell is accomplished by bond length contraction.

7.2 Future Work

Our inability to obtain reliable measurements of dilute Si samples is a limitation in this work. Future Si K-edge EXAFS studies of low composition alloys would be valuable in order to extend the range of compositions covered. This would also permit better explorations of fitting sigmoidal curves to the heteroatomic bond lengths in Fiit 1. If and when impurity dimer bond length calculations become available for the SiGe system, one could then compare the Si and Ge K-edge EXAFS results for dilute samples directly to these. Additionally, the ability to obtain Si K-edge EXAFS data for dilute samples would permit the use of ultra-dilute alloys for fit models, especially since we now have reasonable estimates for r_{GeSi} at the dilute limits. In this manner, one could redo the fitting, in hopes of improving the quality of the fit, and thereby reducing the magnitude of the uncertainties. Improved models may also enable the sharing of heteroatomic Debye-Waller factors, which would further reduce the number of free parameters, and constrain the fit even more.

Epitaxial strain accommodation at the atomic level is a subject of enormous importance in materials growth research, with great potential for producing advances in device engineering. Thus, there is considerable impetus to continue EXAFS measurements of strained layers, in hopes of obtaining improved results. Unfortunately, strained epilayers on Si present considerable problems for Si K-edge EXAFS measurements, because they are so thin. As the thickness decreases, the TEY signal contamination by the substrate increases. Though substrate contamination is less of a problem for studies of Si K-edge measurements on Ge, thick epilayers on are very difficult to grow, and thus, usable samples tend to be very thin (private communication with J-.M. Baribeau, Institute for Microstructural Sciences, National Research Council). This introduces problems with the signal-to-noise ratio. Also, Ge K-edge measurements are impossible to do with our current technology, since the penetration depth at the Ge K-edge is on the order of 1 μm.

Thus, in order to get reasonable EXAFS of thin (i.e. 10 Å or less) strained epilayers, one needs to avoid the substrate contribution as much as possible and improve the signal-to-noise ratio. Oyanagi et al. have demonstrated an elegant way to do this. In one of their latest works [O+95], a Ge K-edge EXAFS study of Ge sub-monolayers on Si(100), they describe how they obtained high quality measurements using fluorescence detection in a total external reflection geometry with their sample mounted at the center of an eight axis goniometer. With superb position controlling of both the x-ray beam and the sample, they are able to maintain total external reflection for all energies, and thus, measure the overlayer absorption without substrate contamination. Such methods would be very useful for obtaining results for strained SiGe films.

Another way to address the question of strain accommodation in SiGe at the local level would be to perform a detailed second shell analysis of the data. The second shell distances (of which there are six different) can be expected to vary by approximately 0.07 Å over the entire composition range, a much larger amount than the 0.02 Å of the first shell [MT92]. Analysis of these would permit the construction of a short range lattice model of the SiGe structure, which would then permit the analysis of both bond length and bond angle accommodation of strain. This would be a difficult task, though, as the second shell signal strongly overlaps the third shell signal and is heavily contaminated by a triangular multiple scattering path [N95]. In addition, a detailed multishell analysis would aid in determining quantitative results for the passive electron reduction terms, since these are constants between shells. Thus, this would aid in the investigation of ordering presented in Chapter 6.

7.3 Concluding Remarks

In closing, Si and Ge K-edge EXAFS measurements have been used to obtain quantitative results for bond lengths and co-ordination numbers in thin film SiGe alloys. The results published in this work significantly contribute to the discussion regarding steric and epitaxial strain effects on individual bond lengths in alloys. Additionally, the near-edge project detailed in the Appendix is a significant extension of the work published previously by Hitchcock et al. It is hoped that this work will stimulate further interest into x-ray absorption spectroscopy and materials physics.

APPENDIX - POLARISATION DEPENDENCE IN SiGe ALLOYS

Contained within this appendix is a project complimentary to the EXAFS portion of this work. The project, a NEXAFS study of SiGe alloys, details the investigation of a polarization dependent signal in the near-edge features of the Si K-edge x-ray absorption spectra for these alloys.

A1.0 Introduction, Literature Review, and Proposal

Many different effects play a role in determining near edge structure, i.e. bond types, x-ray polarization, oxidation state, charge transfer mechanisms, multiple scattering by multiple coordination shells, etc. [D88, W86, L+81]. As a result of this, it is often difficult to develop a clear understanding of near edge structure. By studying the near edge (i.e. NEXAFS analysis), however, one can obtain semi-quantitative understanding of the dominant effects that produce the structure. NEXAFS analysis differs from EXAFS in that it is a probe of the electronic levels in a material. In the case of crystalline solids, where the electronic levels are well described by highly delocalized energy bands, NEXAFS can reveal information about the long range structure. In the cases of molecules or dopants in crystals, where there is no long range structure, NEXAFS probes localized energy levels, which reveals information about the local structure. An excellent example of the utility of NEXAFS in dopant characterization was demonstrated by Schuppler et al. [S+95]. In their experiments, the authors studied the near edge characteristics of the amophoteric (both an n-type and a p-type) dopant Si in

Si-saturated GaAs. They determined that the poor electrical properties of the material were not solely a result of n-type and p-type carriers effectively nullifying each other (autocompensation), but instead, was a result of the formation of neutral Si_{Ga} and Si_{As} dimers and Si_n clusters.

Hitchcock et al. have gleaned considerable information from the Si K-edge NEXAFS data of SiGe materials [H+94, T+94, H+93]. Specifically, they have determined that a polarization dependence exists in the near-edge data of SiGe alloys and heterostructures. Using plane-polarized synchrotron radiation, they measured the spectra of a limited sample of single crystal epitaxial SiGe materials, with the electric field vector (E-vector) of the photon beam mostly parallel to the normal vector of the SiGe film, and again, with the E-vector perpendicular to the normal (see Figure A1). In both geometries, the x-ray/matter interaction volume within the film was maintained relatively constant, as the sample was aligned to the photon beam such that a constant incidence angle of 20^{o} was maintained. In this fashion, contributions from anisotropic surfaces states are thought to be about similar in magnitude, i.e. both are weak in comparison to the bulk signal. Thus, upon subtraction of the resulting spectra for the two geometries, only the difference in the bulk signals is significant.

The leftover signal, first noted by Hitchcock et al. [H+93], is a characteristic difference within the edge jump (Figure A2), for which they found the phase to be dependent upon the orientation of the strain in the sample (Figure A3). Hitchcock et al. concluded that the source of this polarization was due to the presence of anisotropic low energy conduction band states which are sensitive to the magnitude and the orientation of the strain within the SiGe alloy layer. Unfortunately, they were unable to make clear connections with the calculated band structures of Ma et al. [MWS93], since they lacked the necessary resolution at the Si K-edge.

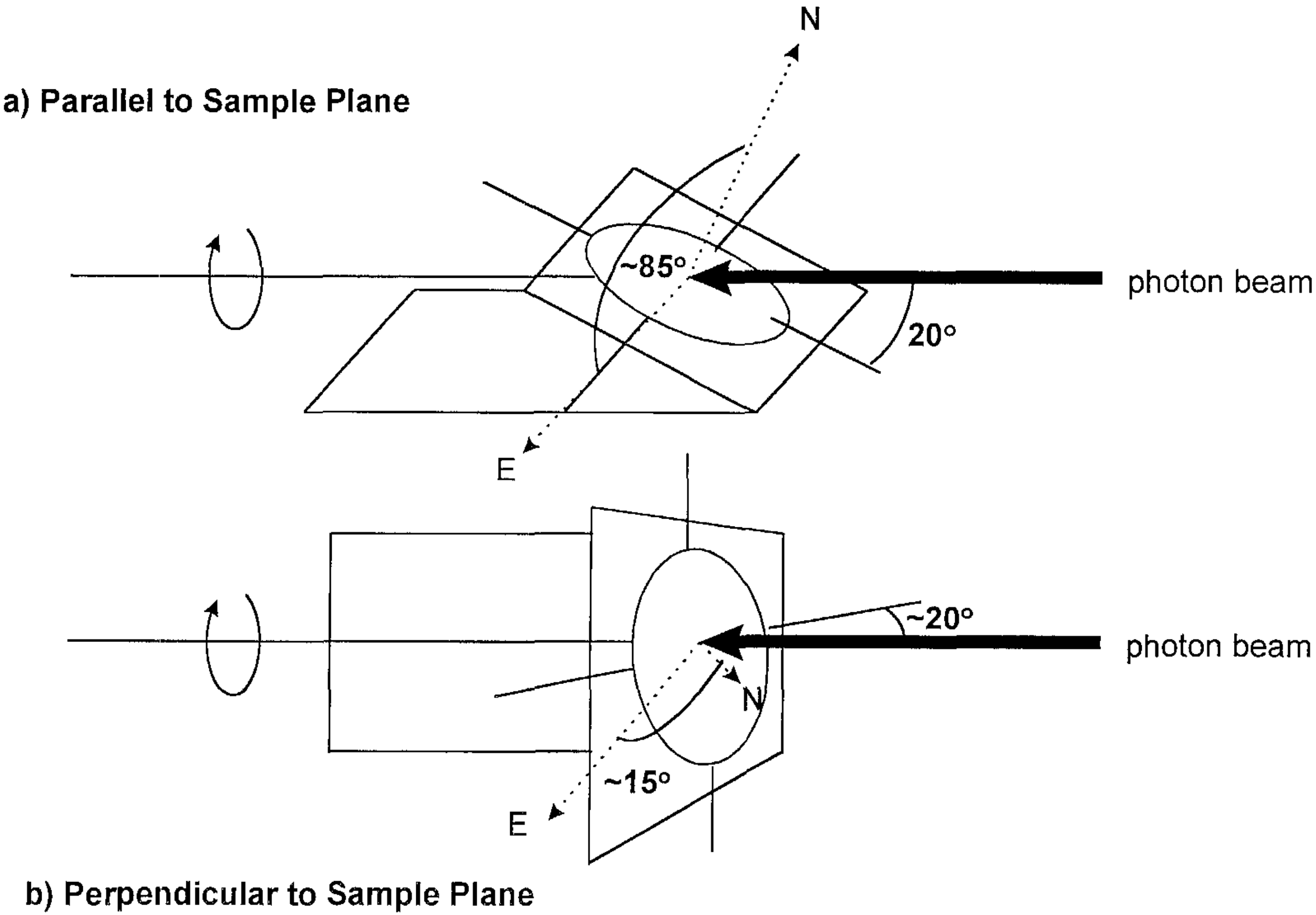

a) Parallel to Sample Plane

b) Perpendicular to Sample Plane

Figure A1 - Geometries used in polarisation measurements. Part a) depicts the perpendicular arrangement, where the E-vector of the radiation is perpedicular to the sample normal. Part b) depicts the parallel arrangement, where the E- and normal vectors are parallel.

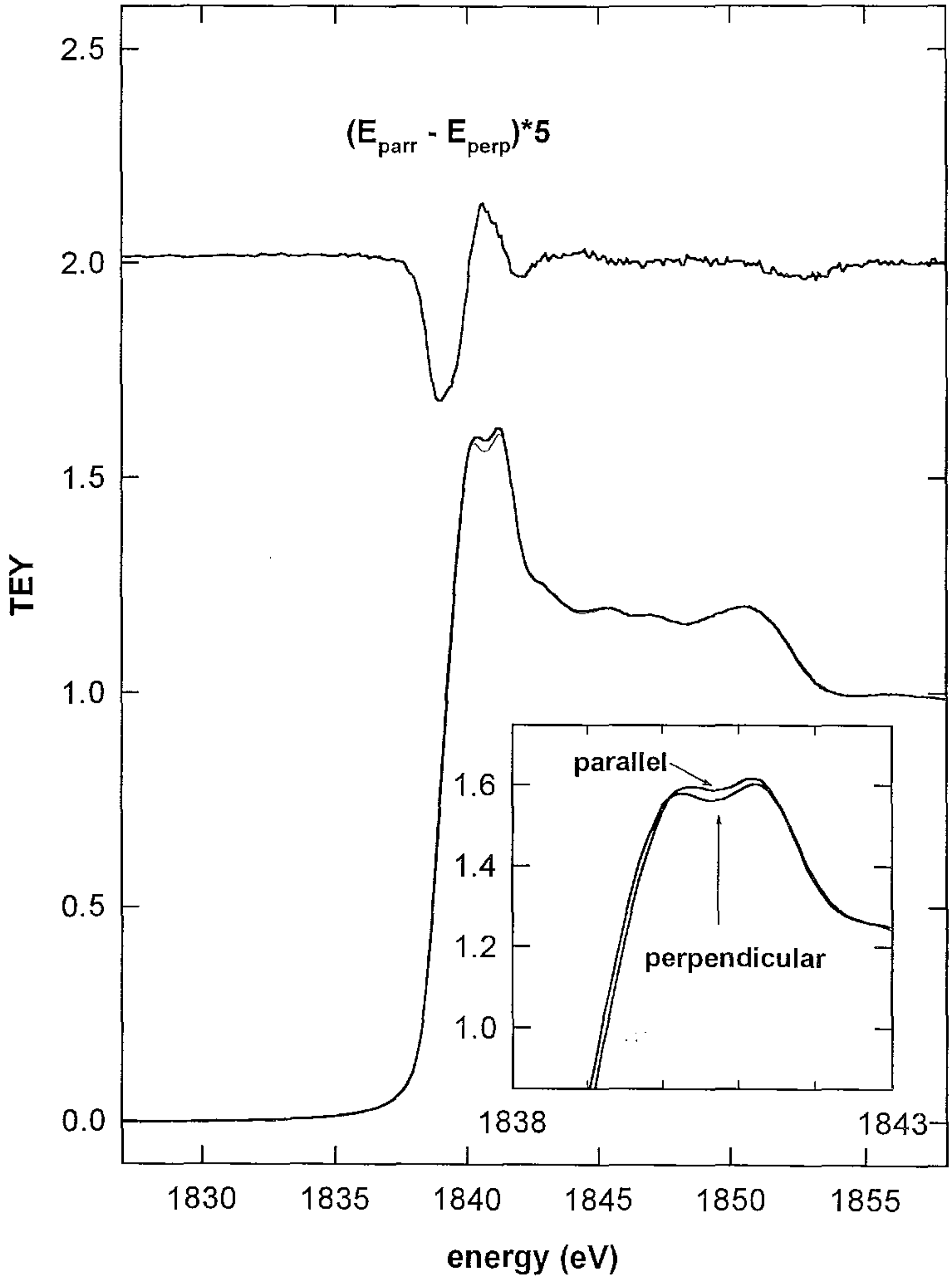

Figure A2 - Origin of the difference signal for sample S50s. The spectra for the perpendicular and parallel geometries are precisely lined up, and the difference is obtained. The inset figure depicts an up-close image of the white lines.

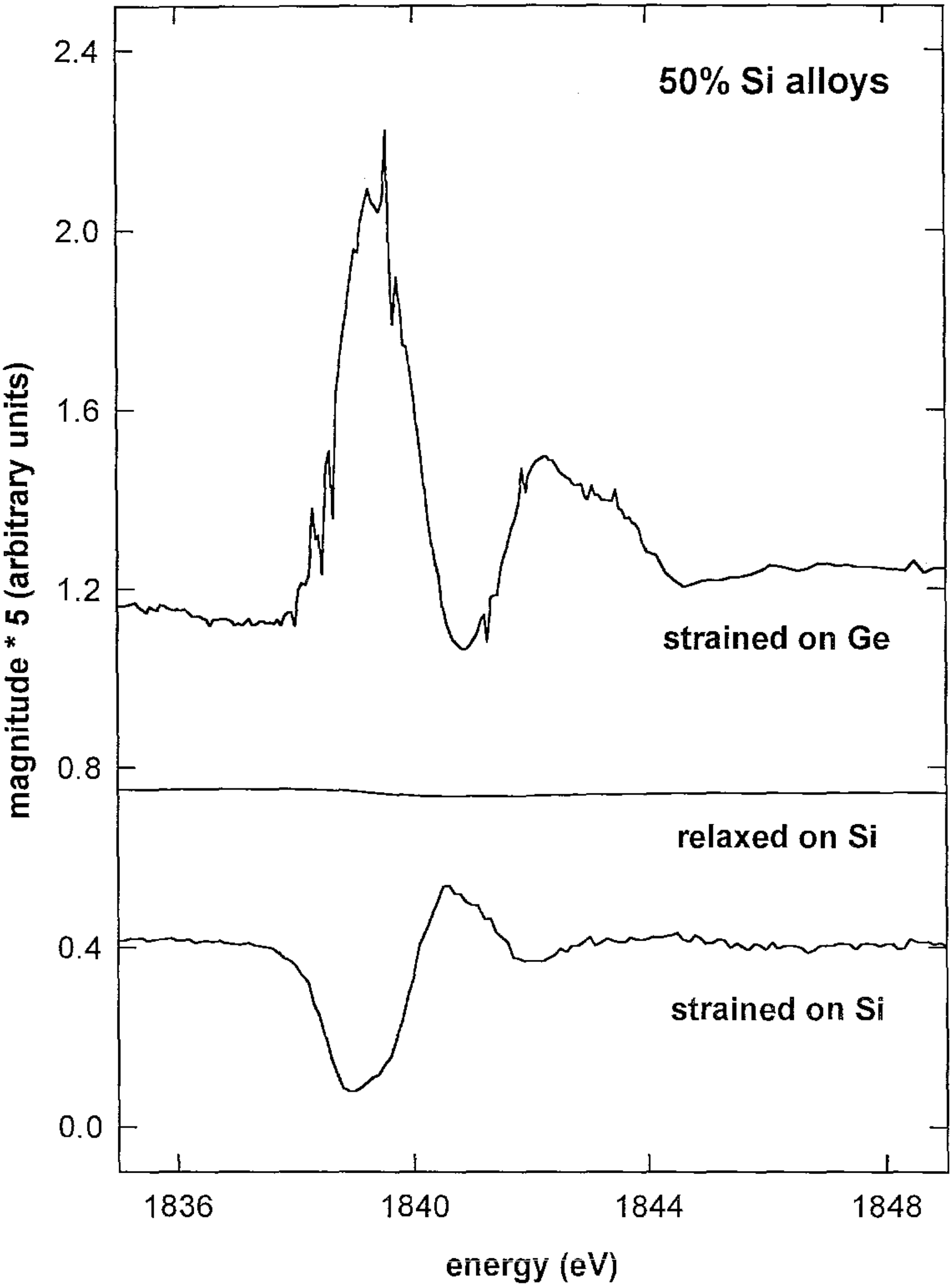

Figure A3 - Polarisation magnitude for 50% SiGe alloys. The relaxed alloy has virtually no polarisation, while the strained alloys have opposite polarsitions due to the two different substrates.

This author has further documented the Si K-edge polarization dependence of epitaxial SiGe alloys, extending the sample coverage to include a full range of strained and relaxed samples on Si(100) substrates, as well as strained, relaxed, and annealed samples on Ge(100) substrates. The motivation for these experiments was to quantify the relationship between the polarization signal and the alloy strain. It was hypothesized that the magnitude of the polarization signal should be a function of composition, since the strain tensor within the alloy layers is proportional to composition. One of the prime motivations for this work was to test this hypothesis, and so we have collected NEXAFS spectra for the two geometries (parallel and perpendicular) for a range of strained, relaxed, and annealed samples, spanning the entire composition range, on both Si(100) and Ge(100) substrates. The experimental details and a presentation of the results follow below.

A2.0 Experimental and Data Processing

The Si K-edge near edge measurements were obtained in the same manner as the Si K-edge EXAFS measurements described above. The experiments were performed at the CSRF-DCM beamline at the SRC, including sample preparation (HF etching, etc.). All experimental apparatus was identical to that used in the Si K-edge EXAFS measurements, except for the sample stage used for mounting in the EXAFS chamber. In order to provide the correct geometry, a stage was positioned on a rotary feedthrough mounted along the axis of the photon beam (see Figure A1). The sample was mounted on an angled portion of the stage, such that in either the parallel or perpendicular geometry, the angle of incidence with the photon beam is maintained at 20°. In this fashion, differences in surface/bulk contributions are eliminated, and less substrate signal is included in the TEY detection. Spectra were recorded as for EXAFS spectra (a range of 1830 eV to 1865 eV), but with a much finer point spacing (in order to better resolve fine near-edge features), typically 0.05 eV. Scans typically ran for periods of 20 minutes each, and were always run consecutively within a given fill period, to avoid problems with realignment with respect to the beam, which shifts slightly from fill to fill. The I_0 oscillation described in Chapter 3 is not a problem in these measurements, since the period of these oscillations (~200 eV) is much longer than the scan range (35 eV).

Following spectral acquisition for the two geometries for a given sample, the spectra were precisely aligned to each other using pre-edge linear background subtractions. This often involved considerable trial and error, as very minute differences in the alignment would have major effects in the resulting difference spectra. After alignment, the spectra were normalized at a plateau at 1857 eV. From these spectra, termed *.bsn files (filenames: Background-Subtracted, Normalized), the difference spectra were obtained (by convention, E-vector parallel to sample plane - E-vector perpendicular to sample plane). Again, by convention, the difference spectra are multiplied by a factor of 5 (hence the term *.df5 files). Figure A2 depicts typical *.bsn and *.df5 spectra for a strained SiGe alloy grown on Si. Optimally, one expects that all of the difference signal is contained in a very narrow region of the *.df5 spectra (i.e. only in the edge jump region of the spectra, 1838-1842 eV). Occasionally, some of the signal extends out to slightly higher post-edge energies; however, beyond 1850 eV and before 1836 eV, there should by no difference signal (i.e. intensity of 0). The presence of a sizable signal here is indicative of a poor or inadequate background subtraction. Difference spectra with such signals are discarded, and the background subtraction procedure is redone, until an acceptable difference spectra is obtained. Table

3.1(above) lists the compositional and structural data for the relevant samples used in the near-edge study.

A3.0 Results and Discussion

Figure A4 depicts the magnitude of the difference spectra (as functions of composition) for a range of SiGe alloys, as well as c-Si. The magnitudes are obtained by subtracting the intensity values of the 1839 and 1841 eV peaks in the difference spectra. The assigned uncertainties are estimates, based upon experience in the variability of the difference magnitude with different background subtractions. The points are grouped according to strain state and strain sign (+ for a positive strain, i.e. SiGe on Ge, and vice versa).

The first item of note in Figure A4 is a non-zero polarization signal for c-Si, which is not strained. Within the error bars on Figure A4, it is effectively zero, but for c-Si, this error estimate is probably too large, since this result has been confirmed several times on several pieces of c-Si, over a period of 5 years, at two different synchrotrons. In contrast, an unstrained sample, S56r, shows no polarization signal, and neither does amorphous Si. To date, it remains a mystery why c-Si should routinely have a non-zero polarization signal. It has been suggested that the source of this signal could be external mechanical strain from sample mounting or wafer cutting. Future work may include a test for this using in-situ mechanical strain on S56r.

From Figure A4, one can see that, just as previously seen [H+94, T+94, H+93], relaxed alloys on Si have little or no polarization dependence. The residual signal they do show is most likely a result of residual strain in the samples, which was mentioned in Chapter 3. Unfortunately, there are only three corresponding points for relaxed samples on Ge. Two have polarizations close to zero; however, the third point (representing

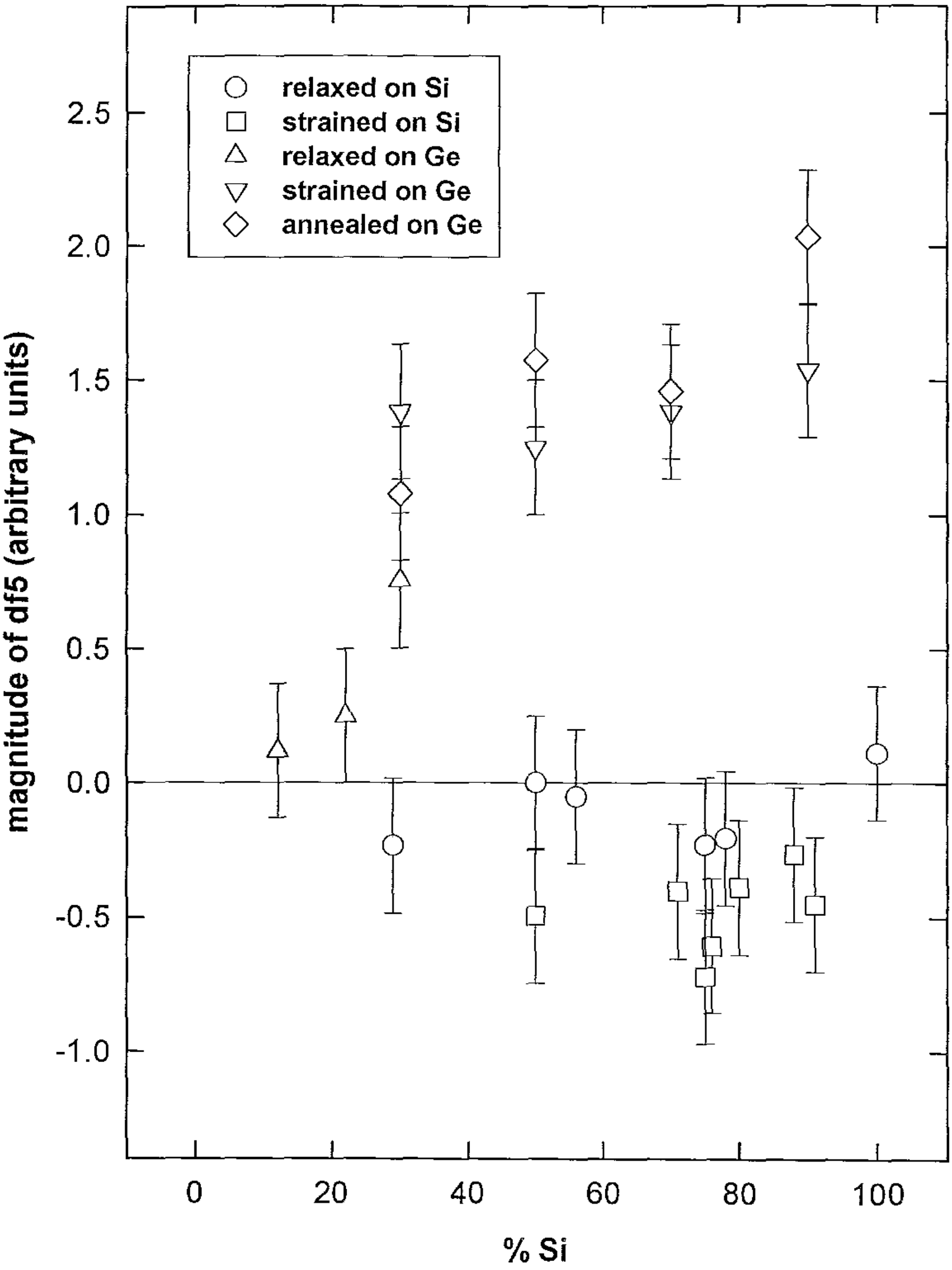

Figure A4 - Polarisation magnitude as a function of composition for a series of strained and relaxed alloys on Si, as well as a series of strained and annealed alloys on Ge.

G30r) has a rather large polarization. This is probably an indication that this sample has still retained significant strain (though it is very thick, and should be completely relaxed). Reciprocal lattice map measurements of this sample should be obtained in order to measure how much strain has been retained. If the sample is found to be mostly relaxed, it will then be necessary to reconfirm the polarization signal. Also, an expanded set of relaxed alloys on Ge is needed in order to extend the measurements across the entire compositional range.

Based upon the results presented in Figure A4, it is difficult to determine if there is any compositional dependence in the magnitudes of the difference signals. Originally, the tentative conclusion of compositional dependence was made by Hitchcock et al. based upon data from a limited set of three samples (G12s, G25s, G50s) [H+94, T+94, H+93]. Since the time of these publications, it has been discovered that one of the samples (G50s), which had an anomalously large difference signal, had undergone an abnormal pre-growth anneal. A new sample of this composition and strain state was grown (G50s2), and new measurements were obtained, for which the results proved to be in better agreement with the other samples. While regression lines to the data points in Figure A4 indicate that there is a very small slope to the sets of points, it is questionable whether a true composition dependence actually exist, given the size of the error bars. In reality, the arbitrary choice of error bars is probably too conservative, and a weak dependence may exist.

Another item of note, however, is the difference in the magnitude of the polarization signal between strained samples on Ge and Si. This was originally observed by Hitchcock and co-workers [H+94, T+94, H+93], and it is observed again in this more extensive study. The reason for this difference in signal strengths is not understood, since for a 50% Si alloy, the strain should be equal, but opposite, for the two substrates. One possible explanation is signal contamination by the Si substrate. For the thinner samples especially, a fraction of the TEY signal will originate from the substrate, which has no polarization. Thus, the polarization magnitude of the alloy will appear to be smaller than it should be.

Of most interest, though, is the magnitude of the polarization in the annealed samples on Ge. Typically, the annealing performed on these samples (30s at 900°C) removes 100% of the alloy strain, as determined by TEM and x-ray diffraction measurements [H91]; however, the polarization measurements indicate that these samples have retained significantly more of their strain than expected, and one point (for G90a) is higher than its strained counterpart. These are very strange results; yet, they have been confirmed with a second set of measurements on new sample pieces. Annealing in a rapid thermal annealing unit (RTA) is performed under a N_2 atmosphere, and is not expected to affect the sample, other than to permit significant diffusion and/or migration [H91]. Possible substrate/epilayer intermixing would result in a slightly reduced %Si for the sample; however, this does not explain the larger than expected signal. Oxide build up is not the source either, since the sample was HF-etched. Clearly, this is a mystery which we do not fully understand.

A4.0 Conclusion

We have attempted to quantify the relationship between the polarization dependence seen in the near-edge spectra of SiGe alloys and their strain state. Specifically, we were testing the hypothesis that the magnitude of the polarization signal was directly related to the magnitude of the strain within the alloy. Our results indicate that a composition dependence is not clearly seen, but may still exist. An extension of the sample set to include strained low %Si samples on Ge(100) may help in establishing a clear compositional relationship. Similar samples on Si(100) are too thin for our TEY measurements; however, some of the techniques in Chapter 8 may permit these measurements to be made.

The most important result of this study is a realization that perhaps we do not properly understand the source of the polarization signal. Specifically, we do not understand: a) why c-Si has a non-zero polarization signal, b) why there is such a weak compositional dependence, c) why there is a large magnitude difference between alloys on Si(100) and Ge(100), or d) why samples thoroughly annealed should have larger polarization signals than their strained counterparts. Thus, we must revisit our interpretation of the source of this signal. A popular method of studying near edge spectra is to perform theoretical calculations, in an attempt to reproduce the spectra. Unfortunately, adequate calculations have not been available for these spectra; however, recent discussions with Fujikawa (Chiba University, private communication) indicate that adequate calculations will be available soon. We are planning to make significant use of these, in order to see if we can reproduce a polarization dependence.

REFERENCES

The convention used in this composition is to list the first initial of the of the authors' surname, followed by the last two digits of the year of publication. If there are more than 3 authors, only the initial of the primary author, followed by a '+' and the publication year are used. Ordering within the list is by the first letter in the code (e.g. [D+56] would be in the "D" listing), followed by the year of publication. In the case of identical ranks, order is determined alphabetically by the primary author's name.

[A+96] M. Arafa, P. Fay, K. Ismail, J.O. Chu, B.S. Meyerson, and I. Adesida, *IEEE Electr. Dev. Lett.* **17**, 124 (1996).

[ANS94] D.B. Aldrich, R.J. Nemanich, and D.E. Sayers, *Phys. Rev. B* **50**, 15026 (1994).

[A+92] P. Aebi, T. Tyliszczak, A.P. Hitchcock, K.M. Baines, T.K. Sham, T.E. Jackman, J.M. Baribeau, and D.J. Lockwood, *Phys. Rev. B* **45**, 13579 (1992).

[A+91] M. Arienzo, S.S. Iyer, B.S. Myerson, G.L. Patton, and J.M.C. Stork, *Appl. Surf. Sci.* **48/49**, 377 (1991).

[A+89] G. Abstreiter, K. Eberl, E. Friess, W. Wegscheider, and R. Zachai, *J. Cryst. Growth* **95**, 431 (1989).

[B92] J.C. Bean, *Proc. of the IEEE* **80**, 571 (1992).

[B87] A. Balzarotti, in Ternary and Multinary Compounds, edited by D.S. Deb. and A. Zunger (Materials Research Society, Pittsburgh, 1987), p. 333.

[B86] J.C. Bean, *Physics Today* **Oct**, 36 (1986).

[B+85] A. Balzarotti, N. Motta, A. Kisiel, M. Zimnal-Starnawska, M.T. Czyzyk, and M. Podgorny, *Phys. Rev. B* **31**, 7526 (1985).

[BM85] J.B. Boyce and J.C. Mikkelsen Jr. *Phys. Rev. B* **31**, 6903 (1985).

[BM83] J.B. Boyce and J.C. Mikkelsen Jr. *Phys. Rev. B* **28**, 7130 (1983).

[B20] W.L. Bragg, *Philos. Mag.* **40**, 169 (1920).

[C+96] M. Casalboni, N. Pinto, B. Izzi, I. Davoli, M. DeCrescenzi, F. DeMatteis, P. Prosposito, and R. Pizzoferrato, *Phys. Rev. B* **53**, 1030 (1996).

[C95] J.D. Cressler, *IEEE Spectrum* **Mar**, 49 (1995).

[CT92] A series of 2 papers:
Y. Cai and M.F. Thorpe, *Phys. Rev. B* **46**, 15872 (1992), and
Y. Cai and M.F. Thorpe, *Phys. Rev. B* **46**, 15879 (1992).

[CE92] L.L. Chang and L. Esaki, *Physics Today* **Oct**, 36 (1992).

[C85] CHESS C2 Beamline Experimental Manual (1985).

[CRI88] E.D. Crozier, J.J. Rehr, and R. Ingalls, X-Ray Absorption: Principles, Applications, Techniques of EXAFS, SEXAFS, and XANES, edited by D.C. Konigsberger and R. Prins (John Wiley & Sons, Toronto, Ontario, 1988).

[CS81] G.S. Cargill and F. Spaepen, *J. Non-Cryst. Solids* **43**, 91 (1981).

[CT65] J.W. Cooley and J.W. Tukey, *Math. Computation* **19**, 297 (1965).

[D88] P.J. Durham, X-Ray Absorption: Principles, Applications, Techniques of EXAFS, SEXAFS, and XANES, edited by D.C. Konigsberger and R. Prins (John Wiley & Sons, Toronto, Ontario, 1988).

[DEP64] J.P. Dismukes, L. Ekstrom, and R.J. Paff, *J. Phys. Chem.* **68**, 3021 (1964).

[E92] F. Evangelisti, *J. Non-Cryst. Solids* **141**, 53 (1992).

[E+88] A. Erbil, G.S. Cargill III, R. Frahm, and R.F. Boehme, *Phys. Rev. B* **37**, 2450 (1988).

[E86] L.F. Eastman, *Physics Today* **Oct**, 77 (1986).

[F96] A. Frenkel, *Proc. of XAFS-9* (Elsevier, 1997).

[F+86] A. Filliponi, P. Fiorini, F. Evangelisti, A. Balerna, and S. Mobilio, *J. de Phys. Coll.* **8**, 357 (1986).

[GOE95] H.G. Grimmeiss, J. Olajos, and J. Engvall, *Acta Physica Polonica* **88**, 567 (1995).

[GGB91] S. de Gironcoli, P. Giannozzi, and S. Baroni, *Phys. Rev. Lett.* **66**, 2116 (1991).

[HH96] G.D. Hutcheson and J.D. Hutcheson, *Sci. Am.* **Jan**, 54 (1996).

[H+95] K.D. Hobart, F.J. Kub, N.A. Papanicoloau, W. Kruppa, and P.E. Thompson, *J. Cryst. Growth* **157**, 215 (1995).

[H+94] A.P. Hitchcock, T. Tyliszczak, P. Aebi, X.H. Feng, Z.H. Lu, J.-M. Baribeau, and T.E. Jackman, *Surf. Sci.* **301**, 260 (1994).

[H+93] A.P. Hitchcock, T.Tyliszczak, P. Aebi, J.Z. Xiong, T.K. Sham, K.M. Baines, K.A. Muller, X.H. Feng, J.M. Chen, B.X. Yang, Z.H. Lu, J.-M. Baribeau, and T.E. Jackman, *Surf. Sci.* **291**, 349 (1993).

[H91] D.C. Houghton, *J. Appl. Phys.* **70**, 2136 (1991).

[I+90] M. Ichimura, Y. Nishino, H. Kajiyama, and T. Wada, *Jpn. J. Appl. Phys.* **29**, 842 (1990).

[I+85] L. Incocia, S. Mobilio, M.G. Proietti, P. Fiorini, C. Giovannella, and F. Evangelisti, *Phys. Rev. B* **31**, 1028 1985.

[I69] International Tables For X-Ray Crystallography, Vol. III: Physical and Chemical Tables 264 (1969).

[J+93] D.E. Jesson, S.J. Pennycook, J.Z. Tischler, J.D. Budai, J.M. Baribeau, and D.C. Houghton, *Phys. Rev. Lett.* **70**, 2293 (1993).

[J+92] D.E. Jesson, S.J. Pennycook, J.M. Baribeau, and D.C. Houghton, *Phys. Rev. Lett.* **68**, 2062 (1992).

[JPB91] D.E. Jesson, S.J. Pennycook, and J.M. Baribeau, *Phys. Rev. Lett.* **66**, 750 (1991).

[K95] E. Kasper *J. Cryst. Growth* **150**, 921 (1995).

[K+95] E. Kasper, A. Schuh, G. Bauer, B. Hollander, and H. Kibbel, *J. Cryst. Growth* **157**, 68 (1995).

[KD95] U. Konig and H. Dambkes, *Solid State Elec.* **38**, 1595 (1995).

[K+92] H. Kajiyama, S. Muramatsu, T. Shimada, and Y. Nishino, *Phys. Rev. B* **45**, 14005 (1992).

[K92] R.W. Keyes, *Physics Today* **Aug**, 42 (1992).

[K+89] C.A. King, J.L. Hoyt, C.M. Gronet, J.F. Gibbons, M.P. Scott, and J. Turner, *IEEE Electron Dev. Lett.* **10**, 2323 (1989).

[K79] C. Kunz, Synchrotron Radiation Techniques and Applications, (Springer-Verlag, Berlin, Germany, 1979).

[K39] J.G. Kirkwood, *J. Chem. Phys.* **7**, 506 (1939).

[LLB95] G.G. Li, F. Bridges, and C.H. Booth, *Phys. Rev. B* **52**, 6332 (1995).

[LB92] D.J. Lockwood, and J.M. Baribeau, *Phys. Rev. B* **45**, 8565 (1992).

[LKI90] F.K. LeGoues, V.P. Kesan, and S.S. Iyer, *Phys. Rev. Lett.* **64**, 40 (1990).

[L+87] D.J. Lockwood, K. Rajan, E.W. Fenton, J.M. Baribeau, and M. W. Denhoff, *Solid State Commun.* **61**, 465 (1987).

[L86] P.B. Littlewood, *Phys. Rev. B* **34**, 1363 (1986).

[L+81] P.A. Lee, P.H. Citrin, P. Eisenberg, and B.M. Kincaid, *Rev. Mod. Phys.* **53**, 769 (1981).

[M94] B.S. Myerson, *Sci. Am.* **Mar**, 42 (1994).

[M+94] E. Murakami, K. Nakagawa, A. Nishida, and M. Miyao, *IEEE Trans. Electr. Dev.* **41**, 857 (1994).

[MSW93] Q.M. Ma, K.L. Wang, and J.N. Schulman, *Phys. Rev. B* **47**, 1936 (1993).

[MT93] N. Mousseau and M.F. Thorpe, *Phys. Rev. B* **48**, 5172 (1993).

[MT92] N. Mousseau and M.F. Thorpe, *Phys. Rev. B* **46**, 15887 (1992).

[M92] B.S. Myerson, *Proc. of the IEEE* **80**, 1592 (1992).

[MTC91] M. Matsuura, J.M. Tonnerre, and G.S. Cargill, *Phys. Rev. B* **44**, 3842 (1991).

[M+91] E. Muller, H.U. Nissen, K.A. Mader, M. Ospelt, and H. von Kanel, *Philos. Mag. Lett.* **64**, 183 (1991).

[MZ86] J.L. Martins and A. Zunger, *Phys. Rev. Lett.* **56**, 1400 (1986).

[MZ84] J.L. Martins and A. Zunger, *Phys. Rev. B* **30**, 6217 (1984).

[N95] M. Newville, Feffit documentation, January 1995.

[N+88] Y. Nishino, S. Muramatsu, Y. Takano, and H. Kajiyama, *Phys. Rev. B* **38**, 1942 (1988).

[OHK96] H. Oyanagi, K. Haga, and Y. Kuwahara, *Rev. Sci. Instrum.* **67**, 350 (1996).

[O+95] H. Oyanagi, K. Sakamoto, R. Shioda, Y. Kuwahara, and K. Haga, *Phys. Rev. B* **52**, 5824 (1995).

[O94] H. Oyanagi, "Recent Progresses in X-Ray Absorption Fine Structure" in Researches of The Electrotechnical Laboratory. (Electrotechnical Laboratory, June 1994).

[OB85] A. Ourmazd and J.C. Bean, *Phys. Rev. Lett.* **55**, 765 (1985).

[OA84] R.W. Olesinski and G.J. Abbaschian, *Bull. Alloy Phase Diagrams* **5**, (1984).

[P91] T.P. Pearsall, *Mats. Sci. and Eng. B* **9**, 225 (1991).

[P+90] W.F. Pong, R.A. Mayanovic, B.A. Bunker, J.K. Furdyna, and U. Debska, *Phys. Rev. B* **41**, 8440 (1990).

[PB85] L. People and J.C. Bean, *Appl. Phys. Lett.* **47**, 322 (1985).

[P73] J.C. Phillips, Bonds and Bands In Semiconductors. (Academic Press, 1973).

[P67] L. Pauling, The Nature of the Chemical Bond (Cornell University Press, Ithaca, NY, 1967).

[R+91] J.J. Rehr, J. Mustre de Leon, S.I. Zabinsky, and R.C. Albers, *Phys. Rev. B* **44**, 4146 (1991).

[SD95] A. Schuppen and H. Deitrich, *J. Cryst. Growth* **157**, 207 (1995).

[S+95] S. Schuppler, D.L. Adler, L.N. Pfeiffer, K.W. West, E.E. Chaban, and P.H. Citrin, *Phys. Rev. B* **51**, 10527 (1995).

[S88] E.A. Stern, X-Ray Absorption: Principles, Applications, Techniques of EXAFS, SEXAFS, and XANES, edited by D.C. Konigsberger and R. Prins (John Wiley & Sons, Toronto, Ontario, 1988).

[S+85] T. Sasaki, T. Onda, R. Ito, and N. Ogasawara, *Jpn. J. Appl. Phys.* **25**, 231 (1985).

[SBH80] E.A. Stern, B.A. Bunker, and S.M. Heald, *Phys. Rev. B* **21** 5521 (1980).

[SSL75] D.E. Sayers, E.A. Stern, and F. Lytle, *Phys. Rev. B* **11**, 4836 (1975).

[SSL71] D.E. Sayers, E.A. Stern, and F. Lytle, *Phys. Rev. Lett.* **27**, 1204 (1971).

[SK39] H. Stohr and W. Klemm, *Z. anorg. allgem. Chem.* **241**, 313 (1939).

[T+95] J.Z. Tischler, J.D. Budai, D.E. Jesson, G. Eres, P. Zschack, J.M. Baribeau, and D.C. Houghton, *Phys. Rev. B* **51**, 10947 (1995).

[T+94] T. Tyliszczak, A.P. Hitchcock, Z.H. Lu, J.-M. Baribeau, and T.E. Jackman, *Scanning Micro.* **8**, 795 (1994).

[V27] L. Vegard, *Z. Phys.* **5**, 17 (1927).

[WN92] M.R. Weidmann and K.E. Newmann, *Phys. Rev. B* **45**, 8388 (1992).

[W+91] J.C. Woicik, C.E. Bouldin, M.I. Bell, J.O. Cross, D.J. Tweet, B.D. Swanson, T.M. Zhang, L.B. Sorenson, C.A. King, J.L. Hoyt, P. Pianetta, and J.F. Gibbons, *Phys. Rev. B* **43**, 2419 (1991).

[W86] J.Wong, *Mats. Sci. and Eng.* **80**, 107 (1986).